LASER ABSORPTION SPECTROSCOPY IN APPLICATIONS FOR TEMPERATURE, CONCENTRATION, AND SPATIAL RECOVERY

A Dissertation Presented for the

Doctor of Philosophy

Degree

The University of Tennessee, Knoxville

Samuel E. Feltis

May 2026

Copyright © 2026 by Samuel E. Feltis

All rights reserved.

Teach me, my God and King,
In all things Thee to see,
And what I do in anything
To do it as for Thee.

ACKNOWLEDGEMENTS

I would like to acknowledge with sincere gratitude the following people without whom this dissertation could never have been:

Dr. Brett Compton and Niya Grimes, for their assistance in operating the dilatometer through all its difficulty.

Drs. Rodney Bowersox and Tyler Dean, whose operation of their hypervelocity wind tunnel allowed much of this research to progress.

Dr. Damiano Baccarella, Killian Samuels, and Mitchell Trotsky, for their assistance through our collaborations and their patience when I used their equipment past its breaking point.

My colleagues Bilge Gokcecik and Mirka Mandich, for their assistance in operating the equipment and parsing through gigabytes of data.

My colleague Aleksander Clark, for his patience and experience.

Dr. Zhili Zhang, my advisor and mentor, for his invaluable insight and instruction.

My family, for always asking, “are you a doctor yet?” when told my scholastic timeline.

And a special thanks to the members of Redeemer Church of Knoxville, for being with me through it all.

ABSTRACT

Laser absorption spectroscopy (LAS) is a diagnostic tool that has been utilized in aerospace and mechanical engineering applications for over a decade. Unlike physical probes which disturb the measured experimental environment, laser light does not significantly impact fluid flow—especially when it comes to high-enthalpy environments. This allows for measuring material characteristics in varying experiments ranging from highly turbulent flows to steady laminar flames.

The recovery of values such as pressure, temperature, and concentrations of absorbing media within a system is vital in any material or aerospace engineering capacity. The purpose of this work is to more fully and meaningfully demonstrate four applications of LAS for material and environmental characterization. Within, these LAS-based experiments characterize composite carbon structures, recover non-equilibrium temperatures behind normal shocks, measure velocity and concentration changes in fast-moving fluid, and reconstruct spatial profiles of combustion environments.

TABLE OF CONTENTS

Chapter One Introduction 1

Tunable Diode Laser Absorption Spectroscopy 1

Ro-Vibrational Temperature Model 5

Wavelength Modulated Spectroscopy 9

Tomographic Reconstruction 13

Chapter Two Mass Spectrometry and Laser Absorption Spectroscopy Instrumentation for Characterization of Carbon Phenolic Composites Pyrolysis 15

Motivation 16

Abstract 16

Introduction 17

Mass Spectrometry and Laser Spectroscopy 18

Methodology 20

Setup 20

Procedure 22

Results 23

Spectroscopic Results 23

Mass Results 27

Discussion of Failures 29

Chapter Three Measurements of NO Rotational and Vibrational Temperatures Behind a Normal Shock in Hypervelocity Flow via Absorption Spectroscopy 33

Motivation 34

Abstract 34
Introduction 35
Setup 37
Facility and Test Conditions 37
Model Geometry 37
Experiment 39
Ro-Vibrational Model 40
Data Processing 42
Results 44
Discussion of Failures 53
Chapter Four Mach 6.5 Arcjet Tunnel Velocity Measurement by Wavelength Modulated Spectroscopy 56
Motivation 57
Abstract 57
Introduction 57
Setup 58
Procedure 59
Results 60
Discussion of Failures 62
Chapter Five Sparse Tomographic Reconstruction of Temperature and Concentration in Ammonia Flames 67
Motivation 68

Abstract 68
Introduction 68
Ammonia Applications 68
Tomographic Application & Recovery 69
Setup 70
Methodology 73
Laser Calibration and Signal Preprocessing 73
Signal Deconvolution 76
Algebraic Reconstruction Tomography 77
Temperature and Concentration Recovery 79
Experiment Reconstruction 79
Results 80
Discussion of Measured Error 82
Discussion of Failures 83
Chapter Six Conclusions and Future Work 85
Conclusions 85
On Chapter Two 85
On Chapter Three 86
On Chapter Four 86
On Chapter Five 87
Benediction 88
List of References 89

Vita..... 103

LIST OF TABLES

Table 2.1. Hiden gas library. 19

Table 2.2. Carrier gases and their specific heat capacities. 32

Table 3.1. Initial gas pressures and resulting flow conditions in the HXT for the TDLAS measurements. 39

Table 3.2. Equilibrium conditions for the post-normal shock region. 39

Table 3.3. Transitional band information for the three main NO peaks. 41

Table 3.4. Recovered frozen temperatures for each analyzed run. 49

Table 3.5. Approximate equilibrium distances for the HXT runs. 53

Table 5.1. Review of tomographic LAS literature. 70

Table 5.2. Review of sparse tomographic LAS literature. 71

LIST OF FIGURES

Figure 1.1. (a) Upward portion of a cycle of the spectrum and (b) recovered spectral fit plotted for absorbance. 2

Figure 1.2. Comparison of two modeled absorbance curves showing the agreement between the RVT and HITRAN (equilibrium temperature, Eq) models at equal temperatures and disparity at unequal temperatures. 9

Figure 1.3. Modulated WMS signal atop the carrier signal. 10

Figure 1.4. Wavenumber as a function of time fit from simulated data. 10

Figure 1.5. Phantom data iteratively aligned with experimental data. 11

Figure 1.6. WMS 2f data for the reference (stagnant) and angled (moving) fluids. 12

Figure 2.1. Experimental visualization with important components labeled. Green and red lines show exaggerated incident and reflected beams across the mirrors. The gas inlet and outlet of the Herriott cell are marked. 20

Figure 2.2. Visible light passing through the Herriott cell to illustrate the path taken by the 1654 nm laser. 21

Figure 2.3. Top-down diagram of the cell setup. 22

Figure 2.4. Recovered concentration evolution of methane via TDLAS of the pyrolyzed sample with error bars. 23

Figure 2.5. Methane transmission spectra as temperature increases. 24

Figure 2.6. TDLAS CH_4 concentration results compared with normalized MS result measuring AMU 15. 25

Figure 2.7. Methane production from pyrolysis of samples at increasing heating rates. . 26

Figure 2.8. Raw results from MS concerning the first few AMUs at $Q = 5\ °C/min$..... 26

Figure 2.9. Recovered concentrations of the most prominent gases at $Q = 5\ °C/min$. ... 28

Figure 2.10. Recovered concentrations of gases with a middling presence at $Q = 5\ °C/min$. 28

Figure 2.11. Recovered concentrations of gases with a minor presence at $Q = 5\ °C/min$. 28

Figure 2.12. Breakdown of normalized mass loss contributions by compound with percentage values listed. 29

Figure 2.13. AMU of 28 as measured by the mass spectrometer. The dashed-line corresponds roughly to a furnace temperature of $500\ °C$. 30

Figure 2.14. Value of methane intensity at varying temperatures. To note, prior to combustion, the signal is at its maximum. As the furnace continues heating up, the intensity drops significantly to a minimum around $580\ °C$ before steadily rising back up by 820 °C. 30

Figure 2.15. Water vapor signal intensity for a range of temperatures. To note, the signal intensity does not change dependent on the temperature..... 31

Figure 3.1. The components of the Texas A&M HXT facility [44]. 36

Figure 3.2. (a) Dimensioned drawing of the Mach stem generator with representative flow structures and laser location, (b) a photograph as installed in the HXT test-section (viewed from the side), and (c) Schlieren image visualizing Mach stems in steady state from run 221 (with mirrors for NO and atomic oxygen silhouetted). ... 38

Figure 3.3. A diagram showing the beam path of the diode laser beam with respect to the tunnel and model as well as the concurrent schlieren setup. 38
Figure 3.4. Baseline signal and transmitted NO signal from Run 219. 40
Figure 3.5. Measurable bands by the QCL. 41
Figure 3.6. Flowchart showing the operations for data processing. 41
Figure 3.7. The baseline spectrum is in blue and the transmitted spectrum is in red. Shown are progressive (nonconsecutive) selections of the transmitted spectra. 42
Figure 3.8. Run 219, 6^{th} down-cycle measurement. 43
Figure 3.9. Run 220, 5^{th} down-cycle measurement. 43
Figure 3.10. Run 221, 4^{th} up-cycle measurement. 43
Figure 3.11. Best fit for noisy, low-concentration NO data in run 221, 14^{th} up-cycle measurement shown here as an illustration of data that were discarded. 45
Figure 3.12. Highlighted peaks for integration resulting in a ratio purely as a function of temperature. 45
Figure 3.13. R(Tr, Tv) as shown in Eq. (50) and the recovered Tr and Tv values..... 45
Figure 3.14. Temperature evolution across run 219. 47
Figure 3.15. Temperature evolution across run 220. 47
Figure 3.16. Temperature evolution across run 221. 47
Figure 3.17. Schlieren images throughout steady state of run 221 from 0.986 to 1.243 ms with beam-posts for NO and atomic oxygen detection silhouetted. 48
Figure 3.18. Concentration changes for NO across steady state for three of the runs of the HXT. 49

Figure 3.19. Reduced NO concentration. 49

Figure 3.20. Reduced run 219 rotational and vibrational temperatures. 51

Figure 3.21. Reduced run 220 rotational and vibrational temperatures. 51

Figure 3.22. Reduced run 221 rotational and vibrational temperatures. 51

Figure 3.23. Equilibrium temperature fit for some HXT data. 54

Figure 3.24. Temperature separation behind a normal shock for translational (Tt), rotational (Tr), and vibrational (Tv). 55

Figure 4.1. Experimental setup of the laser across the tunnel. The reference cell is shown. 59

Figure 4.2. Velocity shift measured at 25 m/s with hot-wire anemometer and recovered at 24 m/s with WMS velocimetry. 60

Figure 4.3. Recovered velocity from the measured CO in the tunnel. 61

Figure 4.4. Recovered mole fraction from the measured CO in the tunnel. 62

Figure 4.5. Original arcjet tunnel setup. 63

Figure 4.6. Velocity calculated from the tunnel using unaided LAS. 63

Figure 4.7. Velocity using an amplifier on the orthogonal beam. 63

Figure 4.8. Two versions of the table-top setup. In (a), the orthogonal non-shifted beam is maintained. In (b), the beamsplitter and mirrors are arranged to maximize the shift measured. 64

Figure 4.9. Three runs from the Mach 1 jet on the table-top experiment. All three answers are substantially different. 65

Figure 4.10. Wavenumber ν as a function of wavelength λ. 65

Figure 4.11. Velocity from Mach 1 jet utilizing CO. Beams ‘Gamma’ and ‘Theta’ refer to the setup in Fig. 4.8. 65
Figure 5.1. Combustion experiment with a) equivalence ratios and b) setup. 72
Figure 5.2. Diagnostic setup with 1900 cm-1 (green) and 1853 cm-1 (blue) laser beams. 72
Figure 5.3. Diagnostic setup with 1900 cm-1 laser offsets in red. 74
Figure 5.4. Spectral range for 1900 cm-1 (green) and 1853 cm-1 (blue) lasers. 74
Figure 5.5. Laser absorption spectrums for nitric oxide (in red), water (in blue), and the convolved sum (in black). 75
Figure 5.6. Impact of equivalence ratio φ on concentration. 76
Figure 5.7. Ratio of peaks 1 and 4 for various convolutions. 78
Figure 5.8. Deconvolution in SLATE. 78
Figure 5.9. ART in SLATE. 78
Figure 5.10. Temperature and concentration recovery in SLATE. 79
Figure 5.11. Experiment reconstruction in SLATE. 80
Figure 5.12. SLATE reconstruction of Hencken burner temperature and concentration. 81
Figure 5.13. SLATE reconstruction of NO concentration molecules/cm3. 81
Figure 5.14. SpectraPlot analysis of NO, H_2O, and CO. The largest peak is CO. 83

CHAPTER ONE

INTRODUCTION

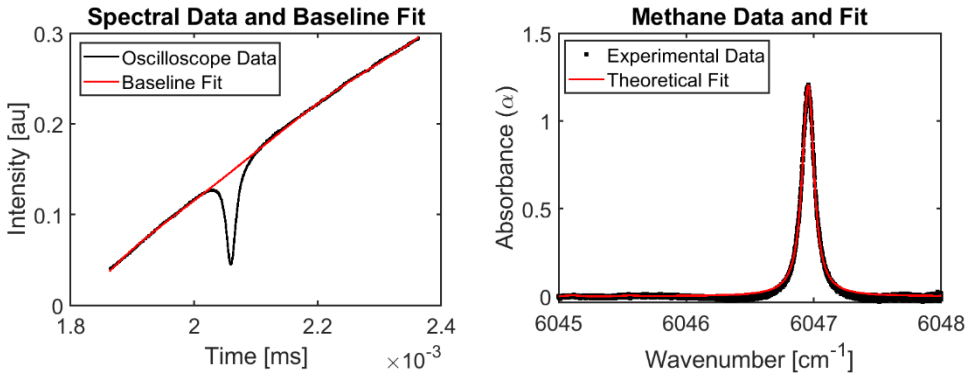
Tunable Diode Laser Absorption Spectroscopy

Tunable diode laser absorption spectroscopy (TDLAS), often just LAS, is a technique used for measuring material properties of fluids such as concentration, temperature, and pressure. This diagnostic tool employs a tunable diode laser to produce a range of wavelengths that scan across absorption features of a target molecule. As the laser beam passes through the pathlength of the experiment, a receiving photodiode measures the intensity of light absorption by the present gas molecules. LAS offers high resolution in regard to gas concentration and fast response times, making it particularly effective for detecting low concentrations of gases. Its non-intrusive nature and ability to provide real-time measurements further enhance its utility in research and industrial settings.

Prior LAS experiments have been used to measure temperature and concentration in unconventional experimental setups [1], recovery of physical gas parameters [2], and distributions across the line-of-sight [3,4]. This work expands on these ideas and improves them where possible.

By utilizing the Beer-Lambert law, shown in Eq. (1), which relates the absorption of light to the properties of the material through which it is traveling, LAS can calculate the concentration of the target gas based on the measured absorbance at specific wavelengths. The function is exponential, as light is absorbed logarithmically through a medium.

$$\tau_i = \frac{I_{t,i}}{I_0} = \exp[\alpha_i] = \exp[-n\sigma_i L] \quad (1)$$



(a) **(b)**

Figure 1.1. (a) Upward portion of a cycle of the spectrum and (b) recovered spectral fit plotted for absorbance.

Here, the recovered transmitted spectrum τ is a value between 0 and 1 for some wavenumber transition i. Through the absorbing medium, the transmitted signal is I_t (arbitrary units), I_0 (identical arbitrary units) is the signal without an absorbing species present, α the absorbance spectrum, n the molecular density of the absorbing species in $[\text{molecules/cm}^3]$, σ the absorption cross-section in $[\text{cm}^2]$, and L the laser pathlength through the absorbing species in $[\text{cm}]$. Fitting experimental data with a theory line (knowing L and σ) recovers n. As shown in **Figure 1.1**, detection limits in the parts-per-billion ($[\text{ppb}]$) range make LAS ideal for measuring the absolute concentration (e.g. $[\text{molecules/cm}^3]$) of trace gases.

Absorption cross-section σ, heavily dependent on temperature, is derived via Eqs. (2 – 3),

$$\sigma_i = \sum_j S_i(T) g_{V_{ij}} \tag{2}$$

$$S_i(T) = S_i(T_0) \frac{Q(T_0)}{Q(T)} \exp\left[-c_2 E_i'' \left(\frac{1}{T} - \frac{1}{T_0}\right)\right] \frac{1 - \exp[-c_2 \nu_i / T]}{1 - \exp[-c_2 \nu_i / T_0]} \tag{3}$$

With ν_i being the wavenumber in $[\mathrm{cm}^{-1}]$ for transition i, c_2 the second radiation constant equal to 1.4387769 $[\mathrm{cm} \cdot \mathrm{K}]$, T the temperature in [K], T_0 the reference temperature of 296 [K], $Q(T)$ the molecular partition function of the absorbing species at some temperature, and E'' the lower-state transition energy in $[\mathrm{cm}^{-1}]$. The Voigt convolution function g_V is given in Eqs. (4 – 5) with resolved units of [cm] [5].

$$g_{V_{ij}} = f_{V\,ij} \frac{\nu_j}{\nu_i} \frac{\tanh\left(\frac{c_2 \nu_j}{2T}\right)}{\tanh\left(\frac{c_2 \nu_i}{2T}\right)} \tag{4}$$

$$f_{V\,ij} = c_{L_i} \frac{\alpha_{V_i}}{\pi\left(\left(\nu_j - \nu_i\right)^2 + \alpha_{V_i}^2\right)} + c_{G_i} \sqrt{\frac{\ln 2}{\pi}} \frac{\exp\left[-\frac{\ln 2\ \left(\nu_j - \nu_i\right)^2}{\alpha_{V_i}^2}\right]}{\alpha_{V_i}} \tag{5}$$

Here, ν_j is an accounting of all wavenumbers from $-\infty$ to $+\infty$ $[\mathrm{cm}^{-1}]$; realistically this is roughly the wavenumber bounds of the laser scan range. The broadening term α_{V_i} is the Voigt broadening defined in Eq. (8). The c_L and c_G terms are the Gaussian and Lorentzian constants of the broadenings shown in Eq. (6). These terms are also discussed in depth in literature [6].

$$\begin{aligned} c_{L_i} &= 0.6818817 + 0.6129331 d_i - 0.1838439 d_i^2 - 0.1156844 d_i^3 \\ c_{G_i} &= 0.3246017 - 0.6182531 d_i + 0.1768139 d_i^2 + 0.1210944 d_i^3 \end{aligned} \tag{6}$$

Where *d* is a dimensionless ratio of the Lorentzian and Doppler/Gaussian broadenings,

$$d_i = \frac{\alpha_{L_i} - \alpha_{D_i}}{\alpha_{L_i} + \alpha_{D_i}} \tag{7}$$

All broadening terms are in units of $[\mathrm{cm}^{-1}]$. The Voigt broadening is given by,

$$\alpha_{V_i} = 0.5346 \alpha_{L_i} + \sqrt{0.2166 \alpha_{L_i}^2 + \alpha_{D_i}^2} \tag{8}$$

The Doppler/Gaussian and Lorentzian broadening coefficients are found then in Eqs. (9 – 14).

$$\alpha_{D\,i} = \sqrt{\alpha_{\text{laser}}^2 + \alpha_{\text{thermal},i}^2} \tag{9}$$

Thermal broadening, given in Eq. (10), is the standard Doppler broadening unaffected by the laser broadening. The laser broadening in Eq. (11) is a product of the laser itself and is often negligible due to its small size.

$$\alpha_{\text{thermal},i} = \frac{\nu_i}{c}\sqrt{\frac{2N_A k_B T \ln 2}{M_i}} \tag{10}$$

$$\alpha_{\text{laser}} = \frac{\Delta f}{c - \Delta f \lambda} \tag{11}$$

Here, the known laser optical linewidth Δf is given in $[\text{Hz}]$, the laser wavelength λ is in $[\text{cm}]$, and the speed of light c is in units of $[\text{cm/s}]$. Molecular weight M_i is in $[\text{g/mol}]$ and is the most prominent isotopologue of transition i centered at ν_i; N_A and k_b are the Avogadro and the Boltzmann constants as $6.022140858 \times 10^{23}$ $[\text{mol}^{-1}]$ and $1.3806488 \times 10^{-16}$ $[\text{erg/K}]$ respectively.

Lorentzian broadening in Eq. (12) is the sum of the pressure broadening and natural broadening. The pressure (or collisional) broadening will depend on the concentration of the absorbing medium, the total pressure of the gas, and the temperature of the system as shown in Eq. (14). The natural broadening is a consequence of the Einstein A coefficient in Eq. (13).

$$\alpha_{L_i} = \alpha_{\text{pressure},i} + \alpha_{\text{natural},i} \tag{12}$$

$$\alpha_{\text{natural},i} = \frac{\mathcal{A}_i}{2\pi c} \tag{13}$$

$$\alpha_{\text{pressure},i} = \left[(1-\chi)\gamma_{\text{air},i} + \chi\gamma_{\text{self},i}\right] P \left(\frac{T_0}{T}\right)^{n_{\text{air},i}} \tag{14}$$

Where the Einstein A coefficient $\mathcal{A}$ is tabulated in the HITRAN database [7] for measured lines in units of $[\text{s}^{-1}]$, the γ_{air} and γ_{self} terms are the air-broadened and self-broadened half-widths at half-maximum (HWHM) per transition i given in $[\text{cm}^{-1}/\text{atm}]$, and $n_{\text{air},i}$ is the temperature dependence coefficient. The pressure broadening uses pressure in $[\text{atm}]$ and temperature in $[\text{K}]$. The mole-fraction may be related to the molecular concentration in local thermodynamic equilibrium via Eq. (15).

$$\chi = \frac{nk_B T}{P} \tag{15}$$

Where the pressure is in [Pa] and the Boltzmann constant is $1.3806488 \times 10^{-23}$ [J/K].

Ro-Vibrational Temperature Model

In high-enthalpy flows, temperatures at local thermodynamic equilibrium no longer accurately reflect the behavior of the system as seen experimentally. Energy no longer takes the role only of kinetic but now fills the niche of rotational (spinning in space), vibrational (diatomic oscillation), translational (lateral movement), and electronic (separate electron levels) temperatures alike.

A ro-vibrational temperature (RVT) model was created to better understand how the absorbance spectrum of nitric oxide (NO) changes in both rotational and vibrational temperature. In this model, translational temperature is assumed to be equal to that of rotational temperature, while the electronic temperature component is considered negligible as all energy transitions within the experiment are expected to occur in the ground state.

Due to the differences in vibrational and rotational temperature, the temperature present in Eqs. (4 – 15) is replaced with the rotational component T_r.

The spectral line intensity $S(T)$ in $[\mathrm{cm}^{-1}/\mathrm{molecule}\cdot\mathrm{cm}^{-2}]$ given in Eq. (3) is now assumed to be dependent on both rotational and vibrational energies, as shown in Eq. (16).

$$S_i(T_r,T_v) = S_i(T_0)\frac{Q(T_0,T_0)}{Q(T_r,T_v)}\exp\left[-c_2\left(\frac{F_i''}{T_r}+\frac{G_i''}{T_v}-\frac{F_i''+G_i''}{T_0}\right)\right]\times \frac{1-\exp\left[-c_2\left(\frac{\Delta F_i}{T_r}+\frac{\Delta G_i}{T_v}\right)\right]}{1-\exp\left[-c_2\frac{(\Delta F_i+\Delta G_i)}{T_0}\right]} \tag{16}$$

Where the partition function Q is calculated as in Eq. (17) taken from Hanson [8],

$$Q(T_r,T_v) = Q_{\mathrm{elec}}Q_{\mathrm{vib}}Q_{\mathrm{rot}} = (4)\left(\frac{3}{1-\exp[-\theta_v/T_v]}\right)\left(\frac{T_r}{\theta_r}\right) \tag{17}$$

Here, θ_v and θ_r are the vibrational and rotational characteristic temperatures in [K] respectively. The numerator of the vibrational partition function is the statistical degeneracy of the most abundant isotopological vibrational band as from the HITRAN database. The value of the electronic partition function comes from Eq. (18).

$$Q_{\mathrm{elec}} = (2S+1)\left(2+\delta_{0,\Lambda}\right) \tag{18}$$

The value of $\delta_{0,\Lambda}$ depends on the quantum number Λ, as described in reference [8]. The $\delta_{0,\Lambda}$ value for ground state NO is zero while the value for $2S+1$ for the $\mathrm{X}^2\Pi$ transition of NO is 2. The characteristic temperatures of the vibrational and rotational modes are respectively shown in Eq. (19) alongside the moment of inertia in Eq. (20).

$$\theta_v = c_2\omega_e; \qquad \theta_r = \frac{h^2}{8\pi^2 I k_B} \tag{19}$$

$$I = \frac{m_1 m_2}{m_1 + m_2} r_0^2 \tag{20}$$

Where ω_e is the first harmonic oscillator vibrational constant of NO, m_1 and m_2 are the masses of the oxygen and nitrogen atoms in [kg], r_0 is the distance between them in [m], and h and k_B are the Planck and Boltzmann constants as $6.62607015 \times 10^{-34}$ [J/Hz] and $1.3806488 \times 10^{-23}$ [J/K] respectively.

From the reference [9], the vibrational (G) and rotational (F) energies in Eq. (16) are defined via Eqs. (21 – 28).

$$G(v) = \omega_e(v + 0.5) - \omega_e x_e(v + 0.5)^2 - \frac{\omega_e}{2} + \frac{\omega_e x_e}{4} \tag{21}$$

Where v is the vibrational number of the transition and $\omega_e x_e$ is the anharmonicity constant of NO. The vibrational energy G, given in [cm^{-1}], is reduced by the zero-point energy with $G(v = 0)$. This is to more closely model the HITRAN database and the energies listed there. The rotational energy is reviewed in Eqs. (22 – 26).

$$F''(J'') = B_v''[(J'' + 0.5)^2 - 1] - D_v''[(J'' + 0.5)^4 - (J'' + 0.5)^2 + 1] \mp B_v''\sqrt{ł''} \tag{22}$$

The terms B_v and D_v are vibronic constants for NO documented both in Reisel's work [10] as well as in the NIST database with values of $B_v'' = 1.69619$ [cm^{-1}] and $D_v'' = 5.326 \times 10^{-6}$ [cm^{-1}] respectively . In the equation, the top symbol of the $\mp$ is for the $\Omega = 1/2$ state, with the bottom symbol being for the $\Omega = 3/2$ state; similarly for the double-symbol in Eqs. (24, 26). The main bulk of the rotational energy calculation is shown below, with the ár-rune ł defined in Eq. (23), the ground state rotational energy term Y_v in Eq. (24) and the subsequent terms for hyperfine transitions in Eqs. (25 – 27).

$$\text{ϟ}'' = \frac{(Y_v'' - 2)^2}{4} + [(J'' + 0.5)^2 - 1]\begin{pmatrix} 1 + 2\mu''[2(J'' + 0.5)^2 - Y_v''] + \\ \mu''^2\{[2(J'' + 0.5)^2 - 1]^2 - 1\} \end{pmatrix} \quad (23)$$

$$Y_v'' = \frac{\tilde{A} \pm C(J'' - 0.5)^2}{B_v''} \quad (24)$$

$$\mu'' = \frac{D_v''}{B_v''} \quad (25)$$

$$\phi(J, Y_v, \text{ϟ}) = 0.5(J + 0.5)\left\{\left[\frac{2 - Y_v}{2\sqrt{\text{ϟ}}} \mp 1\right]\left[\frac{\tilde{P}}{2} + \tilde{Q}\right] + \frac{\tilde{Q}}{\sqrt{\text{ϟ}}}[(J + 0.5)^2 - 1]\right\} \quad (26)$$

$$F_{\Omega e} = F_\Omega - \phi; \qquad F_{\Omega f} = F_\Omega + \phi \quad (27)$$

Where e and f represent the positive and negative parity recorded in the HITRAN/HITEMP databases. The values of the constants mentioned in the equations above and below are all tabulated in Reisel's work [10] where $C = -1.1871 \times 10^{-3}$ [cm^{-1}], $\tilde{A} = 123.0372$ [cm^{-1}], $\tilde{P} = -1.1882 \times 10^{-2}$ [cm^{-1}], and $\tilde{Q} = -5.43 \times 10^{-5}$ [cm^{-1}]. The upper-state vibrational energy is calculated in the same means as Eq. (21) only using v' in lieu of v'' alongside the corresponding constants; the upper-state rotational energy for either spin-state is found with Eq. (28):

$$F'_{\Omega=\frac{1}{2}}(J') = B_v'(J' + 0.5)(J' - 0.5) - D_v'(J' + 0.5)^2(J' - 0.5)^2 + 0.5\tilde{\gamma}\,(J' - 0.5) \quad (28)$$
$$F'_{\Omega=\frac{3}{2}}(J') = B_v'(J' + 0.5)(J' + 1.5) - D_v'(J' + 0.5)^2(J' + 1.5)^2 - 0.5\tilde{\gamma}(J' + 1.5)$$

With parity being accounted for in the same manner as the lower-state energies, simply substituting the upper-state values where, within Eqs. (24 – 27), the lower-state are written. The values of the constants are $B_v' = 1.98685$ [cm^{-1}], $D_v' = 5.43 \times 10^{-6}$ [cm^{-1}], $\tilde{\gamma} = -1.252 \times 10^{-2}$ [cm^{-1}]. Shown in **Figure 1.2** are the results of this model.

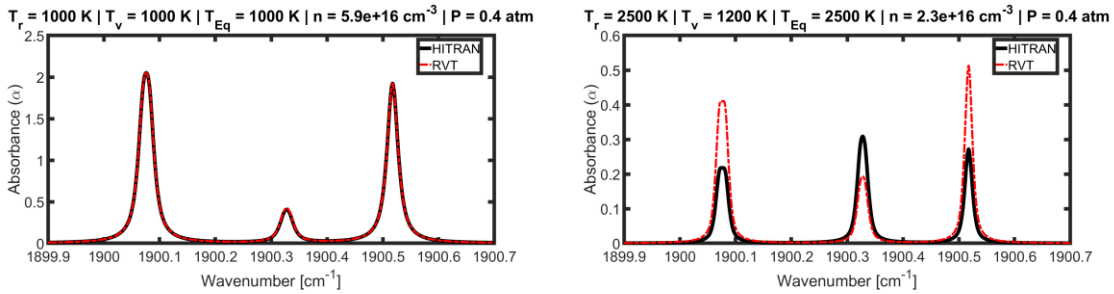


Figure 1.2. Comparison of two modeled absorbance curves showing the agreement between the RVT and HITRAN (equilibrium temperature, Eq) models at equal temperatures and disparity at unequal temperatures.

The two absorbance curves in **Figure 1.2** (from using the RVT model and the equilibrium model) show how the model responds to different temperature inputs while the NO concentration is maintained as constant and the pressure is held constant at mole-fraction $\chi = 0.02$ and pressure $P = 0.4$ [atm].

Wavelength Modulated Spectroscopy

Wavelength modulated spectroscopy (WMS) is a technique to improve LAS signal quality and measurement sensitivity by leveraging the non-linear effects of harmonic oscillations. These harmonic non-linearities can be related to material characteristics in much the same way as recovered by the Beer-Lambert Law [11,12]; to wit, they depend on pressure, temperature, and concentration.

To perform WMS, a high-frequency sinusoid is modulated atop the carrier signal as shown in **Figure 1.3**. The baseline signal $I_0(t)$ may be converted to a function of wavenumber $I_0\big(\nu(t)\big)$ using Eq. (29) to solve for $\nu(t)$.

$$\nu(t) = a_0 + a_1 t + a_2 t^2 + a_3 t^3 + a_4 t^4 + a_5 \cos(2\pi f t + a_6) \tag{29}$$

The a constants are found via fitting Eq. (29) within some tolerance to experimental data as shown in **Figure 1.4**.

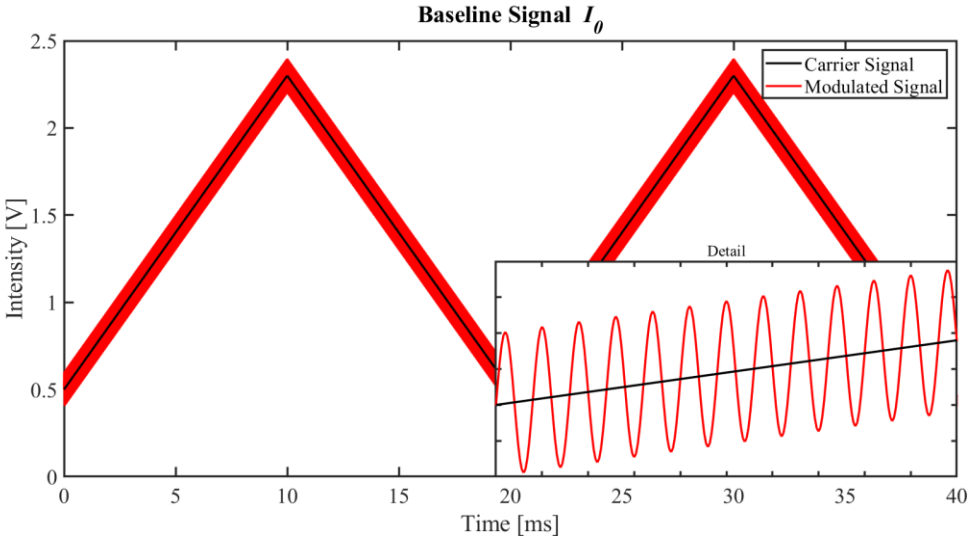


Figure 1.3. Modulated WMS signal atop the carrier signal.

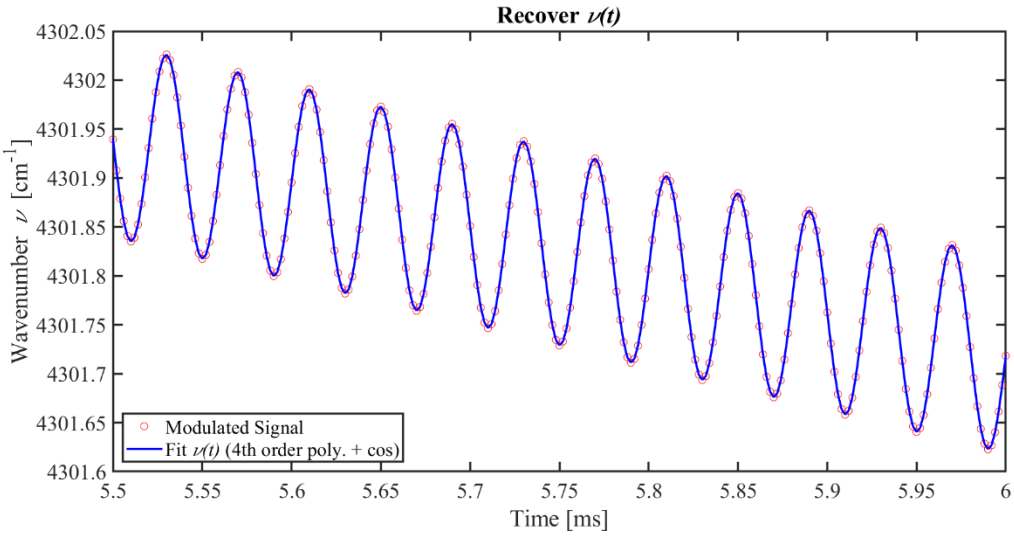


Figure 1.4. Wavenumber as a function of time fit from simulated data.

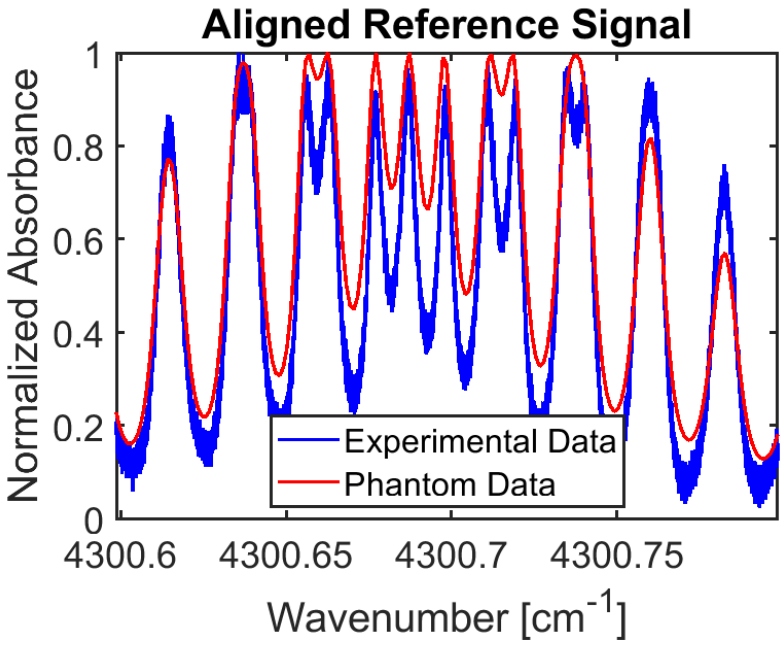


Figure 1.5. Phantom data iteratively aligned with experimental data.

With $\nu(t)$, a simulated phantom (fake) transmitted intensity $I_t(\nu(t))$ may be created and aligned with the measured (real) $I_t(t)$ from the experiment. This process is highlighted in **Figure 1.5**.

Recovering velocity with WMS velocimetry necessitates only that the phases of the transmitted intensities be aligned to each other. The magnitudes need not match. The phantom data are aligned in this manner to recover a noiseless approximation of the experiment to better recover the velocity.

The phantom approximation is passed into a lock-in amplifier (LIA) to recover the varying harmonic modes; in most real applications of WMS, these are the second and first harmonics. The harmonic modes are found using Eqs. (30 – 32),

$$W = \alpha \exp[i(n2\pi f_{\mathrm{mod}} t)] \tag{30}$$

$$X = \mathrm{Re}[W]; \quad Y = \mathrm{Im}[W] \tag{31}$$

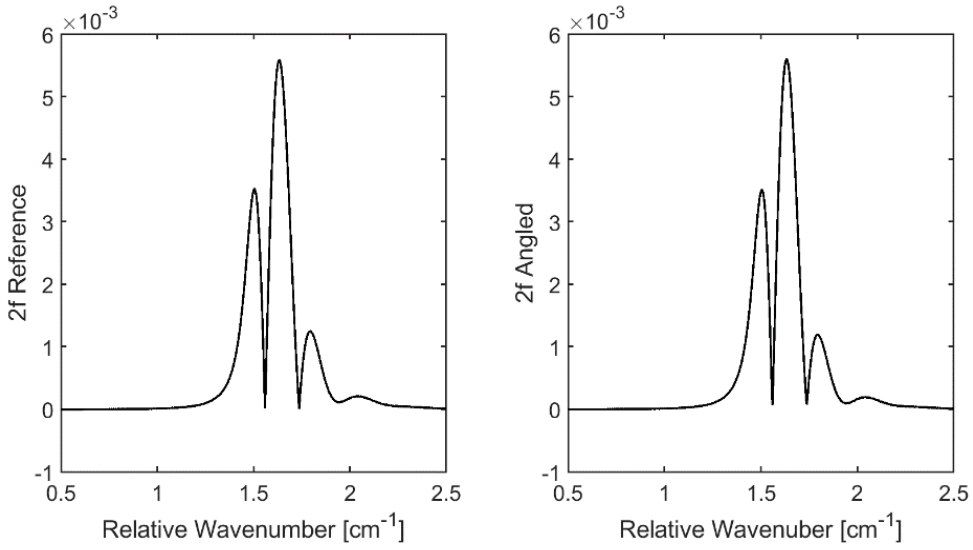


Figure 1.6. WMS 2f data for the reference (stagnant) and angled (moving) fluids.

$$R_{\mathrm{WMS}} = \sqrt{X^2 + Y^2} \tag{32}$$

Where α is the phantom absorbance recovered from I_t, n is an integer harmonic number, f_{mod} is the modulation frequency of the sinusoid in [Hz], and t is time in [s]. The signal R_i, then, is solved for the chosen harmonic.

Equations (30 – 32) create the second harmonic mode as shown in **Figure 1.6**. Displayed are two curves, one for a reference signal (a signal through stationary fluid) and an angled signal (the signal angled through swiftly moving fluid).

Shown in the figure are the reference and angled signals of a small jet measured at $25\ [\mathrm{m/s}]$ by a hot-wire anemometer for the purposes of calibrating the system. Using Eq. (33), the difference in wavenumber between two selected points is directly related to the velocity.

$$U = \frac{c\Delta\nu}{\nu_0 \cos\theta} \tag{33}$$

Here, c is the speed of light in $[\mathrm{cm/s}]$, $\Delta\nu$ is the measured change in wavenumber in $[\mathrm{cm^{-1}}]$, ν_0 is the transition center in $[\mathrm{cm^{-1}}]$, and θ is the beam angle with respect to the flow direction. To improve accuracy, typically the velocities of several measurements are averaged.

Tomographic Reconstruction

When path-averaged LAS is coupled with algebraic reconstruction tomography (ART) and two-line thermometry, individual "cells" of concentration and temperature may be resolved. This begins by obtaining experimental values of absorbance via the first part of Eq. (1), enabling integration of the absorbance α_i across all wavenumbers ν. The integrated absorbance A_i is recovered as in Eq. (34).

$$A_i = \int_{-\infty}^{\infty} \alpha_i d\nu \tag{34}$$

Where α is the experimental absorbance from Eq. (1). To resolve A into individual cells, elementary tomography is introduced. Modern methods of ART are discussed in Hansen [13], while thorough summaries of tomographic reconstruction techniques applicable for sparse LAS experiments are given by Cai [14] and Guha [15]. The basic premise of ART solves for $\bar{x}_i$ as in Eq. (35) [13,16]:

$$\bar{A}\bar{x}_i = \bar{b}_i \tag{35}$$

Where $\bar{A}$ is a geometry matrix and $\bar{b}_i$ is a matrix of lower-dimensional information. In this work, $\bar{b}_i$ is the path-integrated, wavenumber-integrated absorbance A_i from Eq. (34) reformatted as a sinogram to account for the experiment geometry given in $\bar{A}$. Equation (36) is solved for the m^{th} number spatial beam via iteration to a maximum k. When solved, $\bar{x}_i$ is the two-dimensional surface of integrated absorbances for spectral transition

(peak) i corresponding to $\bar{b}_i$. The relaxation parameter λ_0 is used to manually adjust the fitting and is fixed at a constant value of 0.1.

$$\bar{x}_{k+1} = \bar{x}_k + \lambda_0 \bar{a}_m \frac{b_m - (\bar{a}_m \cdot \bar{x}_k)}{(\bar{a}_m \cdot \bar{a}_m)} \tag{36}$$

With individual cells of integrated absorbance across the geometry recovered, two-line thermometry may be used to reconstruct a temperature profile. Two-line thermometry is a simple technique to recover temperature independent of pressure and concentration. A ratio of integrated absorbances for spectral transitions (peaks) i and j can be constructed using Eq. (37):

$$R_{ij} \equiv \frac{A_i}{A_j} = \frac{n\sigma_i L}{n\sigma_j L} = \frac{S_i(T)}{S_j(T)} \tag{37}$$

For the same measurement, the ratio of peaks becomes a ratio of spectral line intensities and solely dependent on the temperature. Theoretical data from the HITRAN/HITEMP database are ratioed via Eq. (37) to generate a theoretical ratio R_{ij}. Each ratio represents a unique temperature; experiment ratios are compared to this theoretical ratio to recover the temperature.

CHAPTER TWO

MASS SPECTROMETRY AND LASER ABSORPTION SPECTROSCOPY INSTRUMENTATION FOR CHARACTERIZATION OF CARBON PHENOLIC COMPOSITES PYROLYSIS

Motivation

To measure, simultaneously, all present gases from an outgassing of a carbon phenolic (carbon-carbon compound) sample. To minimize equipment involved while still recovering the absolute concentrations of every molecule produced by the pyrolysis. To monitor ablative chemistry of nominal heat-shield material and how various corrosive and destructive compounds are produced as the material undergoes thermal dissociation.

Abstract

An instrument has been developed by combining tunable diode laser absorption spectroscopy (TDLAS) and mass spectrometry (MS) to characterize high-temperature material pyrolysis. Pyrolysis exhaust products are measured *in situ* using both TDLAS and MS to establish a correlation of their absolute concentrations, such that the concentrations of all species can be quantified. In this experiment, commercially available carbon phenolic composites underwent pyrolysis processes for the demonstration of the platform. The gas species of water vapor, methane, and carbon monoxide are targeted at room temperature via three lasers centered at 1392, 1654, and 2327 [nm], respectively. The absolute concentration of the gases targeted by the three lasers are measured by TDLAS ($[\mathrm{molecules/cm^3}]$). Mass spectrometry is employed to measure the relative abundances of all present gases, which are then converted into absolute concentrations via correlation with the measurements obtained from TDLAS for water vapor, methane, and carbon monoxide. The temporal evolution of the concentrations of all species is recorded alongside thermal changes measured by a thermocouple connected to the interior of the pyrolysis furnace.

Introduction

As the utilization of carbon materials in aerospace, electronics, energy storage, and medical devices becomes more prevalent [17–19], it is of paramount importance to understand how these materials respond under substantial thermal and mechanical stresses, which not only affect their structural integrity but also influence the generation of various gaseous byproducts. The lack of comprehensive and quantitative measurements raises concerns about the long-term performance and safety of carbon-based components. Reproducing the extreme conditions these materials endure, such as through pyrolysis, has become a key focus of research in recent decades.

Pyrolysis is the process by which a controlled thermal dissociation of a material results in several products outgassing from the sample [20,21]. For phenolic impregnated carbon ablators, these gases consist mainly of hydrocarbons like methane, toluene, and phenol with no small amount of water vapor also produced [22]. To accurately measure the resultants from the materials under extreme heating conditions, the carbon phenolic materials are placed in a furnace and monitored up to 1100 [°C] (~ 1400 [K]). In the case of carbon phenolic materials, the pyrolysis zone of interest ranges from 400 [K] to 1200 [K], a range effectively covered by the furnace used in this study [23]. This temperature range enables a distinct decomposition of the sample, resulting in the formation of constituent gases and residual char [24–27].

Tunable diode laser absorption spectroscopy (TDLAS) is a highly sensitive technique used for measuring trace gas concentrations in various applications, including environmental monitoring, industrial process control, and atmospheric studies [8,28].

Mass spectrometry (MS) is a technique that utilizes basic principles of ionization and acceleration to compartmentalize the individual components of a gas mixture into its constituents based on the mass of each [29]. Normalizing the result of MS will yield the intensities of each measured mass relative to the others present. By coupling MS with TDLAS, the concentrations of all major gases released from the sample may be recovered as functions of both time and temperature. To account for the small concentrations released from the sample, a Herriott cell is constructed to increase the pathlength over which the gases are measured [30].

Measuring the outgassing of commercial carbon materials is crucial for a comprehensive understanding of how these materials pyrolyze, ablate, and deform under both intended and extreme conditions. Gaining insights into thermal decomposition enhances our characterization of deformation models. This research aims to leverage the complementary strengths of TDLAS and MS to measure trace amounts of methane, carbon monoxide, and water vapor—on the order of 10 parts per million ([ppm])—released from commercial carbon materials. The importance of these instruments for pyrolysis lies in their ability to provide precise and real-time measurements of gaseous species, allowing for a deeper understanding of the pyrolysis process. By combining the detailed gas characterization capabilities of TDLAS and MS, we can effectively correlate the gas measurements with the degradation and ablation processes of the materials.

Mass Spectrometry and Laser Spectroscopy

The experimental platform utilizes the *Hiden Analytical HPR-20 R&D* commercial mass spectrometer [31]. This instrument is used as purchased and is unaltered in any way. As

Table 2.1. Hiden gas library.

AMU	Measured Gases
2	$H_2 + 0.03CH_4$
14	$0.156CH_4 + 0.052N_2 + 0.007CO$
15	$0.858CH_4$
16	$CH_4 + 0.114O_2 + 0.091CO_2 + 0.064CH_3OH$
18	$H_2O + 0.019CH_3OH$
28	$N_2 + CO + 0.107C_6H_{14} + 0.065CO_2 + 0.064CH_3OH$
31	$CH_3OH + 0.056(CH_3)_2CHOH$
32	$O_2 + 0.667CH_3OH$
44	CO_2
45	$(CH_3)_2CHOH + 0.01CO_2$
57	C_6H_{14}
78	C_6H_6
86	$0.155C_6H_{14}$
91	$C_6H_5CH_3$
92	$0.785C_6H_5OH$
94	C_6H_5OH
106	C_8H_{10}
108	C_7H_8O

the gases are separated not by species but by atomic mass unit (AMU), the MS data must be interpreted using a table of species combinations to recover individual species. Given with the mass spectrometer is a calibration library of intensity contributions of varying gases shown in part in **Table 2.1**.

For heavier gases, there is often only a single compound present. With lighter AMUs, the MS often measures several compounds as with AMU 28, corresponding directly to both nitrogen and carbon monoxide and to a lesser extent carbon dioxide, hexane, and methanol. Although an AMU of 16 corresponds to methane nominally, the measurement also corresponds to small amounts of oxygen, carbon dioxide, water vapor, and methanol. The AMU of 15 is used for calibrating the result from MS with the response of TDLAS, as 15 depends solely on methane. When the corresponding methane concentration is

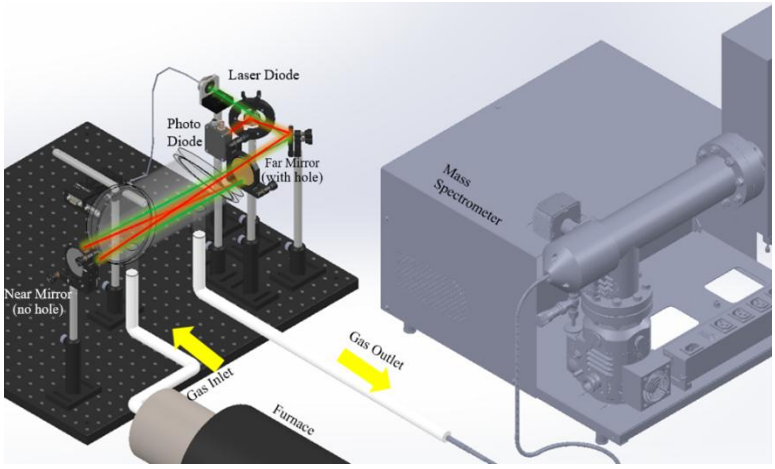


Figure 2.1. Experimental visualization with important components labeled. Green and red lines show exaggerated incident and reflected beams across the mirrors. The gas inlet and outlet of the Herriott cell are marked.

recovered in MS, it's a simple mathematical denouement to recover the absolute concentrations of every other measured gas.

Methodology

Setup

To perform LAS, laser diode/thermoelectric cooler (LD/TEC) drivers *ITC4001* from Thorlabs are used. A *Rigol DG812* arbitrary waveform generator creates triangle signals to scan a fixed range of wavenumbers. The cell setup includes a mirror system connected to the exhaust of a dilatometer furnace. The flow of the gas and the paths of the laser beam are illustrated in **Figure 2.1**.

In the Herriott mirror system, one of the mirrors (the far mirror in **Figure 2.1**, *Thorlabs CM508-200EH4-M02*) has a small hole near the top to allow a single beam both in and out. The mirrors are both concave, creating a parabolic cavity for the light to bounce within prior to exiting the cell. The windowed lenses on either side of the optical cell are

angled at the Brewster angle (around 55.6°) to prevent any laser cavitation from the lens thickness. Although laser cavitation from thick windows or lenses will distort a signal, certain angles reduce this effect.

The yellow arrows in **Figure 2.1** indicate the direction of exhaust as it exists the dilatometer furnace and enters the Herriott cell. The 1654 [nm] methane laser beam bounces between the mirrors positioned on either end of the cell (**Figure 2.2**), increasing the measured path length through the experiment from 25 [cm] to 450 [cm], as it is reflected back and forth nine times. The 1392 [nm] water vapor laser is sent perpendicularly to the cell (shown in **Figure 2.3**) in order to reduce atmospheric influence; likewise, for the carbon monoxide laser (2327 [nm]) as the mirrors do not well reflect that wavelength of light. This results in the pathlength for the water vapor and carbon monoxide lasers to be around 5 [cm] each. The exhaust then exits the cell and

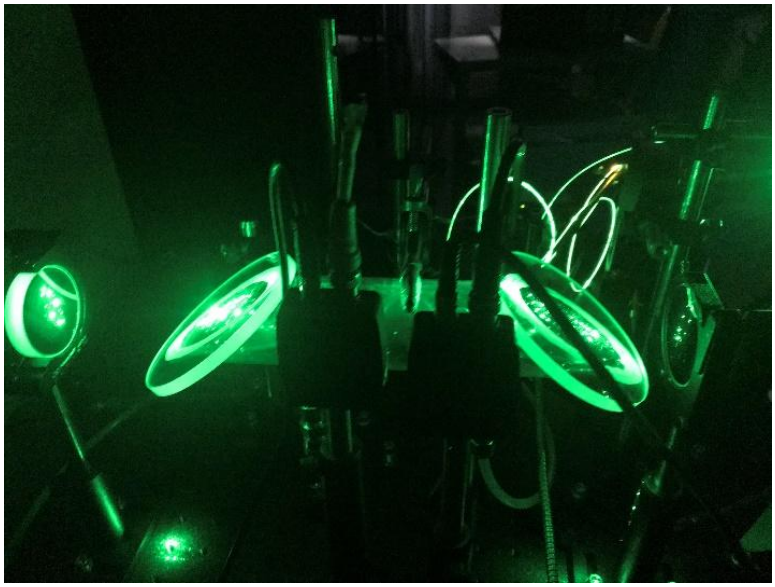


Figure 2.2. Visible light passing through the Herriott cell to illustrate the path taken by the 1654 [nm] laser.

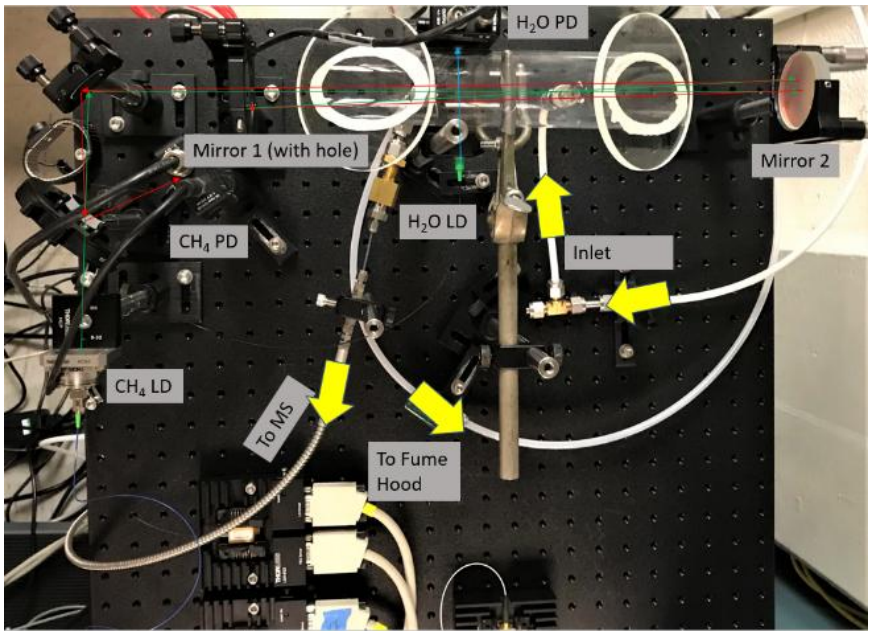


Figure 2.3. Top-down diagram of the cell setup.

flows to a fume hood where a portion of the gas is directed to the mass spectrometer. Helium constantly cycles the outgassing through the apparatus to maintain pressure. Importantly, helium is chosen for its high specific heat to protect any volatile gases released during the experiment from premature combustion (see later section *Discussion of Failures*). The gas has cooled significantly by the time it reaches the mirror system, so any effects the temperature has on the broadening of the recovered spectra are negligible, leaving only the concentration as unknown.

Procedure

For this study, a sample of *T300* carbon fiber in *SC10008* phenolic resin, supplied by C-CAT under Air Force contract, is placed inside the dilatometer furnace connected to the cell. As the furnace heats up, the carbon phenolic sample undergoes pyrolysis. Outgassing from the sample is directed into the cell via a constant flow of helium through

the whole system. As the gases pass through the laser paths, the methane, water vapor, and carbon monoxide absorb the wavelengths centered at 1654, 1392, and 2327 [nm] respectively, showing up on the connected oscilloscope. The data are analyzed in Chapter One with Eq. (1).

Results

Spectroscopic Results

To recover a detailed enough evolution curve for the concentrations of the measured gases, data are taken in intervals every $30 - 50$ [°C] as shown in **Figure 2.4**. The uncertainty bounds are the percent error of the fits. The resultant line plotted comes from fitting each of the spectra in **Figure 2.5** at the appropriate temperature measured by the thermocouple in the dilatometer via Eq. (1). The temperature on the x-axis is the temperature of the pyrolysis.

When fit, the concentration of the methane gas is recovered and may then be correlated with the intensity measured by MS as in **Figure 2.6**. Intensity is normalized by the maximum value in either curve to show the matching features more clearly. There is a

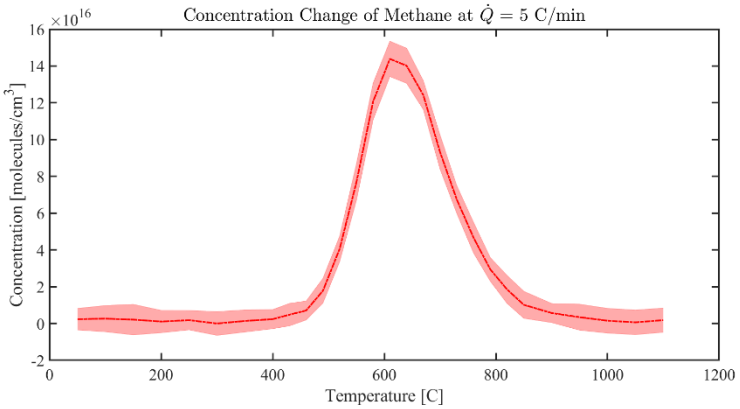


Figure 2.4. Recovered concentration evolution of methane via TDLAS of the pyrolyzed sample with error bars.

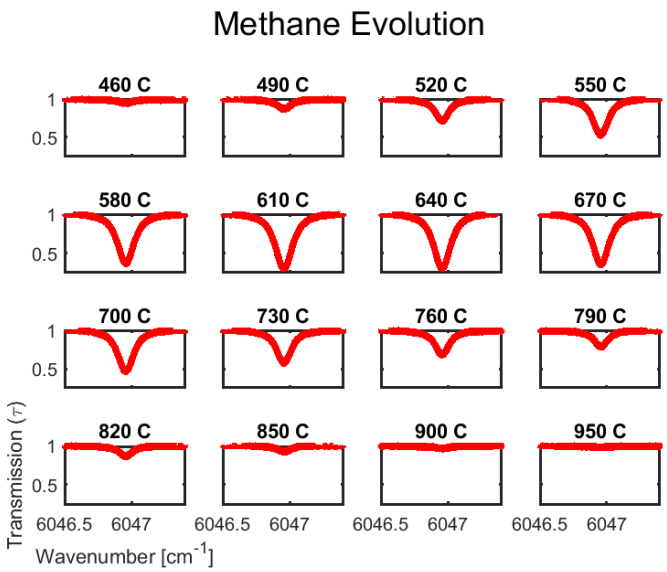


Figure 2.5. Methane transmission spectra as temperature increases.

slight shift in the x-axis to account for the length of the tubes measuring the gas in the MS versus the TDLAS. To wit, as the TDLAS diagnostics measure the gas before the MS does, the intensity measured by the MS will come at a later time than that measured by TDLAS. Correlating the time to temperature for both, then, requires a small correction amounting to no more than 10 [K] in the post-processing. Shown in **Table 2.1**, the AMU of 15 represents an independent measure of methane and no other gases. The intensity of methane recovered at this AMU is only about 86% the nominal value of the gas. Using Eq. (38), a conversion factor between MS and TDLAS is recovered,

$$C_{\mathrm{MS}} = \frac{TDLAS_x}{MS_x/0.858} \tag{38}$$

Where C_{MS} is the conversion factor and $TDLAS_x$ and MS_x are corresponding points on the curves. This factor allows for the conversion between the relative MS intensities to absolute concentration in $[\mathrm{cm}^{-3}]$.

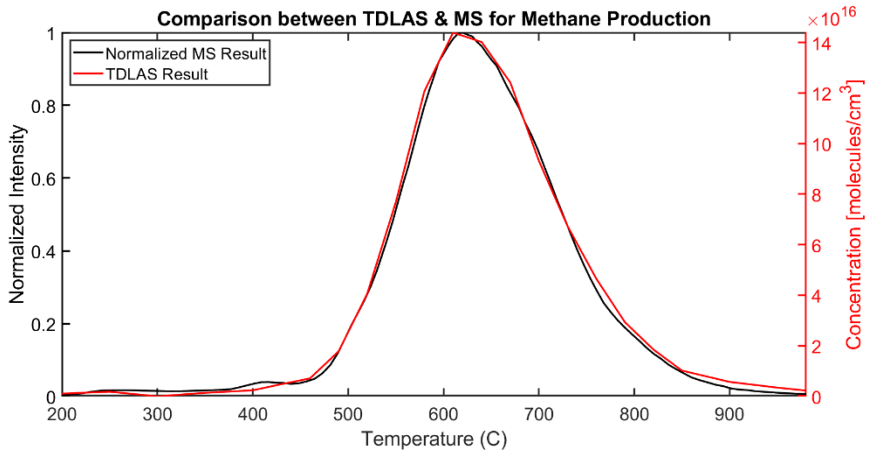


Figure 2.6. TDLAS CH_4 concentration results compared with normalized MS result measuring AMU 15.

This process is repeated for different heating rates, as shown in **Figure 2.7**. As the heating rate of the sample increases, the maximum production of methane shifts to higher temperatures as indicated by the accompanying arrow. The absolute concentrations of every measured gas may be recovered by combining Eq. (38) and **Figure 2.8**, resulting in **Figure 2.9**. This is done via deconvolving the gases in **Table 2.1** to create individual relations to the measured methane (AMU 15) to recover each gas' concentration in turn. These relations are found in Eqs. (39 – 46).

$$\mathrm{CH_4} = \frac{AMU_{15}}{0.858} \tag{39}$$

$$\mathrm{H_2} = AMU_2 - 0.03\mathrm{CH_4} \tag{40}$$

$$(\mathrm{CH_3})_2\mathrm{CHOH} = AMU_{45} - 0.012AMU_{44} \tag{41}$$

$$\mathrm{CH_3OH} = AMU_{31} - 0.056(\mathrm{CH_3})_2\mathrm{CHOH} \tag{42}$$

$$\mathrm{H_2O} = AMU_{18} - 0.019\mathrm{CH_3OH} \tag{43}$$

$$\mathrm{O_2} = AMU_{32} - 0.667\mathrm{CH_3OH} \tag{44}$$

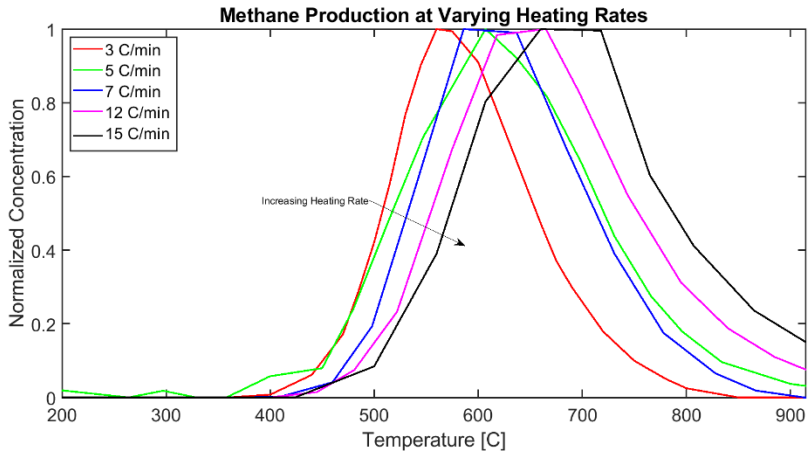


Figure 2.7. Methane production from pyrolysis of samples at increasing heating rates.

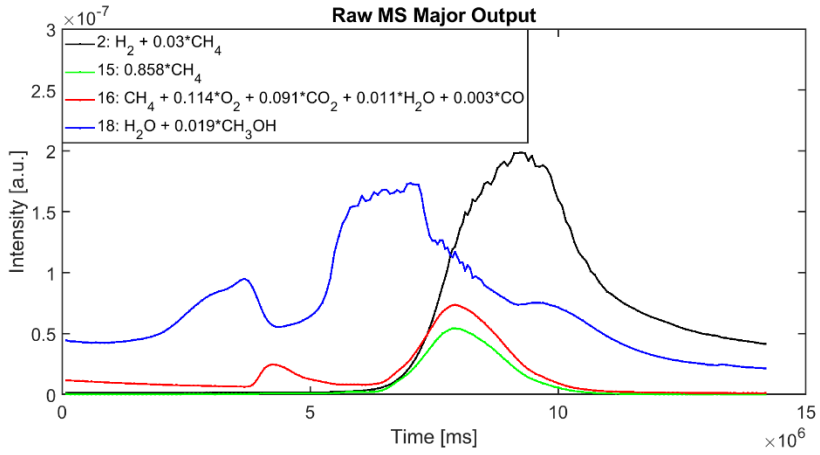


Figure 2.8. Raw results from MS concerning the first few AMUs at $\dot{Q} = 5$ [°C/min].

$$\mathrm{CO} = \frac{AMU_{16} - \mathrm{CH_4} - 0.114\mathrm{O_2} - 0.091AMU_{44} - 0.011\mathrm{H_2O}}{0.03} \tag{45}$$

$$\mathrm{N_2} = AMU_{28} - CO - 0.107AMU_{57} - 0.065AMU_{44} - 0.064\mathrm{CH_3OH} \tag{46}$$

All other relations are read directly from the mass spectrometer, as there are no other competing gases. Because the concentrations of all measured AMUs are known, the system of equations becomes trivial. Utilizing this methodology, the concentrations of the other gases are recovered as shown in **Figures 2.10 – 2.11**. Utilizing **Table 2.1**, the gases become uncoupled, leaving only the corresponding concentrations of each. These concentrations are refined by simultaneous measurements of methane and water vapor.

Mass Results

The MS-TDLAS results can be compared, summed, and normalized to approximate the individual component contribution percentages of mass loss from the sample across the entirety of the pyrolysis. This process is shown in Eqs. (47 – 49).

$$\rho_i = \frac{1}{N_A} M_i \int n_i dT \tag{47}$$

$$\rho = \sum_i \rho_i \tag{48}$$

$$\eta_i = \frac{\rho_i}{\rho} \tag{49}$$

Where M is the molecular weight in $[\mathrm{mg/mol}]$, n the molecular concentration of compound i in $[\mathrm{molecules/cm^3}]$, and η is the percent mass of compound i lost in the pyrolysis.

Results shown in **Figure 2.12** are specifically for the heating rate of $5\ [°\mathrm{C/min}]$, and demonstrate that the largest components of the outgassing from the carbon phenolic

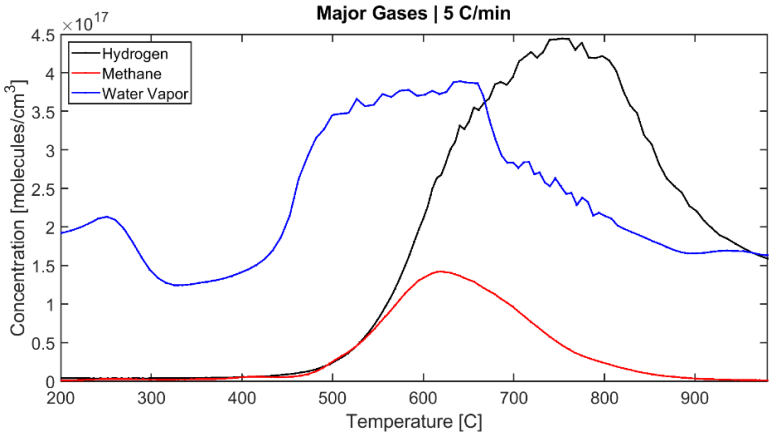


Figure 2.9. Recovered concentrations of the most prominent gases at $\dot{Q} = 5$ [°C/min].

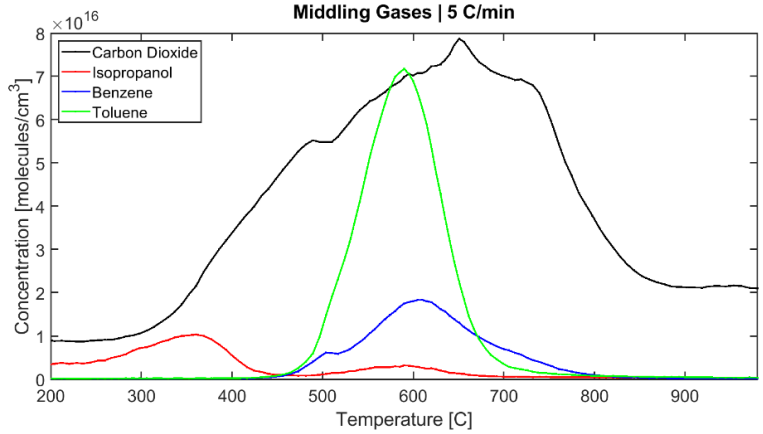


Figure 2.10. Recovered concentrations of gases with a middling presence at $\dot{Q} = 5$ [°C/min].

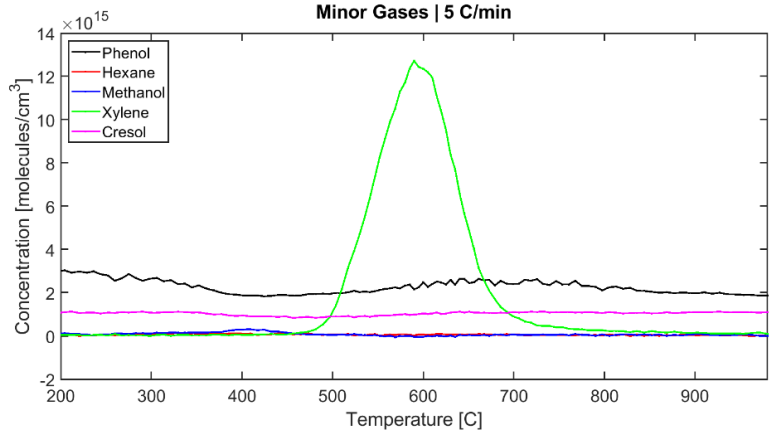


Figure 2.11. Recovered concentrations of gases with a minor presence at $\dot{Q} = 5$ [°C/min].

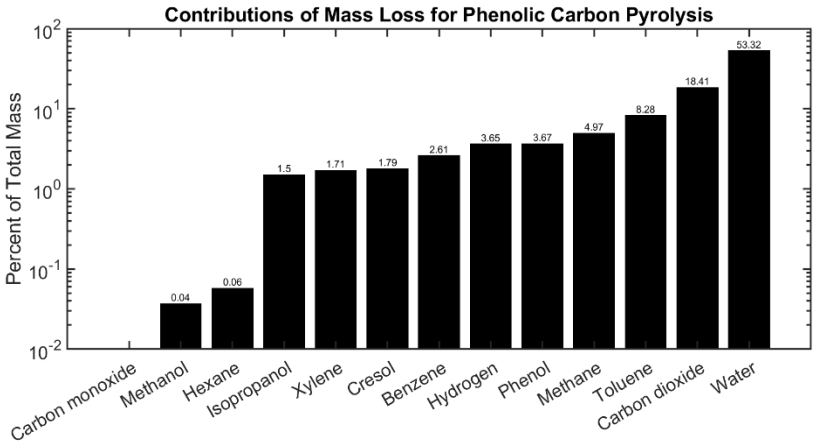


Figure 2.12. Breakdown of normalized mass loss contributions by compound with percentage values listed.

sample is water vapor, carbon dioxide, and toluene, with significant contributions from methane, phenol, and hydrogen.

Discussion of Failures

Within this experiment, there are several pitfalls to note such that any who attempt to recreate it may do so painlessly. The largest and most important is that the carrier gas within the system used must be helium. Theoretically, any inert gas may be used (any gas that will not interact with the created compounds) but using gases other than helium lead to less than desirable results. Shown in **Fig. 2.13** is a graph of the MS output for the AMU of 28.

The pressure in the system drops considerably (shown by the value of the nitrogen carrier-gas). A similar trend occurred with argon. Corresponding with the flows of nitrogen and argon as carrier gases, is a decrease in the measured methane as shown in **Fig. 2.14**.

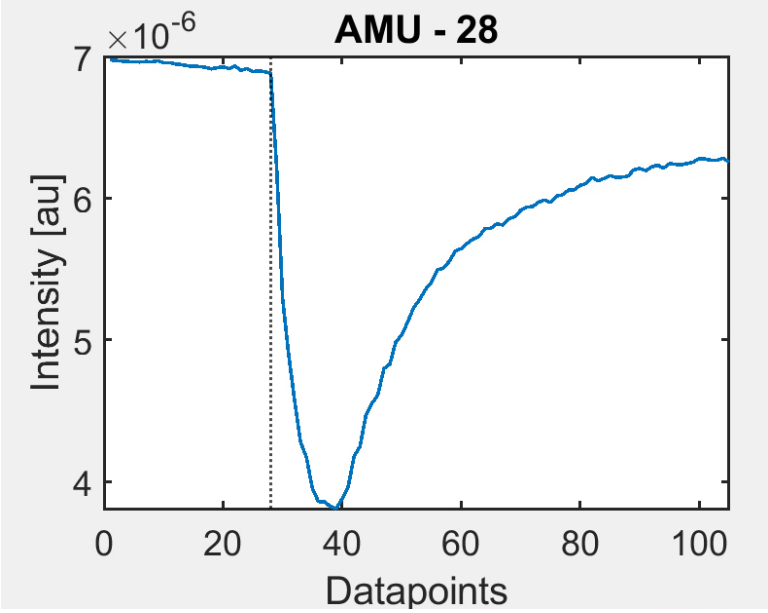


Figure 2.13. AMU of 28 as measured by the mass spectrometer. The dashed-line corresponds roughly to a furnace temperature of 500 [°C].

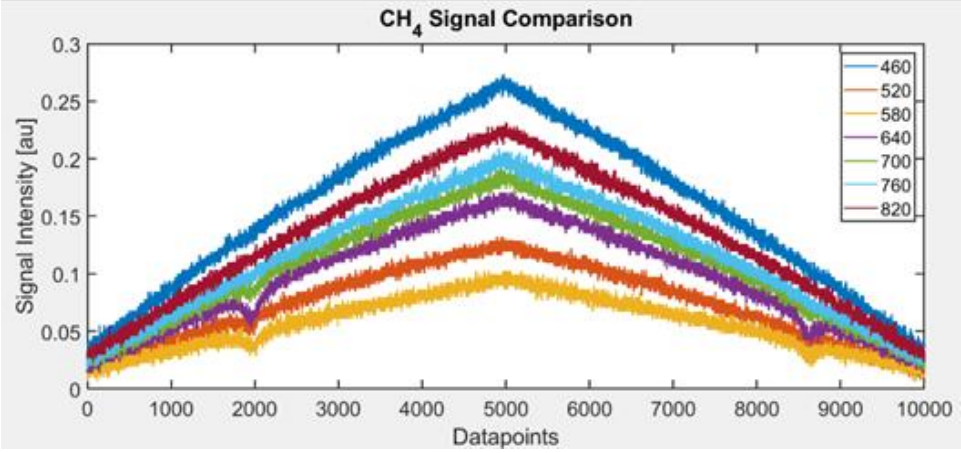


Figure 2.14. Value of methane intensity at varying temperatures. To note, prior to combustion, the signal is at its maximum. As the furnace continues heating up, the intensity drops significantly to a minimum around 580 [°C] before steadily rising back up by 820 [°C].

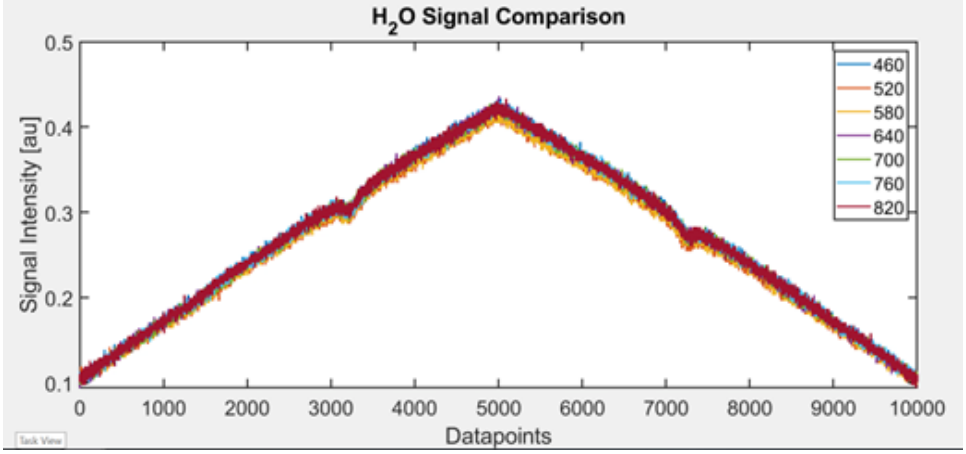


Figure 2.15. Water vapor signal intensity for a range of temperatures. To note, the signal intensity does not change dependent on the temperature.

Even normalizing the recovered signal and calculating the concentration as measured by the distortion, no realizable signal is recovered. At this point, it was assumed that there was some form of dust or particulate blocking the laser signal, so water vapor was also mapped for the same ranges as shown in **Fig. 2.15**.

As seen in **Fig. 2.15**, the behavior of the carrier wave should be static. That the methane was decreasing whenever argon or nitrogen was utilized gave rise to the exclusion of those carrier gases. As the experiment was not built to measure the capabilities of different inert gases, it's unknown entirely the reason why this phenomenon occurred, but it is speculated it has to do with the relative heat capacities of each. Shown in **Table 2.2** are the varying specific heat capacities for a number of inert gases.

With this table in mind, it is presumed that the methane was prematurely combusting from the outgassing, reducing the overall signal intensity on the 1654 [nm] laser.

Table 2.2. Carrier gases and their specific heat capacities.

Compound	Heat Capacity [J/kg · K]
He	5191.625
N_2	1039.623
Ne	1030.228
Ar	521.902

Other points of failure include diminishing saturation signals and ensuring transmission of light. Of the three compounds being measured directly by LAS (water vapor, methane, and carbon monoxide), water vapor alone is extant in the atmosphere. If the 1392 [nm] laser were multiplexed with the 1654 [nm] methane laser, it would give both a functional pathlength of 450 [cm]. However, the water vapor would measure an extra $50 - 100$ [cm] outside the cell between the laser diode, mirrors, and photodiode as has been illustrated in **Fig. 2.3**. This extra absorbance pathlength for the water vapor will saturate the signal and give wildly incorrect results. Originally, an attempt was made to measure a background signal from the 1392 [nm] laser and simply denote any increases beyond that as from the pyrolysis, but with a pathlength of around half a meter, the system became sensitive enough to pick up on water vapor from people breathing around the experiment. Ultimately, it was decided to reduce the pathlength to the 5 [cm] clear across the cell.

A similar conclusion was reached for the carbon monoxide laser at 2327 [nm]. It is believed that some optic in the system is opaque at this wavelength resulting in a diminished signal for carbon monoxide when multiplexed across the Herriott cell system.

CHAPTER THREE

MEASUREMENTS OF NO ROTATIONAL AND VIBRATIONAL TEMPERATURES BEHIND A NORMAL SHOCK IN HYPERVELOCITY FLOW VIA ABSORPTION SPECTROSCOPY

Motivation

To characterize the temperature and concentration of nitric oxide behind a normal shock in high Mach flows. To track the evolution over time of these variables and minimize the errors on the measurements. To model how ablative and corrosive gases (nitric oxide) change behind a normal shock with an idea of how such creation and evolution would affect hypersonic craft.

Abstract

Tunable diode laser absorption spectroscopy (TDLAS) measurements of nitric oxide (NO) using a quantum cascade laser (QCL) in the vicinity of 5.26 [μm] were conducted in a hypervelocity flow generated in the Texas A&M hypervelocity expansion tunnel (HXT). The nascent NO was produced downstream of symmetric Mach reflections generated in Mach 8.5 flows with stagnation enthalpies from 6.9 to 11.1 [MJ/kg]. Path-averaged flow parameters of rotational and vibrational temperatures and NO concentration at a measurement rate of 30 [kHz] were obtained. By probing the R-branch of the fundamental absorption band in NO, thermal nonequilibrium and NO concentration levels in the post-shock region were measured. Measurements are compared to equilibrium calculations. NO equilibrium values during the 1 [ms] test period differ from the experimental rotational and vibrational measurements across the same time period. The experimental measurements of the rotational temperature show a consistent value around 3000 [K] larger than the recovered vibrational temperature across any run. The NO concentrations in all runs are near the reported equilibrium value; often beginning

higher than, and over time decaying to, the equilibrium concentration value of the specific tunnel run.

Introduction

Strong shockwaves are ubiquitous in hypersonic flight conditions and the increase in gas temperature through such strong compressions can result in the generation of nitric oxide (NO), the activation of vibrational energy modes of molecules, and possibly dissociation chemistry depending on the flow conditions. The molecular dissociation and redistribution of energy among the available vibrational energy modes leads to changes in the physical and transport properties of the gas that have a significant impact on the calculation of important engineering quantities such as the amount of surface heat transfer [32,33]. As ground testing facilities are key to development of hypersonic flight systems, it is important to quantify these high-temperature gas effects during testing. TDLAS can be modeled to account for nonequilibrium temperatures through the use of a two-temperature model approximation assuming independent rotational and vibrational temperatures and states. This is important, as a common approach to modeling nonequilibrium flows in CFD is to use a multi-temperature approach where each internal energy mode (translational, rotational, vibrational, and electronic) is given a corresponding temperature. Using a two-temperature model, it is assumed that translational and rotational temperatures are identical due to similar relaxation rates, the vibrational differs due to its relatively long relaxation time, and that the electronic is negligible so long as the absorbing medium remains in the ground state. Such models and their applications in CFD are discussed elsewhere in literature [32–36].

Thermal nonequilibrium flows stem from the varying relaxation timescales of the rotational and vibrational energy modes [8]. To wit, high energy environments may maintain, for brief periods of time, several different temperatures based on the mode of excitation. NO is a good measure of these varying excitation modes as it readily forms in hypersonic environments and contains ample variation in its absorption peaks allowing for mode differentiation [37]. The use of TDLAS in hypersonic flows has been rigorously tested and shown in various experiments and literature to be a reliable measurement technique to describe such flows [37–43]. By using TDLAS within the fundamental band R-branch of NO, the rotational and vibrational temperatures may be recovered.

In this work, nascent NO formed behind a normal shock in a Mach 8.5 flow is analyzed via TDLAS to recover the rotational and vibrational temperatures. A two-temperature model is used to understand the effect on nonequilibrium flow behind the shockwave. Similar assumptions were also made in work by Girard et al. [37]. Furthermore, all excited states are presumed to be in the $X^2\Pi$ ground state of NO, allowing for the approximation of a constant electronic partition function, removing the need to consider the electronic temperature [8]. This work is primarily focused on establishing a baseline analysis for TDLAS in the Texas A&M hypervelocity expansion tunnel (HXT), with future interest focusing on measuring thermochemical nonequilibrium in the shear flow

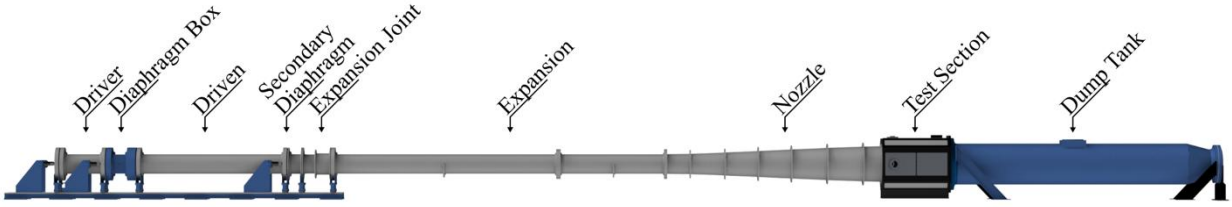


Figure 3.1. The components of the Texas A&M HXT facility [44].

region of a Mach stem interaction.

Setup

Facility and Test Conditions

Experiments were performed in the HXT which is described in detail by Dean et al. [44] and depicted in **Figure 3.1**. The 30.5 [m] long facility features a 0.48 [m] diameter pipe in the driver, driven, and expansion sections and a nozzle with a 0.92 [m] exit diameter is used to further expand the flow to achieve increased Mach number range, test time, and test core size. Typical facility run times are on the order of 1 [ms] but vary based on the target flow conditions. Testing conditions for this work are shown in **Table 3.1**. In each test helium was used for the driver gas while air was used in the driven section.

Model Geometry

The model geometry used in this work is described by Dean et al. [45] and shown in **Figure 3.2**. Measurements were carried out at approximately 30 [mm] behind the resulting normal shock region. The model is easily moved streamwise, which allows the TDLAS setup to remain in a fixed position during condition changes. An advantage of this geometry is its ability to generate a normal shock without a test object in the post-shock region. Similar axisymmetric concepts have been used by others [46], but the two-dimensional design of the model allows for better compatibility with optical diagnostics. The normal shock is well illustrated in **Figure 3.2**.

The origin of the system is defined in **Figure 3.2a** as the top of the bottom wedge. As stated previously, measurements were collected in the post-normal shock region.

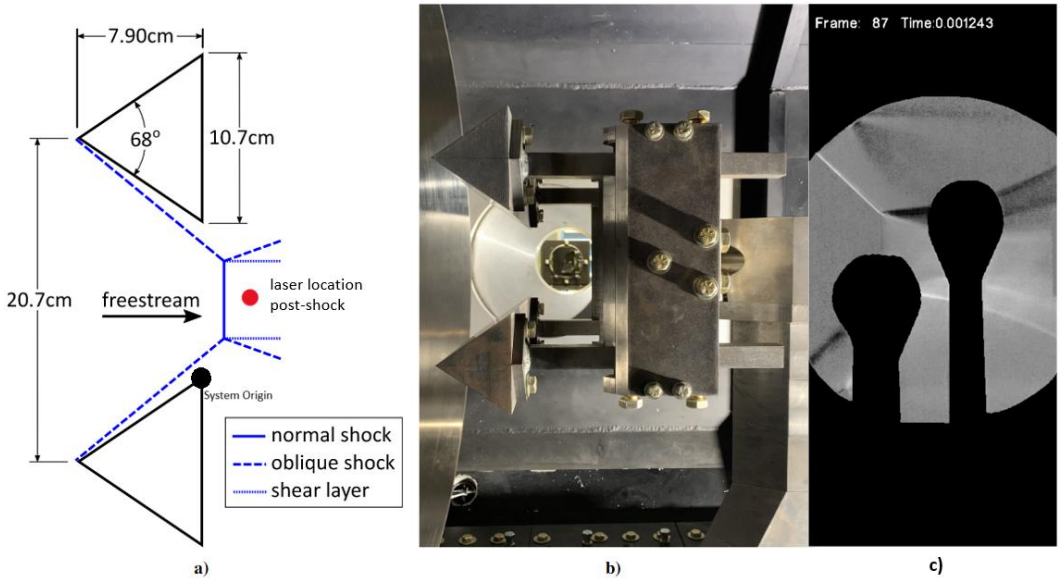


Figure 3.2. (a) Dimensioned drawing of the Mach stem generator with representative flow structures and laser location, (b) a photograph as installed in the HXT test-section (viewed from the side), and (c) Schlieren image visualizing Mach stems in steady state from run 221 (with mirrors for NO and atomic oxygen silhouetted).

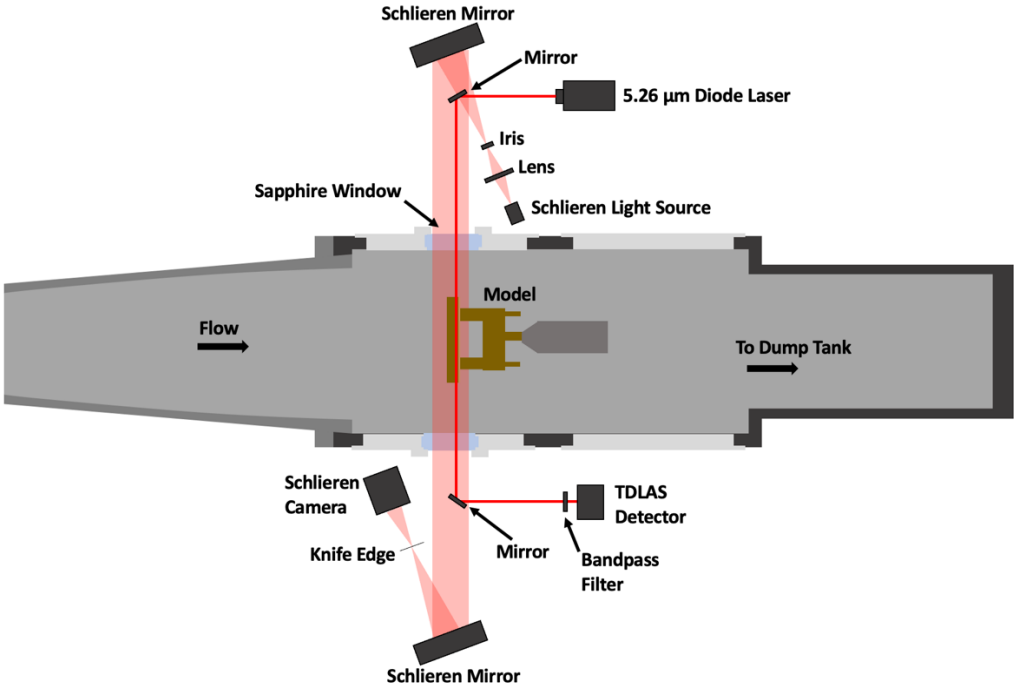


Figure 3.3. A diagram showing the beam path of the diode laser beam with respect to the tunnel and model as well as the concurrent schlieren setup.

Table 3.1. Initial gas pressures and resulting flow conditions in the HXT for the TDLAS measurements.

HXT Run Number	Driver Pressure [MPa]	Driven Pressure [kPa]	Expansion Pressure [Pa]	Mach #	h_0 [MJ/kg]	T_∞ [K]	ρ_∞ [kg/m^3]	U_∞ [m/s]
219	9.65	7.24	28.93	8.6	6.9	440	0.0091	3616
220	9.31	0.59	2.67	8.5	11.1	700	0.00083	4508
221	8.34	1.93	8.80	8.5	8.8	570	0.0027	4068
222	8.34	1.93	8.80	8.5	8.8	570	0.0027	4068

Table 3.2. Equilibrium conditions for the post-normal shock region.

HXT Run Number	E.Q. T_2 [K]	E.Q. P_2 [kPa]	E.Q. ρ_2 [kg/m^3]	E.Q. NO Mole Fraction	E.Q. NO Mass Fraction
219	3780	107.94	0.0888	0.049	0.057
220	4931	15.42	0.0087	0.008	0.010
221	4285	40.85	0.0282	0.023	0.028
222	4285	40.85	0.0282	0.023	0.028

Equilibrium conditions for this region are shown in **Table 3.2**. These calculations were performed for a seven-species model using the JANAF thermochemical database [47].

Experiment

A schematic showing the beam path of the diode laser beam is shown in **Figure 3.3**. The diode laser (*LD-PD DFB-QCL*) emission is centered around 5.26 [μm] with a nominal tuning capability of 30 [nm] depending on modulation parameters. The spectral width of the laser is below 1 [MHz]. The 5.26 [μm] beam was guided into the tunnel using a silver mirror and then turned onto a detector using another silver mirror. A bandpass filter (*Thorlabs FB5250-500*) was placed in front of the detector to reduce any potential contributions from other light sources. The laser current was modulated at 30 [kHz] to perform the necessary wavelength sweeping on a timescale comparable to the facility run

time. The 30 [kHz] modulation and nominal facility run time of 1 [ms] provides around 30 cycles during the steady state.

Ro-Vibrational Model

As transmission has been modeled for both vibrational and rotational temperatures (see Chapter One), they may each be fit to unique values through iteration. Both the transmitted signal and baseline data are taken from an oscilloscope sampled at 200 [MHz] and analyzed in MATLAB using Eq. (1).The two signals are shown in **Figure 3.4** with the vibrational and rotational bands shown in **Figure 3.5**. The data are broken into up-cycles and down-cycles depending on whether they occur on the rise or the fall of the carrying sinewave. The periodic cycles were minimally averaged so as to better preserve the shape of each spectrum in time.

In **Table 3.3**, the subscript 1 in the Rotational Transitions column is for the value $\Omega = 1/2$; likewise, 2 for $\Omega = 3/2$. Each signal is analyzed independently through an iterative

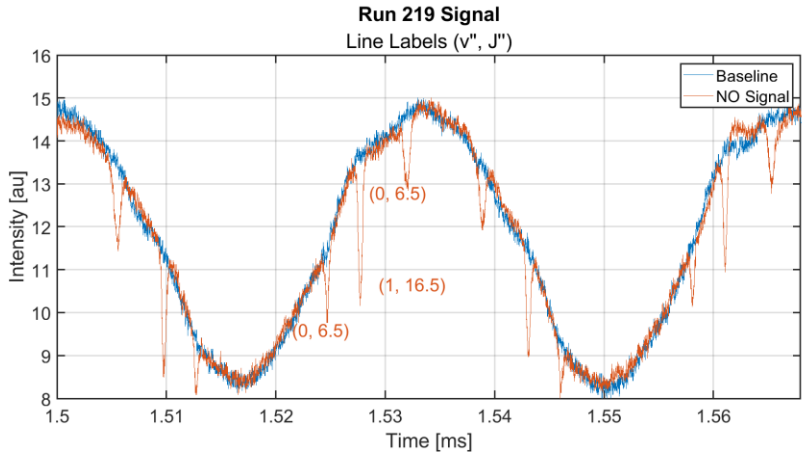


Figure 3.4. Baseline signal and transmitted NO signal from Run 219.

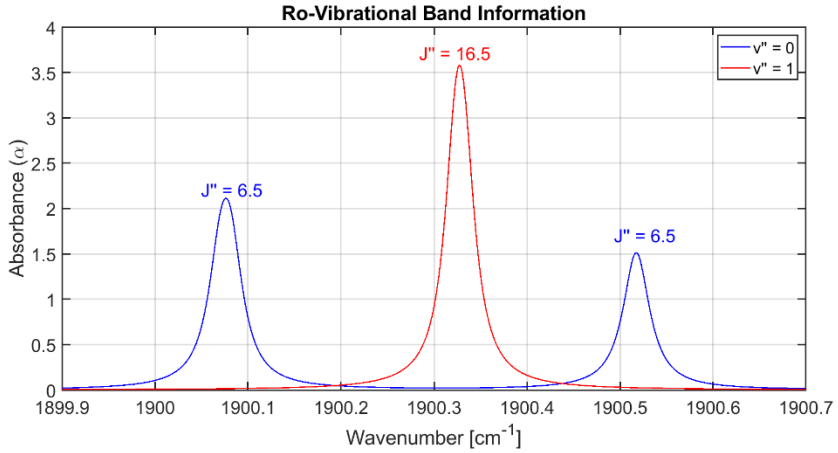


Figure 3.5. Measurable bands by the QCL.

Table 3.3. Transitional band information for the three main NO peaks.

Vibrational Level $(v'' - v')$	Rotational Transitions	Extant Range $[\mathbf{cm^{-1}}]$
$0 \rightarrow 1$	$R_1(6.5), R_2(6.5)$	$1900.071 - 1900.518$
$1 \rightarrow 2$	$R_1(16.5)$	$1900.324 - 1900.339$

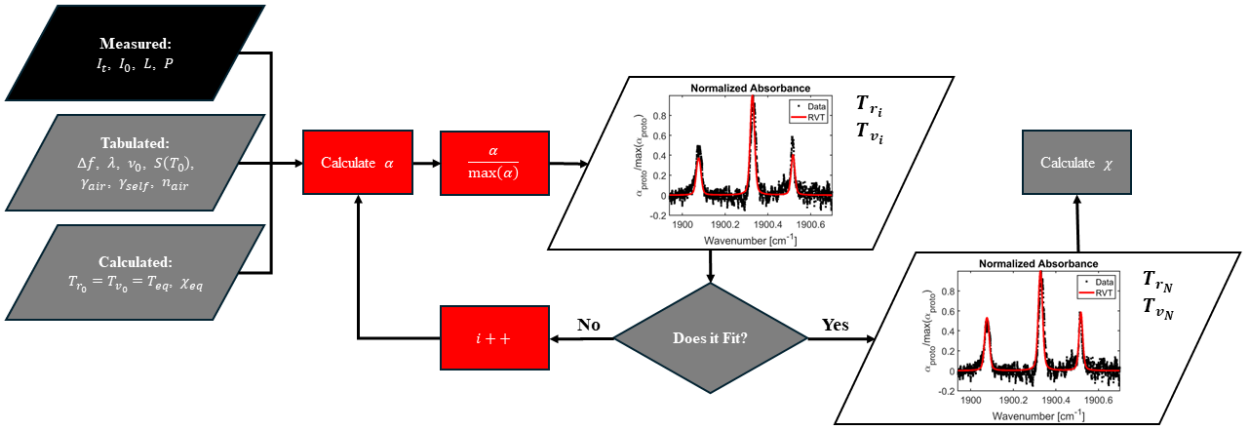


Figure 3.6. Flowchart showing the operations for data processing.

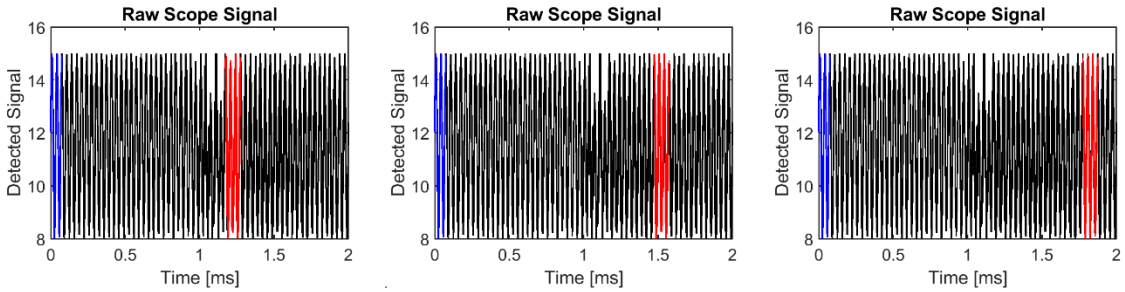


Figure 3.7. The baseline spectrum is in blue and the transmitted spectrum is in red. Shown are progressive (nonconsecutive) selections of the transmitted spectra.

process with starting conditions equal to that of the equilibrium values shown in **Table 3.2**. Upon convergence of an answer, results are plotted to confirm convergence.

Data Processing

To process the data, an iterative function is employed to return the best results with minimal input as laid out in **Figure 3.6**. To begin, the baseline spectrum is divided from the transmitted spectrum to recover the transmission in accordance with Eq. (1). The baseline spectrum is taken from the early measurements of the tunnel's steady state as shown in **Figure 3.7**. The baseline remains constant while the transmitted spectra shift along the time-axis.

Scans are split into up-cycles and down-cycles, then analyzed under an equilibrium assumption to obtain initial spectral shapes. These shapes are then normalized and used as an initial guess prior to being passed through to the fitting function. The fitting function used is a simple scan across a large range of rotational and vibrational temperatures to find a range where the residual error is within a set tolerance. When a range of minimum error is found, the sweep repeats with a smaller range centered on the prior range of minimum error.

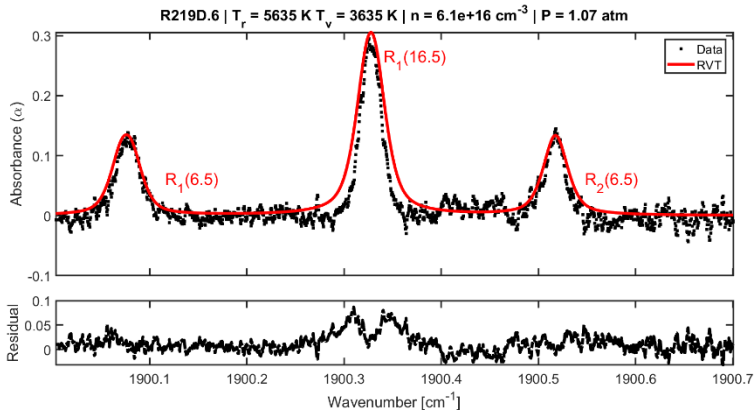


Figure 3.8. Run 219, 6th down-cycle measurement.

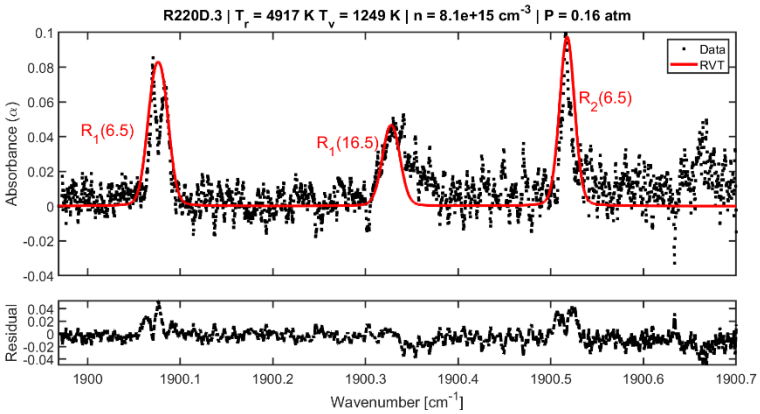


Figure 3.9. Run 220, 5th down-cycle measurement.

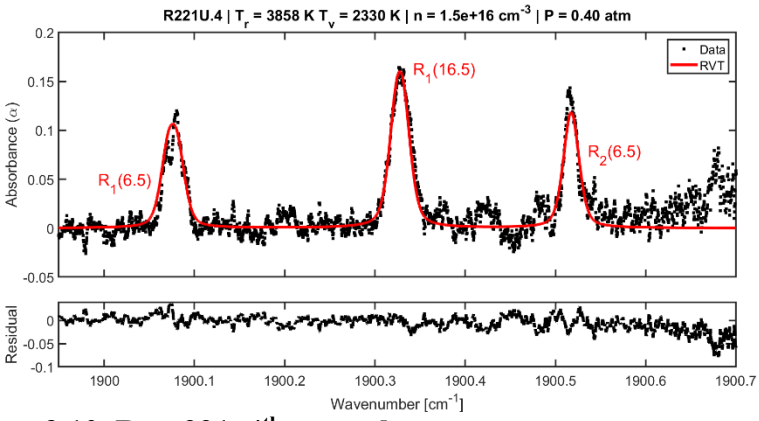


Figure 3.10. Run 221, 4th up-cycle measurement.

Beginning with initial temperature guesses taken from the final equilibrium temperature of the system, a range of 5000 [K] centered on the equilibrium temperature is swept across for both rotational and vibrational temperatures. When a new range of minimum error is found, the center is set as the new starting point and a new sweep of just 1250 [K] occurs. This process repeats with each sweep comprising a smaller range of degree changes than the prior until error is below the tolerance, the temperature change would be less than 1 [K], or when the temperature change oscillates between two values.

Results

Four tests in the HXT were evaluated, with most fits yielding low residual errors. This is shown in **Figures 3.8 – 3.10** with recovered spectra shown for illustration. Depicted in black are the experimental data and in red are the RVT model fits using the equations described in Chapter One. Beneath each figure are the residuals for the individual spectrum; outlier data have been disregarded. As the steady state decays toward the later periodic cycles, the signal to noise ratio diminishes greatly as shown in **Figure 3.11**. As such, the data just prior to the end of steady state have been discarded.

As the noise level reached the measured height value of the peaks, it became difficult to accurately model the temperature and the concentration of NO present in the system. This is reflected in **Figure 3.18** where the NO concentration tapers off toward the end of the steady state conditions.

As a fidelity check for the convergence of the temperature values, a ratio is created from the integrated absorbances of the peaks as discussed in Chapter One. This ratio follows

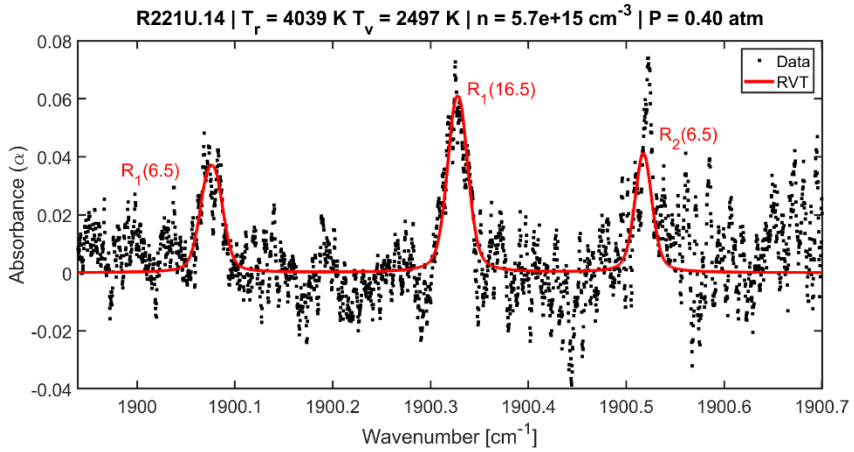


Figure 3.11. Best fit for noisy, low-concentration NO data in run 221, 14th up-cycle measurement shown here as an illustration of data that were discarded.

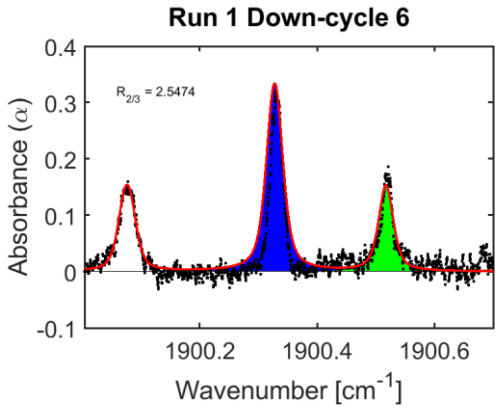


Figure 3.12. Highlighted peaks for integration resulting in a ratio purely as a function of temperature.

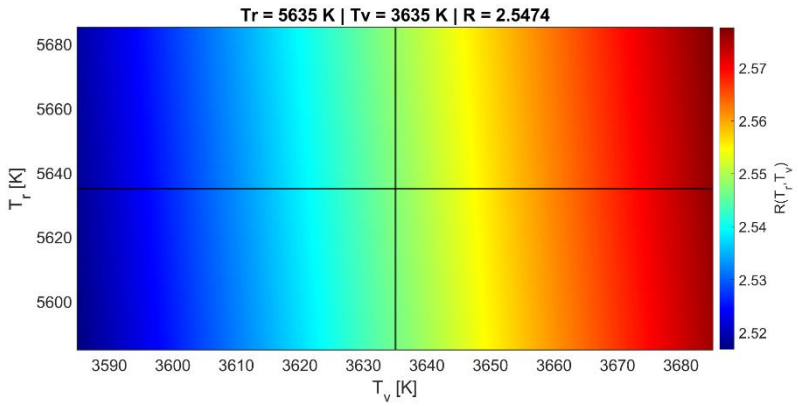


Figure 3.13. $R(T_r, T_v)$ as shown in Eq. (50) and the recovered T_r and T_v values.

the form of Eq. (50), a variant of the form presented in Eq. (37), and depends solely on the rotational and vibrational temperatures.

$$R(T_r, T_v) = \frac{A_1}{A_2} = \frac{S_1(T_r, T_v)}{S_2(T_r, T_v)} = f(T_r, T_v) \tag{50}$$

By comparing this ratio to a theoretical ideal, the temperature may be recovered for both the vibrational and the rotational values. This is shown in **Figures 3.12 – 3.13** by taking a ratio of the 2nd (middle) peak over the 3rd (right) peak.

For every temperature combination there is a unique value of R allowing for a recovery of the rotational and vibrational temperatures. The recovered temperatures match the values obtained through spectral fitting. **Figures 3.14 – 3.16** show the recovered rotational and vibrational temperatures against time from the data, the trendlines of either, the calculated equilibrium temperature taken from **Table 3.2**, and the frozen temperatures for three of the four runs. The uncertainty bounds are found using Eqs. (51 – 53).

$$d\tau = \text{maximum}\left[\left|\frac{\tau_{\text{sim}} - \tau_{\text{exp}}}{\tau_{\text{exp}}}\right|\right] \tag{51}$$

$$d\tau = \frac{\partial \tau}{\partial T_r} dT_{r_0} + \frac{\partial \tau}{\partial T_v} dT_{v_0} + \frac{\partial \tau}{\partial S} dS + \frac{\partial \tau}{\partial \gamma_{\text{air}}} d\gamma_{\text{air}} + \frac{\partial \tau}{\partial \gamma_{\text{self}}} d\gamma_{\text{self}} + \frac{\partial \tau}{\partial n_{\text{air}}} dn_{\text{air}} \tag{52}$$

$$dT_r = dT_{r_0} + \xi; dT_v = dT_{v_0} + \xi \tag{53}$$

Where τ_{sim} is the transmission of the simulated model, τ_{exp} is the transmission of the experimental data, and ξ is the average noise level of the spectrum ratioed over the spectral maximum. As the laser is path-integrated, it must pass through the boundaries of the extant shock-structures in the system. Noise ξ helps quantify these structures, with lower values indicating minimal interference with the overall measurement.

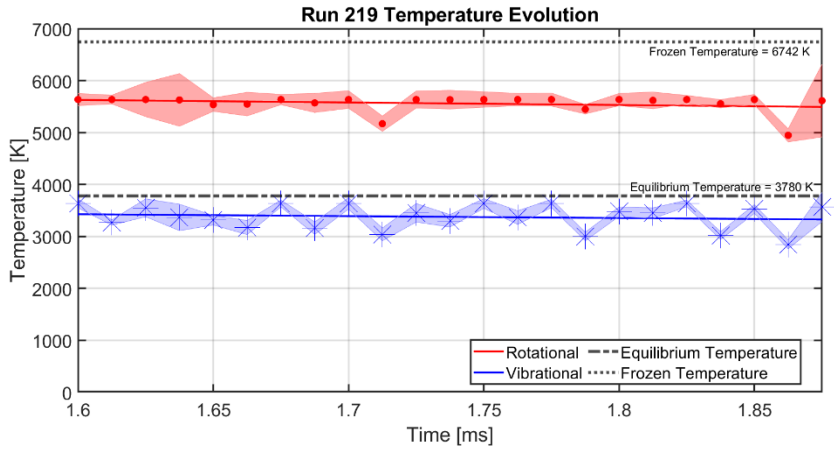


Figure 3.14. Temperature evolution across run 219.

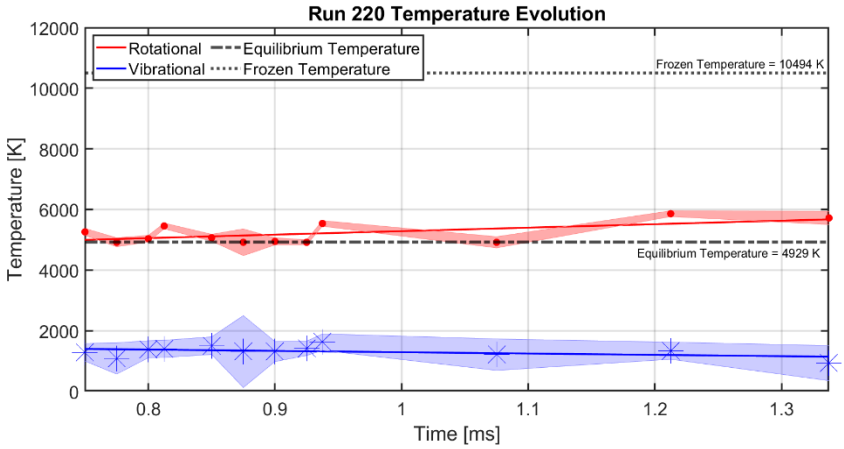


Figure 3.15. Temperature evolution across run 220.

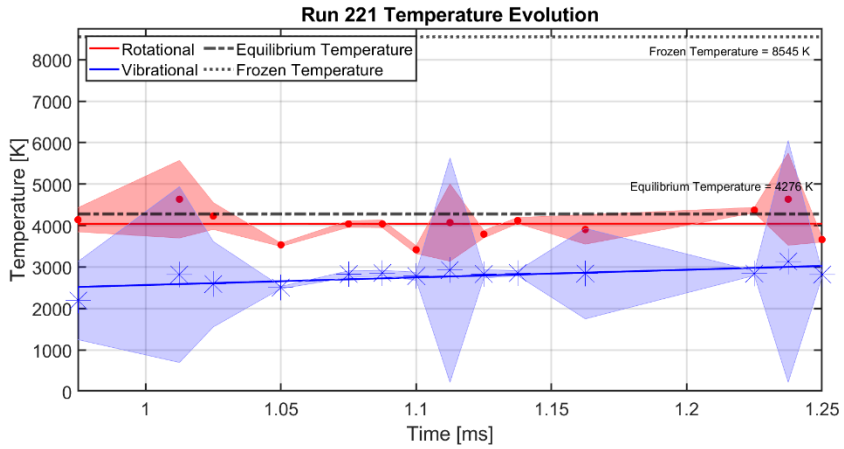


Figure 3.16. Temperature evolution across run 221.

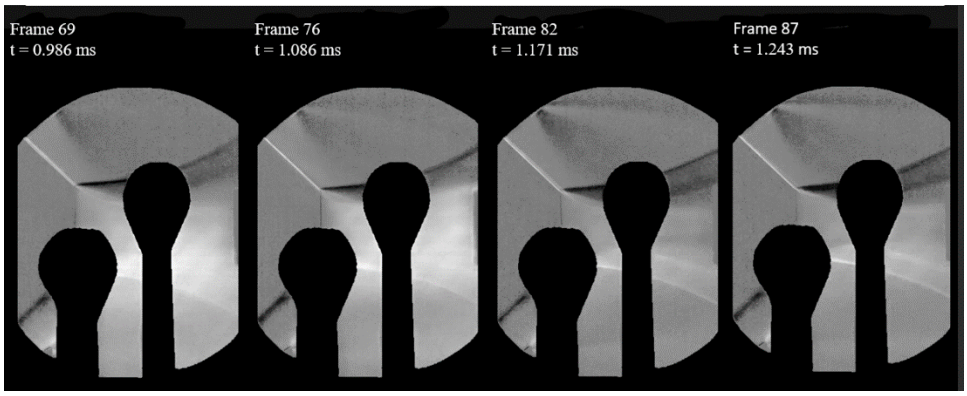


Figure 3.17. Schlieren images throughout steady state of run 221 from 0.986 to 1.243 [ms] with beam-posts for NO and atomic oxygen detection silhouetted.

To recover the maximum uncertainties for the rotational temperatures, $d\tau$ is calculated from Eq. (51) and dT_{v_0} is set to zero; the value of dT_{r_0} is then calculated from Eq. (52). Uncertainties for HITRAN values are tabulated in the HITRAN database. The calculated value is summed with the uncertainty from the SNR ξ to recover the final uncertainty of the rotational temperature dT_r. A similar process is performed for dT_v. Transmission is considered in place of absorbance to remove any division by zero. The error bounds on either side of the datapoints then are the resultant answers for dT_r and dT_v which result in the definition of $d\tau$ in Eq. (51). Any datapoints with an error bound beyond the frozen temperature or below 0 [K] have been discarded.

With all three analyzed runs, the rotational and vibrational temperature are plotted with an associated trendline. This trendline remains constant for the duration of steady state, indicating that the NO remains in thermal nonequilibrium for this time. Throughout any given run there would be occasional disturbances or fluctuations in the post-shock region as illustrated by the opaqueness of the flow in frames 69 and 76 of **Figure 3.17**.

Table 3.4. Recovered frozen temperatures for each analyzed run.

Run	Mach	Freestream Temperature [K]	Frozen Temperature [K]
219	8.6	440	6742
220	8.5	700	10494
221	8.5	570	8545

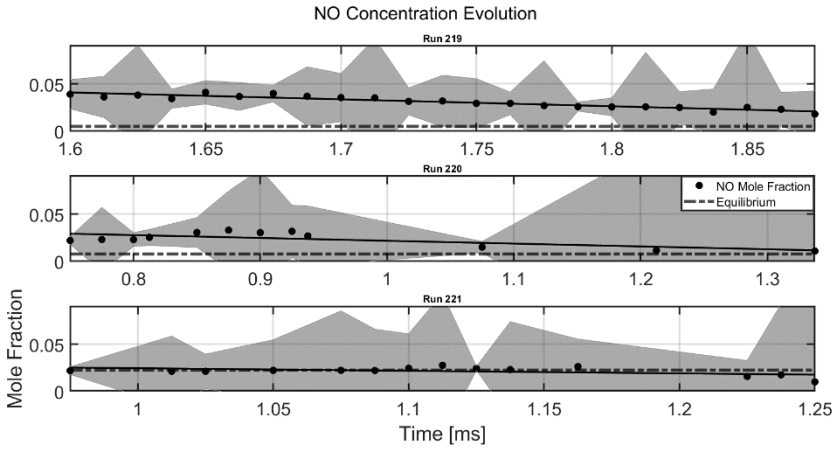


Figure 3.18. Concentration changes for NO across steady state for three of the runs of the HXT.

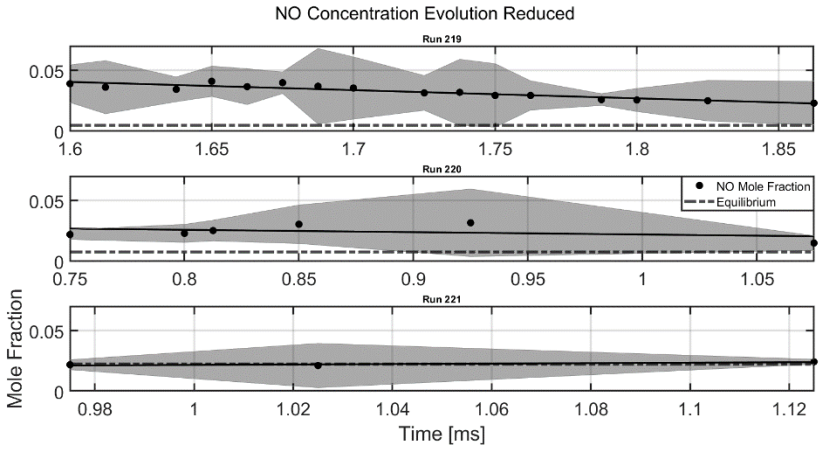


Figure 3.19. Reduced NO concentration.

These fluctuations in the optical density of the flow cause oscillations in the recovered temperature and concentrations shown in **Figures 3.14 – 3.16** and **3.18**.

The temperature assuming ideal post-shock conditions (called the frozen temperature) has been calculated for all runs using Eq. (54) to compare with the experimentally recovered values.

$$T_{\text{frozen}} = \frac{(2\gamma M_a^2 - \gamma + 1)\big((\gamma - 1)M_a^2 + 2\big)}{(\gamma + 1)^2 M_a^2} T_\infty \tag{54}$$

This is an upper-limit for real temperature values. For runs 220 and 221, the frozen temperature far exceeds the highest measured rotational temperatures. However, in run 219, the frozen temperature is only a few hundred degrees higher than the maximum rotational temperature. This analysis is shown in **Table 3.4**. In Eq. (54), γ is approximated to 1.4. The freestream temperature T_∞ and Mach number M_a both come from **Table 3.1**. The approximation of γ is to give an absolute maximum temperature ceiling as the actual γ will have a lower value than this, though not by a significant margin. As shown in **Figure 3.18** the concentration evolution across steady state follows similar trends, with the NO concentration diminishing during the test time.

The concentration of NO is recovered by solving for n and χ in Eqs. (1) and (14) using the conversion in Eq. (15) to reduce the number of variables. Pressure is assumed known from the tests as the equilibrium pressure calculated in **Table 3.2** and temperature is assumed rotational. The error bounds in **Figure 3.18** are the simple maximum of the absolute value of the percent error recovered from the comparison of the theoretical fits of the transmission to the experimental results in Eq. (51) summed with the noise

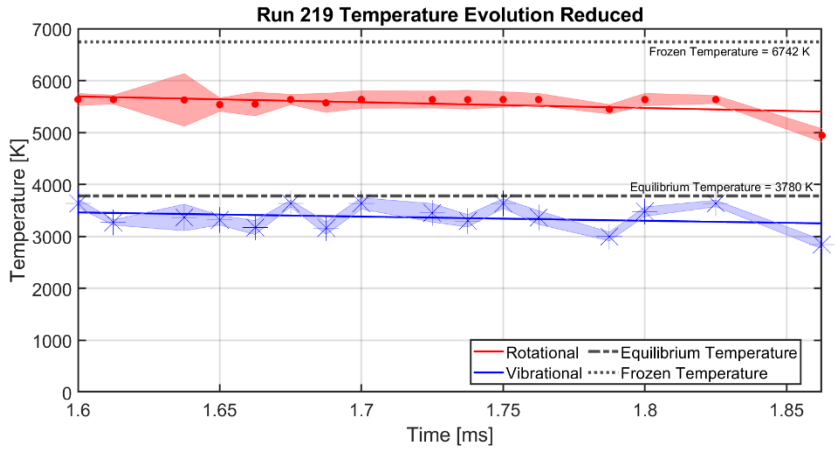


Figure 3.20. Reduced run 219 rotational and vibrational temperatures.

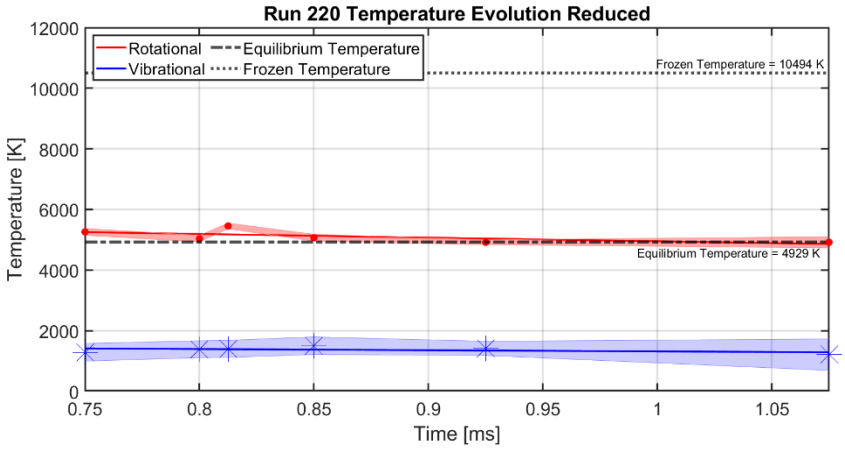


Figure 3.21. Reduced run 220 rotational and vibrational temperatures.

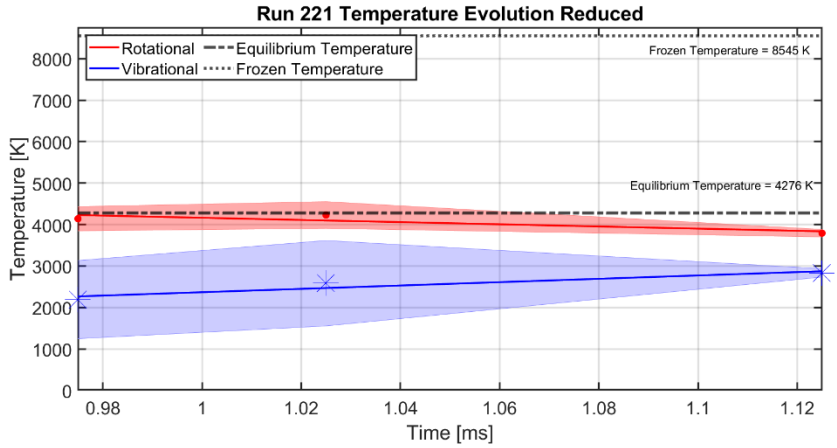


Figure 3.22. Reduced run 221 rotational and vibrational temperatures.

uncertainty ξ. If only the datapoints where the bounds of uncertainty remain strictly positive are considered, then **Figure 3.19** is recovered.

The removal of concentration datapoints with error bounds that are strictly positive may be applied to the temperatures recovered in **Figures 3.14 – 3.16** to further reduce possible erroneous datapoints. Performing this analysis results in **Figures 3.20 – 3.22** where "reduced" indicates that the poor fit concentration datapoints have been removed.

To note, for the later runs, the low concentration data had too high a noise level to be plotted in the reduced scale. Even with the reduced scale, there are still violent temperature swings in the uncertainty as highlighted in **Figure 3.20** where the uncertainty for at least one point exceeds 1000 [K]. This isn't to say that the temperature is unstable at this point, rather the quality of the spectrum at that point in time leaves a large margin of error to consider. The high uncertainty bounds on the figure are there to reflect that.

To discuss whether these results hold up to scrutiny, the approximate equilibrium distances have been estimated using **Table 3.5** and Eqs. (55 – 57), Landau-Teller approximations, to estimate how far into the flow nonequilibrium should follow and hold.

$$P_2 = \left[\frac{2\gamma M_a^2 - \gamma + 1}{\gamma + 1}\right] P_1 \tag{55}$$

$$t = \frac{2}{P_2}\left(C_1 \exp\left[\left(\frac{C_2}{T_{\text{frozen}}}\right)^{\frac{1}{3}}\right]\right) \tag{56}$$

$$x_{\text{equilibrium}} \approx t M_a \sqrt{\gamma R T_{\text{frozen}}} \tag{57}$$

Where P_1 is the freestream static pressure in [Pa] estimated from the driver, driven, and expansion pressures listed in **Table 3.5** along with the NO values for C_1 and C_2. The

Table 3.5. Approximate equilibrium distances for the HXT runs.

Run	Mach	P_1 [Pa]	$x_{\text{equilibrium}} + 20$ [mm]
219	8.6	1149.148	22.289
220	8.5	166.747	29.005
221	8.5	441.693	24.395

Values of C_1 and C_2 for NO are 4.86×10^{-3} [atm/μs] and 1.37×10^{6} [K] respectively.

pressure measurements are taken in the manner shown by Dean [44]. From previous wind tunnel campaigns, the predicted static pressures are shown to be only 5% off measured pressures. These values then give the approximate distances the thermal nonequilibrium will bleed into the flow. The addition of the 20 [mm] in the total distance is to reflect that the shock forms ~20 [mm] [48] from the back of the bottom wedge shown in **Figure 3.2**. The NO laser was aimed directly through the tunnel at an offset distance of 29 [mm] from the back of the bottom wedge, so the laser was well around the distances to measure thermal nonequilibrium for the three analyzed runs.

It is shown that the rotational and vibrational temperatures while under steady state conditions for the HXT do not converge or decay quickly and are slightly stable around the starting conditions. Likewise, the concentration of NO in the system for the duration of steady state is consistent until the degradation of steady state begins. In total, most of the test conditions show thermal nonequilibrium between the vibrational and rotational energy states for NO behind the normal shock.

Discussion of Failures

As with Chapter Two, this experiment encountered many setbacks. The first and most prominent was the modeling of the RVT simulation. Shown in Eqs. (16 – 28) in Chapter

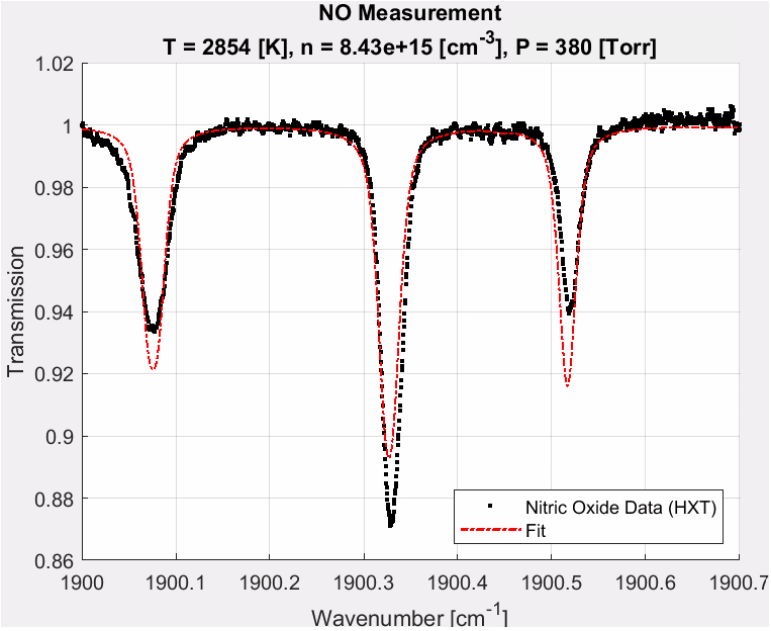


Figure 3.23. Equilibrium temperature fit for some HXT data.

One are the equations of the final RVT model, but these do not go through the derivations and the several attempts of modeling before the solution was discovered. An initial estimate assuming an equilibrium temperature is shown in **Fig. 3.23**.

The red line is the best fit after several dozen iterations. This is the largest indication that an equilibrium temperature assumption will not work for what is measured. It is on this basis that much work has gone into the uncertainty analysis to verify the data.

When creating the RVT model, it became necessary to split all temperature components up into rotational and vibrational—a two-temperature model. The electronic temperature is not considered as all measured NO is in the ground-state. Shown in **Fig. 3.24** is the rationale for assuming only rotational and vibrational (T_r & T_v) in the model.

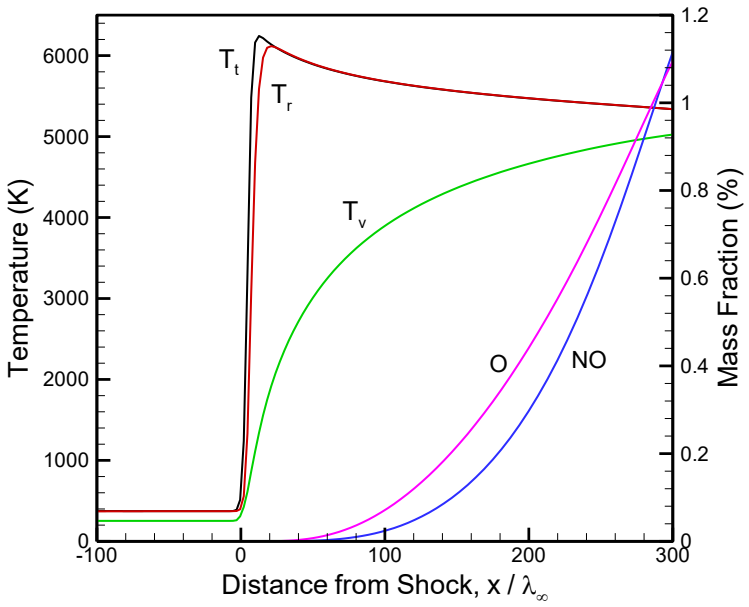


Figure 3.24. Temperature separation behind a normal shock for translational (T_t), rotational (T_r), and vibrational (T_v).

Clearly seen, the rotational and translational temperatures maintain similarity beyond the shock and certainly in the region the laser was probing. The remaining issue with the modeling after this assumption was to decide which temperatures contribute to what in the model. Shown clearly in Eq. (16), the rotational and vibrational energies are reduced by their respective temperatures. What is less clear (and what caused several issues in the early stages of modeling) are the temperatures within the Voigt broadening approximations. Specifically, in Eqs. (10, 14), the temperature variable is replaced with the rotational/translational temperature to best replicate real-world physics.

CHAPTER FOUR

MACH 6.5 ARCJET TUNNEL VELOCITY MEASUREMENT BY WAVELENGTH MODULATED SPECTROSCOPY

Motivation

To characterize the velocity evolution of a Mach 6.5 arcjet tunnel over the course of the test. To measure the change in compound concentration while the test runs. To learn how best to utilize WMS for an LAS system.

Abstract

This study employs wavelength modulated spectroscopy (WMS) single-laser line velocimetry to characterize the velocity and gaseous properties within a Mach 6.5 arcjet tunnel at the University of Tennessee, Knoxville. WMS operates by modulating the wavelength of laser light around the central absorption features of the targeted molecules. In this setup, the absorption of carbon monoxide at $4300\ [\mathrm{cm}^{-1}]$ is chosen for the measurements in the arcjet flow seeded with the gas. The laser is tuned to the absorption features, and the Doppler shift of these lines caused by the high-speed flow is analyzed to determine the flow velocity. By comparing the shifted absorption lines with stationary reference lines, precise velocity measurements are obtained. The depth and shape of the absorption lines further provide measurements of concentration. This research contributes to the field of aerospace engineering by offering a robust method for non-intrusive, high-precision measurements of gas properties and velocities in a hypersonic flow environment.

Introduction

Characterizing the properties of gases and measuring flow velocities in high-speed wind tunnels is a critical aspect of aerodynamic research and the development of aerospace technologies. High-speed flows, especially those reaching Mach numbers in excess of 5,

present significant challenges due to their complex, turbulent nature and extreme conditions. Traditional measurement techniques often face limitations in accuracy, spatial resolution, and intrusiveness, leading researchers to explore advanced diagnostic methods that can provide detailed, real-time data without disturbing the flow.

Laser absorption spectroscopy (LAS), especially WMS-assisted LAS, has emerged as a powerful tool for non-intrusive gas diagnostics. When applied to LAS, this technique can enhance signal detection sensitivity by modulating the laser wavelength around a central absorption line of the target gas. This modulation allows for the extraction of small absorption signals from noisy backgrounds, making it possible to obtain accurate and calibration-free measurements even in challenging environments.

In this study, WMS is applied to a single-laser line velocimetry measurement to characterize the velocity and gaseous properties within a Mach 6.5 arcjet tunnel at the University of Tennessee, Knoxville. The method utilizes a diode laser tuned to a specific absorption spectrum of a target gas: carbon monoxide (CO) at $4300\ [\mathrm{cm}^{-1}]$.

This work demonstrates the application of WMS single-laser line velocimetry in a Mach 6.5 arcjet tunnel to deliver high-precision, non-intrusive measurements of gas properties and flow velocities, offering valuable data for the validation and improvement of computational models and the development of advanced aerospace technologies.

Setup

A single laser beam, modulated with an AWG, is sent to a beam-splitter. Half is directed to a reference cell filled with stagnant gas while the rest is sent across the width of the

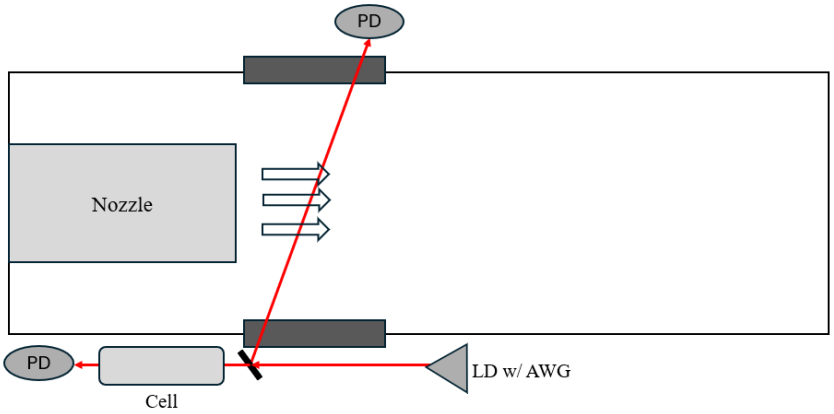


Figure 4.1. Experimental setup of the laser across the tunnel. The reference cell is shown.

tunnel, passing in front of the nozzle at an angle. The basic setup is visualized in **Figure 4.1**.

For this experiment, the angle the laser was sent across with was about 84°. Two *Thorlabs PDA10D2* photodiodes capable of measuring across 2.3 [μm] were placed, one past the reference cell and one on the other side of the tunnel. The carrier signal was a triangle wave at a frequency of 50 [Hz] with a sinusoid modulated atop it at 25 [kHz].

Procedure

To more finely recover the velocity of the tunnel, the data are fit (as described in Chapter One) to extract the shift in wavenumber. Fitting the data removes any uncertainties about the noise contribution to the velocity, but it also requires a higher concentration present to be accurate. These fittings do not carry over to any form of temperature or concentration analysis but are very useful for finding the velocity. Beginning with the baseline, it is fitted with a 4^{th} order polynomial plus a cosine term as in Eq. (29).

With the phase and the amplitude recovered from the fit of the baseline, the actual transmitted data are analyzed. To resolve the wavenumber shift with the most accuracy, phantom data are created mimicking the sinusoidal aspect by having the wavenumber ν as a function of time $\nu(t)$. When the phantom data are created, they are procedurally aligned and compared with the experimental data to recover the shift in wavenumber. Following the alignment of the phantom data, the theoretical fits are passed into a lock-in amplifier (LIA) using a 4th order Butterworth filter following Eqs. (30 – 32) substituting $n = 2$ to achieve the 2nd harmonic.

To ensure this process worked properly, a hot-wire anemometer was placed in a calibration system to manually read the velocity. This velocity was then compared to the WMS result and shown to be only 1 [m/s] off the returned result as shown in **Figure 4.2**.

Results

Following calibration, data were taken across the arcjet tunnel. These data were noisier than the calibration data, but velocities were still recoverable in some tests. Utilizing the

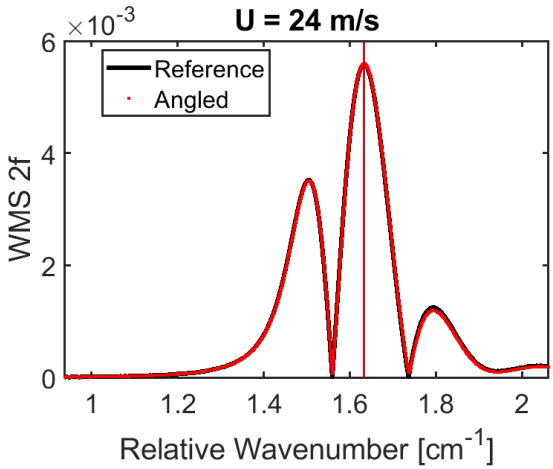


Figure 4.2. Velocity shift measured at 25 m/s with hot-wire anemometer and recovered at 24 m/s with WMS velocimetry.

same process as with the calibration data, the baseline and the data are fit and the velocity is recovered across a time-span in the tunnel. This is shown in **Figure 4.3**.

Velocities are recovered over nearly a second as the tunnel recirculated CO throughout. As the concentration of CO increased, the average velocity across the beam path decreased. Had more data been taken, the velocity would've continued to decrease. The velocity near the start is considered an approximation of the true tunnel freestream velocity.

Utilizing Eq. (58), the mole fraction of the CO may be recovered. The value is seen increasing in the tunnel over the same time period as shown in **Figure 4.4**.

$$\chi_{\text{measured}} = \frac{\left(\frac{2f}{1f}\right)_{\text{measured}}}{\left(\frac{2f}{1f}\right)_{\text{simulated}}} \chi_{\text{simulated}} \tag{58}$$

As expected, as more CO enters the tunnel and recirculates across the path of the laser beam, the average velocity measured decreases due to recirculation effects.

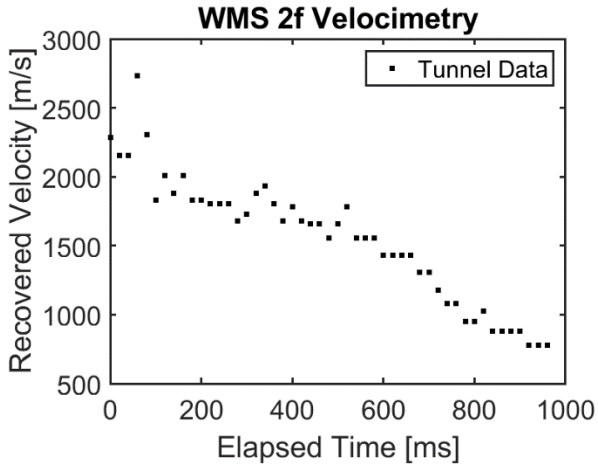


Figure 4.3. Recovered velocity from the measured CO in the tunnel.

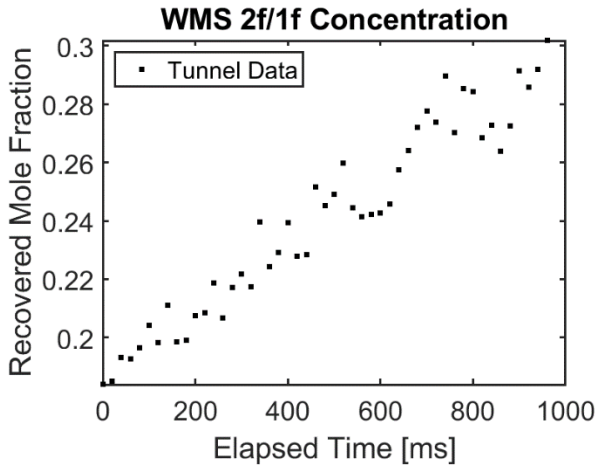


Figure 4.4. Recovered mole fraction from the measured CO in the tunnel.

Discussion of Failures

At the time of writing, this experiment is not yet completed to the extent desired. Even so, what has been discussed thus far is the work of several failures and dead ends. To expedite any furthering of this research, the largest of these failures are documented herein in the chronological order encountered.

To begin, pure LAS velocimetry was tried. A laser centered on 5263 [nm] measuring nitric oxide was fired through the tunnel in the similar setup as **Fig. 4.1**. The main difference with the first iteration is both beams were fired across the tunnel—one angled and one orthogonal as shown in **Fig. 4.5**. The idea was to measure the wavenumber shift purely from the oscilloscope as it should only show up on the angled beam; however, this proved an incorrect methodology. **Figure 4.6** shows the smallest error encountered. This error far exceeds the physical limits of the tunnel, so the data were scraped and the experiment rewritten.

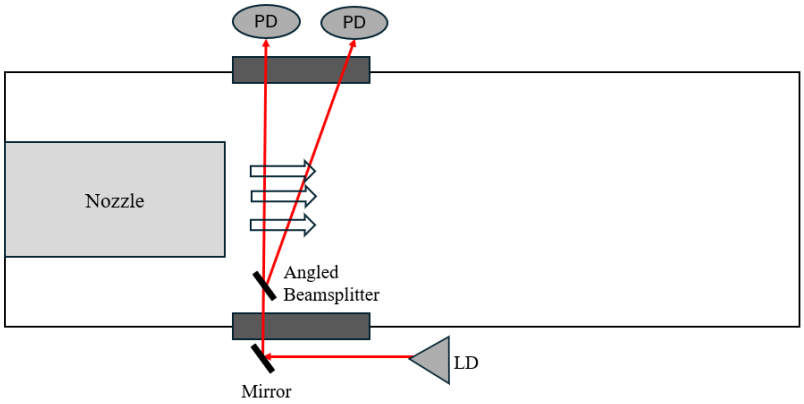


Figure 4.5. Original arcjet tunnel setup.

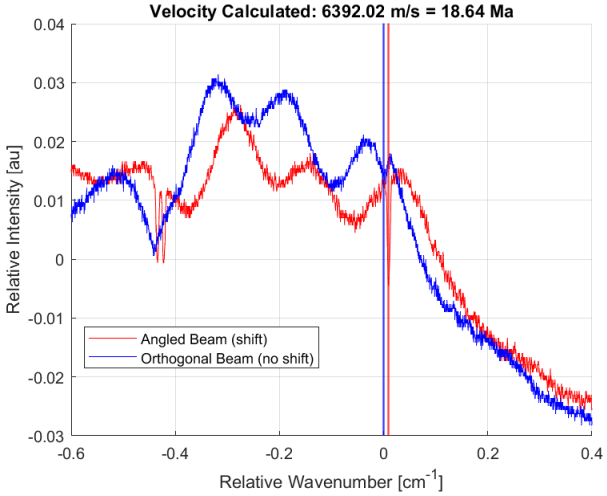


Figure 4.6. Velocity calculated from the tunnel using unaided LAS.

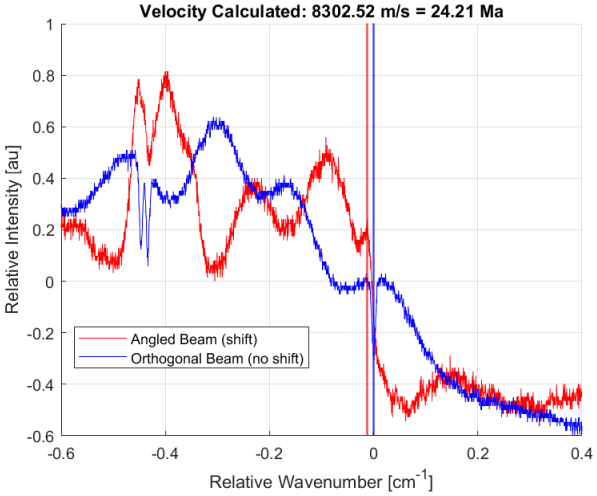


Figure 4.7. Velocity using an amplifier on the orthogonal beam.

At this point, it was assumed the photodiode measuring the orthogonal beam was too weak, so an amplifier was attached to it as in **Fig. 4.7**. This did not fix the issue.

After discussion with others who have run experiments similar to what was being attempted, it was concluded that what was being measured was recirculated NO, not the original flow. The tunnel was then tested in a large scan to measure when NO would first show up; 375 [ms] after the tunnel start—over a third of the total test time—before NO was even showing up on the oscilloscope.

At this point, it became time-consuming to test in the tunnel, so a Mach 1 jet was set up on a table-top experiment and the velocimetry modeling continued. Shown in **Fig. 4.8** is the setup and in **Fig. 4.9** the results of three consecutive runs. None show the value of 343 [m/s] expected even with the setup to double the measured wavenumber shift.

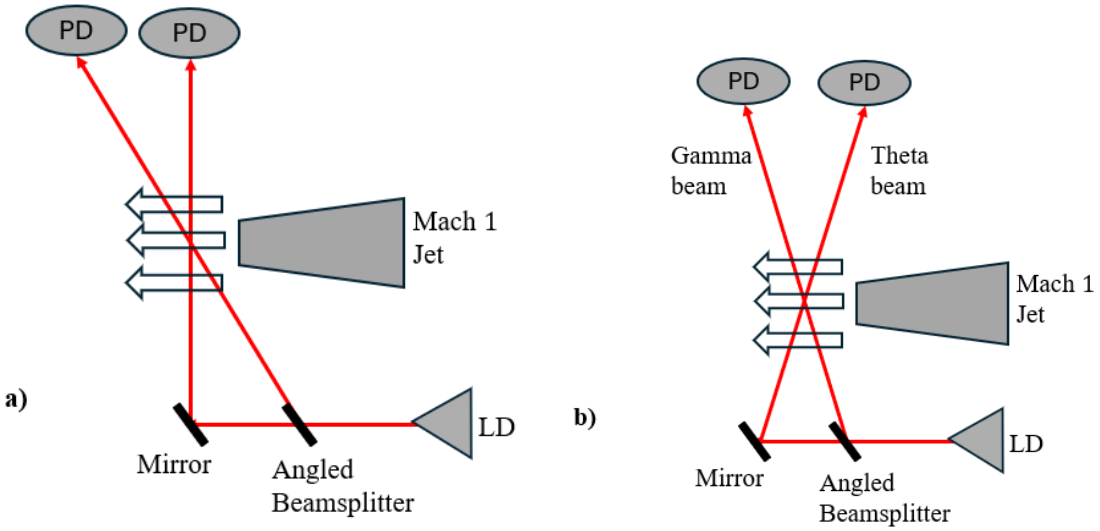


Figure 4.8. Two versions of the table-top setup. In (a), the orthogonal non-shifted beam is maintained. In (b), the beamsplitter and mirrors are arranged to maximize the shift measured.

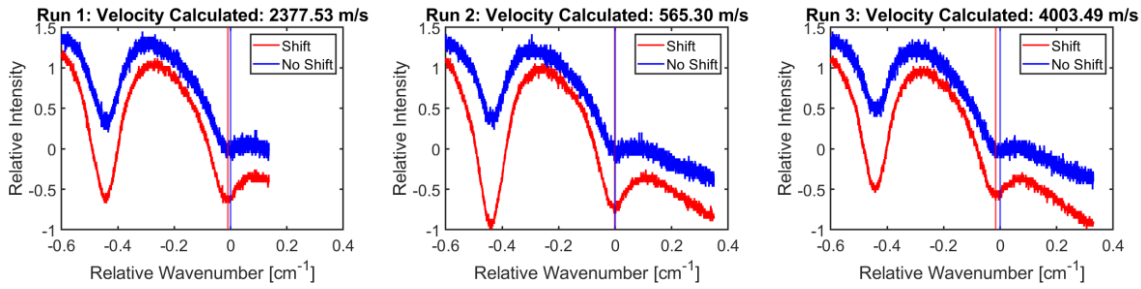


Figure 4.9. Three runs from the Mach 1 jet on the table-top experiment. All three answers are substantially different.

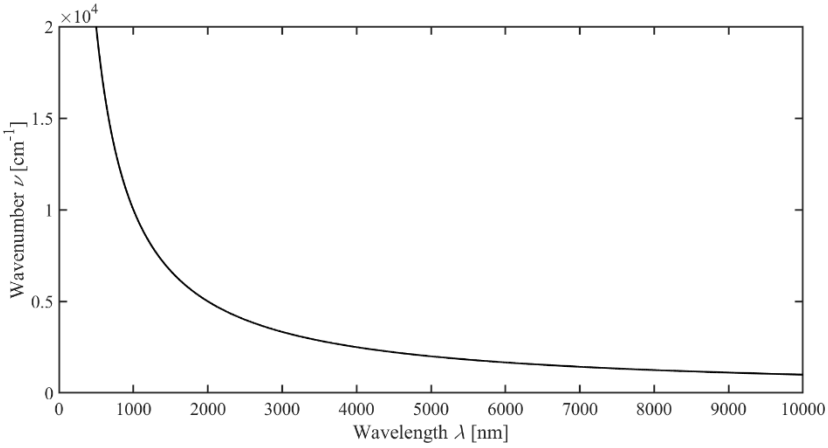


Figure 4.10. Wavenumber ν as a function of wavelength λ.

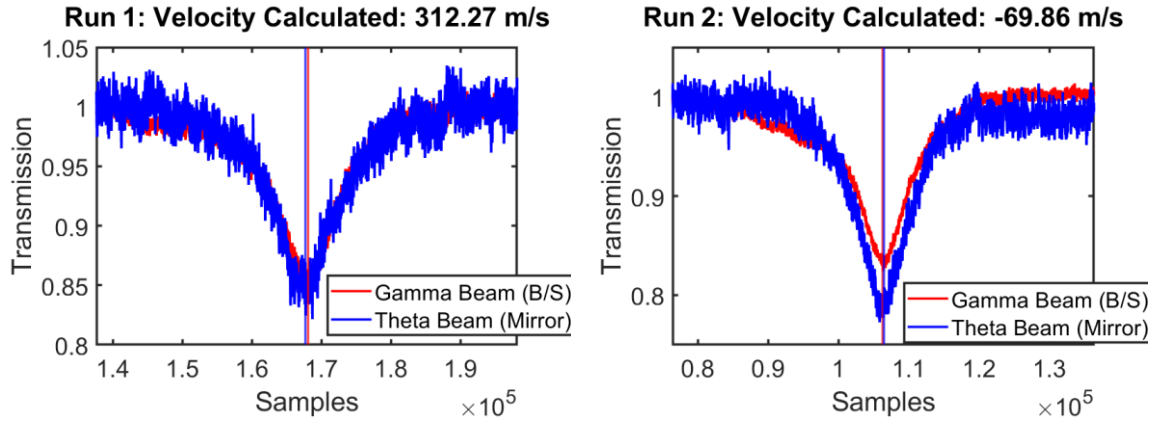


Figure 4.11. Velocity from Mach 1 jet utilizing CO. Beams 'Gamma' and 'Theta' refer to the setup in Fig. 4.8.

The issue was no longer assumed to be photodiode or facility, but the laser itself. In lieu of NO at 5263 [nm], CO at 2327 [nm] was employed. The velocimetry requires a wavenumber shift $\Delta\nu$ in $[\mathrm{cm}^{-1}]$ as in Eq. (33). The standard conversion from [nm] to $[\mathrm{cm}^{-1}]$ is: $[\mathrm{cm}^{-1}] = 10^7/[\mathrm{nm}]$. This results in larger wavelengths yielding smaller wavenumbers as in **Fig. 4.10**. Because of this, if the probing laser for the velocimetry is too far in the IR, the possible shift measurable in the wavenumber decreases. With the 2327 [nm] (4297 $[\mathrm{cm}^{-1}]$) laser, the wavenumber shift is essentially doubled allowing for more accurate measurements, but still the results lacked as in **Fig. 4.11**. It was only after this point, half a year into the experiment, WMS was used.

With the introduction of WMS, most errors went away. There were data-processing errors, difficulties working in the frequency domain, and noise errors; but when said and done, the WMS addition to the velocimetry measurement solved the largest problems as documented herein.

CHAPTER FIVE

SPARSE TOMOGRAPHIC RECONSTRUCTION OF TEMPERATURE AND CONCENTRATION IN AMMONIA FLAMES

Motivation

To reconstruct two-dimensional profiles of temperature and the concentration of some compound across a surface. To show the process can be done simply and efficiently for a flat, laminar flame. To calibrate the demonstrated process for use in more turbulent flows such as plasma torches or plasma jets to further hypersonic and material research.

Abstract

Two-dimensional temperature and nitric oxide concentration fields are reconstructed in a steady state NH_3–O_2-enriched air flame in a Hencken burner using spatially sparse laser absorption spectroscopy (LAS) and algebraic reconstruction tomography (ART). The flame is probed with two quantum cascade lasers centered at 5.263 [μm] and 5.397 [μm] respectively to obtain sparse line-of-sight absorbance measurements. Data are taken across the ammonia flame at equivalence ratios ranging from 0.7 to 1.3 in 0.1 increments, at discrete offset positions ($0 - 12.25$ [mm]), and at three axial heights (1, 2, and 3 [cm]) above the burner surface. The resulting limited-angle, underdetermined dataset is processed using ART to recover two-dimensional fields. The temperature field is obtained by two-line thermometry. This work demonstrates the feasibility and effectiveness of sparse tomographic methods for spatially resolved diagnostics in reactive flows, particularly in environments where full data coverage may be impractical.

Introduction

Ammonia Applications

Ammonia is currently being explored as an alternative fuel for carbon-free combustions [49,50]. Specific molecules can be targeted with laser spectroscopy, making it a useful

technique for the study of NO pollutant formation in ammonia combustion. As research advances from chambers to engines, turbines, and furnaces, nonintrusive spectroscopy measurements may still be collected *in situ* or *operando* to optimize experimental parameters. Ammonia combustion is rarely performed as a steady state experiment due to ignition variability, transient flow dynamics, and corrosive interactions with hardware.

Tomographic Application & Recovery

This work utilizes sparse experimental measurements to recover the temperature and concentration profile of an ammonia-oxygen-air combustion experiment. Spatially-resolved laser absorption spectroscopy (LAS), algebraic reconstruction tomography (ART), and thermometric evaluation are integrated as SLATE: a fully deterministic framework for evaluating sparse spectroscopic data without regularization.

LAS is a well-established diagnostic technique for *in situ* characterization of NO [51–58]. In this work, NO pollutant production in an adiabatic NH_3–O_2-enriched air flame is measured. ART has been used previously to resolve path-integrated LAS measurements spatially [14,59–63]. Sparse reconstruction, in which few data and viewing angles are available, affords the means of studying bench-scale laboratory experiments [64–66]. Recovered temperatures in this work are compared to an adiabatic NH_3–O_2-enriched air combustion simulation produced with Cantera [67].

This work recovers a two-dimensional temperature and concentration profile of NO across a laminar burner with minimal data input by utilizing assumptions of symmetry. Large LAS tomography setups in **Table 5.1** capture transient behavior using multiple tomography beams, spatial offsets, and viewing angles.

In contrast, small-scale experiments using low-power, non-divisible lasers have been limited to studying steady state conditions, as they are required to repeat measurements at different beam offsets. Such diagnostic setups prioritize accuracy over precision; by leveraging assumptions of symmetry, useful insights may still be recovered without expensive equipment. Studies on sparse tomographic reconstruction of LAS are compared in **Table 5.2**. SLATE recovers a reasonable estimate of temperature and concentration using a single laser for tomography, sparse spatial offsets, and limited-angle viewing. To suppress non-physical artifacts from ART, masking removes values above a set threshold and regularization smooths iterative results.

Setup

A laminar flame is produced via the combustion of premixed high purity (99.9989%) ammonia and oxygen-enriched air oxidizer in a Hencken burner. Fuel-to-oxidizer equivalence ratios φ as in [68] are shown in **Figure 5.1a**; combustion equipment is detailed in **Figure 5.1b**.

To compare the temperature and nitric oxide concentration produced by fuel-lean versus fuel-rich flows, equivalence ratios are varied between 0.7 and 1.3 in increments of 0.1. Oxygen enrichment has been shown in [68] to enhance the stability of an ammonia flame;

Table 5.1. Review of tomographic LAS literature.

Author	Tomography Laser Beams	Number of Spatial Offsets	Number of Angles
Upadhyay [59]	126	21	6
Sun [60]	16	1	2
Song [61]	31	2	1
Jeon [62]	16	1	3
Cai [14]	30	1	2
Song [63]	97	1	4

Table 5.2. Review of sparse tomographic LAS literature.

Author	Tomography Laser Beams	Number of Spatial Offsets	Number of Angles	Experiment Symmetry
Keller [64]	1	16	60	Circular
Steavenson [65]	1	23	81	Circular
Shi [66]	2	39	4	Square
Shi [69]	1	25	4	Circular
Feltis, Mandich	1	4	1	Square

an oxygen concentration of approximately forty percent in an atmospheric environment performs well. Gas flow is regulated with mass flow controllers from *Alicat Scientific* ($0 - 5 \pm 0.6\%$ [SLM]) for the ammonia fuel and *Omega Engineering* (*FMA5518A* $0 - 5 \pm 1\%$) for the oxygen and air oxidizers. The flowrate of air was adjusted per test to ensure a consistent combustion flowrate of 4.5 [SLM].

The optical diagnostics used for this experiment are shown in **Figure 5.2**. The laser centered at 1900 [cm^{-1}], shown in green, consist of a computer-controlled tunable *DFB* quantum cascade laser from *LD-PD Pte. Ltd*. and a mid-IR detector system from *VIGO Photonics* (*SIP-TO8* photodiode, *MHS-2* heatsink, and *PTCC-01 TEC* controller). The $7 - 10$ [mW] continuous wavelength beam has a diameter of 5 [mm]. The laser system centered at 1853 [cm^{-1}], shown in blue, includes a *Rigol DG812* arbitrary waveform generator (AWG), *Arroyo 6310-QCL ComboSource 1A QC*L Laser/60W TEC laser controller, *ALPES CW-SM-Q-1853.8-0.5-HHL-L* continuous wavelength laser, and *Vigo Photonics AIP-DC-1M-S* photodiode. The beam diameter of the 1853 [cm^{-1}] laser is 3 [mm]. Transmission intensity signals I_t from both lasers are viewed and saved using a *LeCroy Waverunner 62Xi* oscilloscope.

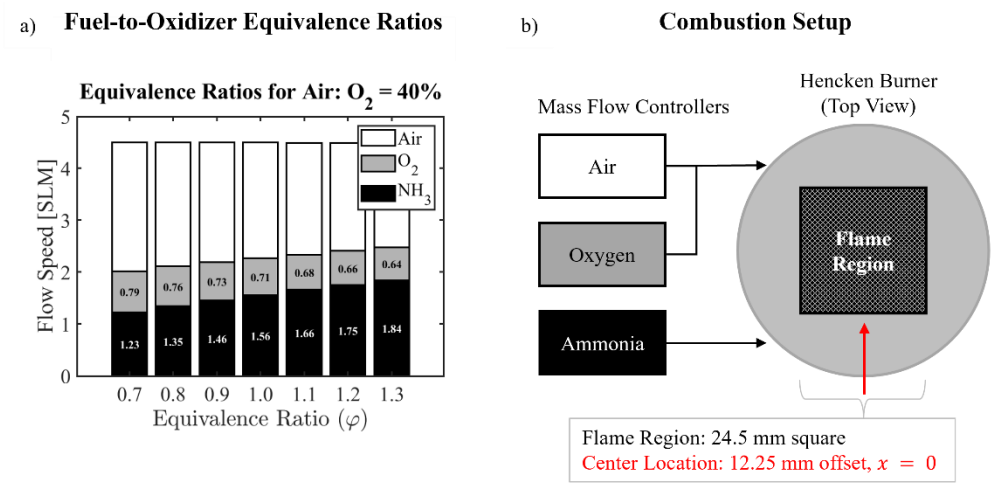


Figure 5.1. Combustion experiment with a) equivalence ratios and b) setup.

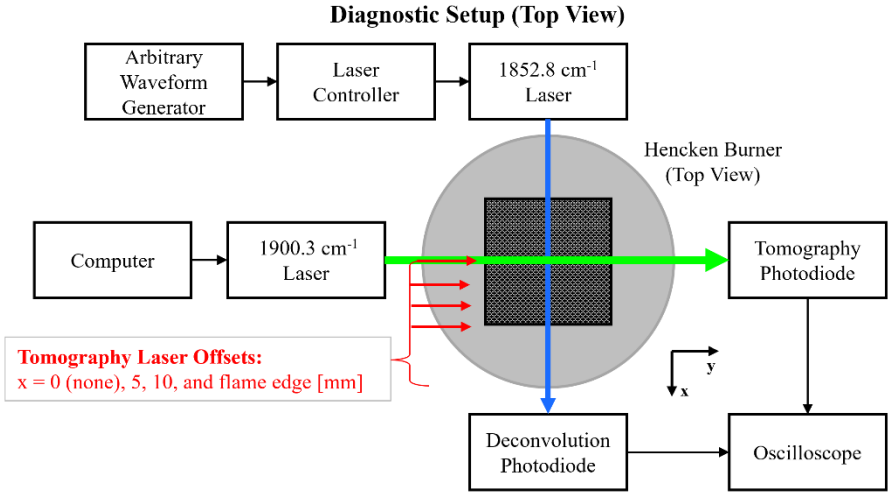


Figure 5.2. Diagnostic setup with 1900 [cm^{-1}] (green) and 1853 [cm^{-1}] (blue) laser beams.

An angled view of the diagnostic setup is shown in **Figure 5.3**. The square Hencken burner surface, outlined in black, is bisected by the beam paths of both the 1900 and 1853 [cm^{-1}] lasers. During the experiment, the 1900 [cm^{-1}] laser and photodiode pair are manually repositioned from the center ($x = 0$, 12.25 [mm] from the mesh edges) to 0.5 [mm] off center, 1.0 [mm] off center, and the flame edge where absorption is no longer visible on the oscilloscope. This horizontal x-offset is shown as red arrows in **Figures 5.2 – 5.3**. The 1853 [cm^{-1}] laser remains centered at $y = 0$. Absorption spectroscopy data are collected from both lasers at vertical offsets of $z = 1$, 2, and 3 [cm] by manually lowering the Hencken burner.

The spectral range for both lasers is shown in **Figure 5.4**. At elevated temperatures, three nitric oxide absorbance peaks from transitions $(0 \rightarrow 1)R_1(6.5)$, $(1 \rightarrow 2)R_1(16.5)$, and $(0 \rightarrow 1)R_2(6.5)$ appear in the spectral scanning range of the 1900 [cm^{-1}] laser. Two-line thermometry cannot be performed directly with the 1900 [cm^{-1}] laser signal, as peaks 2 and 3 are convolved with water vapor absorbance peaks 7, 8, and 9 shown in **Figure 5.5**. For this reason, the 1853 [cm^{-1}] laser system has been included to view a pure NO peak (peak 4, via transition $(0 \rightarrow 1)P_1(6.5)$).

Methodology

Laser Calibration and Signal Preprocessing

The 1900 [cm^{-1}] laser was calibrated by measuring NO at a known temperature, concentration, and pressure. From these data, a spline fit was created between the known theoretical wavenumber transition values and the measured peaks. As the 1853 [cm^{-1}] laser is capable of only measuring a single peak, the wavenumbers were assumed to be

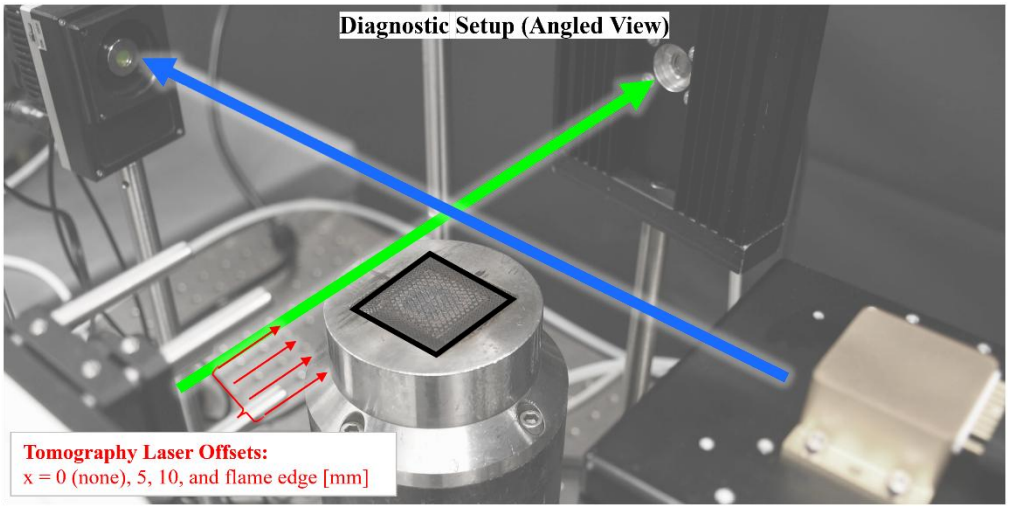


Figure 5.3. Diagnostic setup with 1900 $[cm^{-1}]$ laser offsets in red.

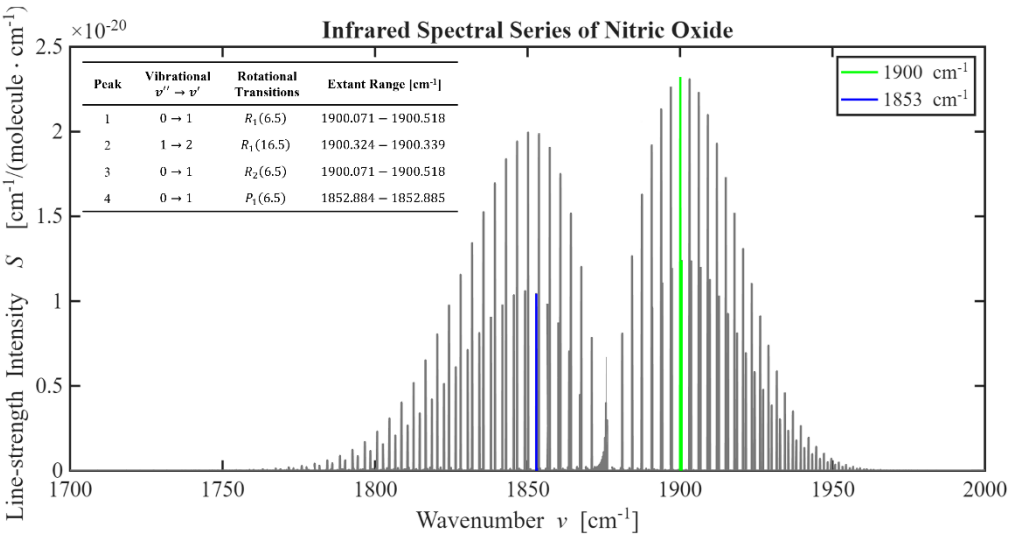


Figure 5.4. Spectral range for 1900 $[cm^{-1}]$ (green) and 1853 $[cm^{-1}]$ (blue) lasers.

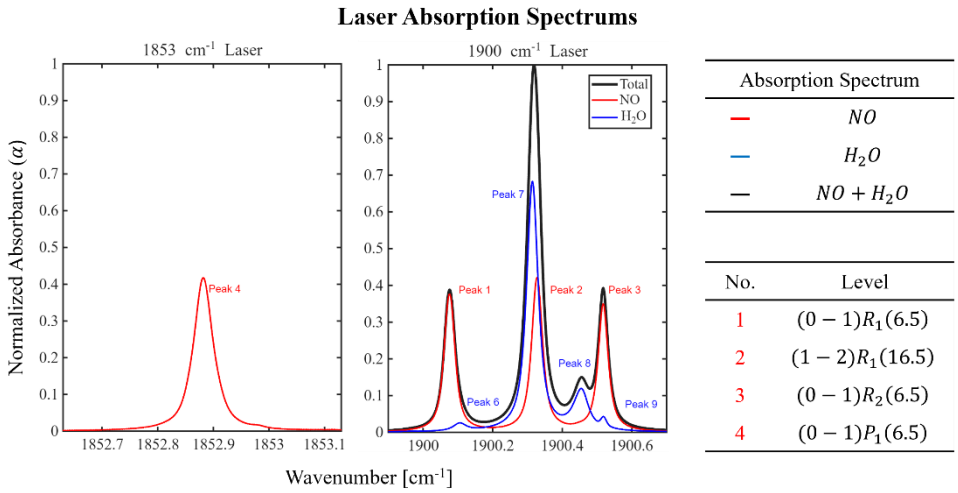


Figure 5.5. Laser absorption spectrums for nitric oxide (in red), water (in blue), and the convolved sum (in black).

linear and normalized theoretical values were used to find the optical limits of the scanning range at a known pressure and temperature. No etalon was necessary for this experiment.

To reduce system noise, 400 scans were collected with the 1900 $[\mathrm{cm}^{-1}]$ laser at 20 [kHz] and averaged. As the 1853 $[\mathrm{cm}^{-1}]$ laser was operated at a much lower frequency (100 [Hz]), the averaging was performed on the oscilloscope itself with 150 averages for each scan performed.

After the laser beam passes through the flame, absorption information is encoded within the beam, collected with photodiodes, and sent to the oscilloscope where it is quantified as intensity I_t with respect to time. Rather than directly measuring I_0 to solve Eq. (1), a baseline signal is mathematically generated by fitting a curve to the non-absorbing parts of I_t. The ramp signal produced by the AWG and the 1853 $[\mathrm{cm}^{-1}]$ laser is fit with a

third-order polynomial. The signal produced by the 1900 $[\mathrm{cm}^{-1}]$ laser is fit with a fourth-order Fourier-sine series.

The x-axes of the data scans are converted from time (t, in units of [s]) to frequency (ν, in units of $[\mathrm{cm}^{-1}]$). As shown in **Figure 5.5**, the 1853 $[\mathrm{cm}^{-1}]$ laser scan captures a single peak ($\nu_4 = 1852.88\ [\mathrm{cm}^{-1}]$) and the 1900 $[\mathrm{cm}^{-1}]$ laser contains three nitric oxide peaks ($\nu_{1,2,3} = 1900.08$, 1900.33, and 1900.52 $[\mathrm{cm}^{-1}]$) convolved with four water vapor peaks ($\nu_{6,7,8,9} = 1900.12$, 1900.32, 1900.45, and 1900.52 $[\mathrm{cm}^{-1}]$). These peaks are used to fit the experimental x-axis to the wavenumber ν for the 1900 $[\mathrm{cm}^{-1}]$ laser; pre-experiment calibration ensures accurate conversion for the 1853 $[\mathrm{cm}^{-1}]$ laser.

Signal Deconvolution

Individual absorbance peaks are isolated based on starting and ending wavenumbers to recover the integrated absorbance per peak, A_i. Two-line thermometry is used to ratio these integrated absorbances and recover the temperature for an assumption of local thermodynamic equilibrium (LTE) per tomographic beam X. To deconvolve nitric oxide

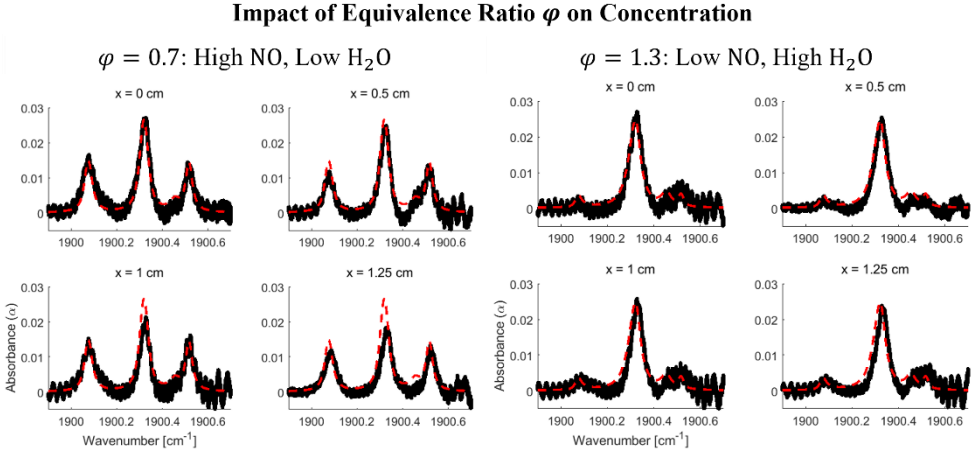


Figure 5.6. Impact of equivalence ratio φ on concentration.

and water vapor signals, peaks 1 and 4 are ratioed. Equivalence ratios $\varphi = 1.2, 1.3$ produce very little nitric oxide, as shown in **Figure 5.6**; therefore, for these conditions, water vapor peaks 6 and 7 are ratioed.

As shown in **Figure 5.7**, the ratio of peaks 1 and 4 does not change substantially when the absorbance of water vapor overtakes that of NO. This confirms that peak 1 is acceptable for thermometry. The LTE temperature is found from thermometry of peaks 1 and 4 in steps 1.1 and 1.2 of SLATE shown in **Figure 5.8**. An initial LTE estimate of concentration is found by iteratively fitting theoretical absorbance values with experimentally measured absorbance values in steps 1.3 and 1.4 in **Figure 5.8**. Absorbance is calculated with Eq. (34) and used to perform thermometry with Eq. (37).

Algebraic Reconstruction Tomography

To utilize Eq. (35) for ART, $\bar{b}_i$ and $\bar{A}$ are defined prior to iteration in steps 2.1–2.3 and 2.4 respectively shown in **Figure 5.9**. The $\bar{b}_i$ is comprised of the experimentally measured integrated absorbances under peak i multiplied by the pathlength l the absorbing laser takes through each individual cell. The geometry matrix $\bar{A}$ is formed from coordinate grid information (x, y) coupled with angle information θ known from the experimental setup. The total laser beam pathlength L is the summation of pathlengths per grid cell l. The ART algorithm in Eq. (36) is then applied in step 2.5 to solve for $\bar{x}_i$ per peak i.

In this work, integrated absorbance data are up-sampled $\pm 2°$ and duplicated at 90° to improve reconstruction. This is a modified version of an axisymmetric flame assumption; as the Hencken burner is a square, only two symmetry angles are reasonable. It is realistic

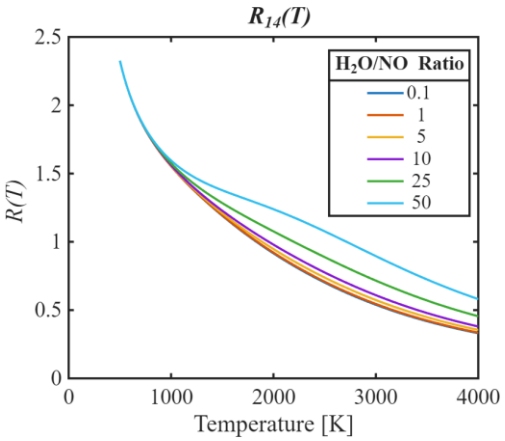


Figure 5.7. Ratio of peaks 1 and 4 for various convolutions.

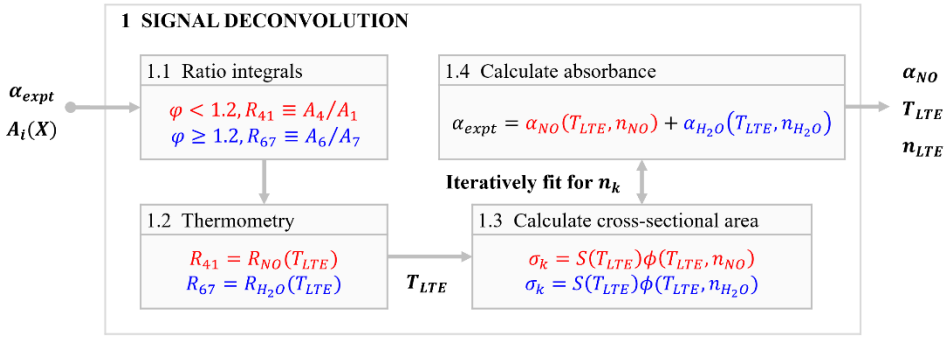


Figure 5.8. Deconvolution in SLATE.

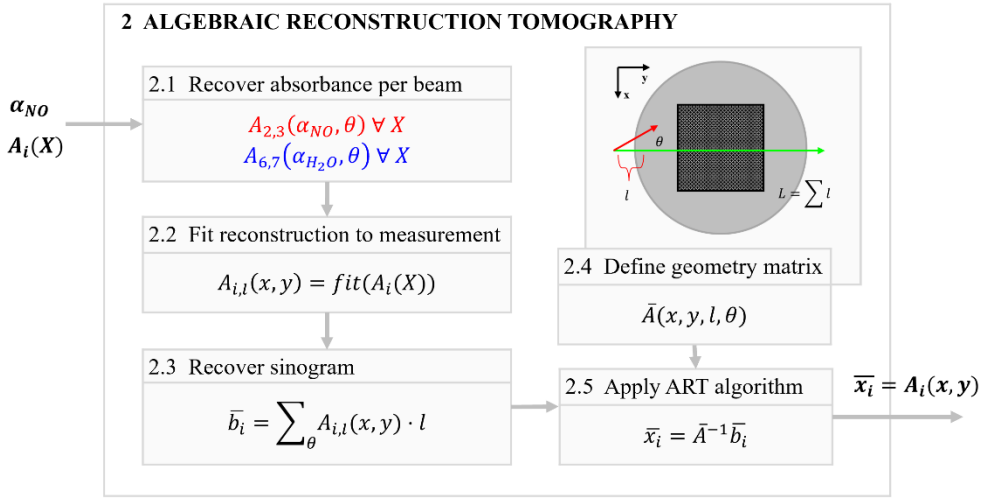


Figure 5.9. ART in SLATE.

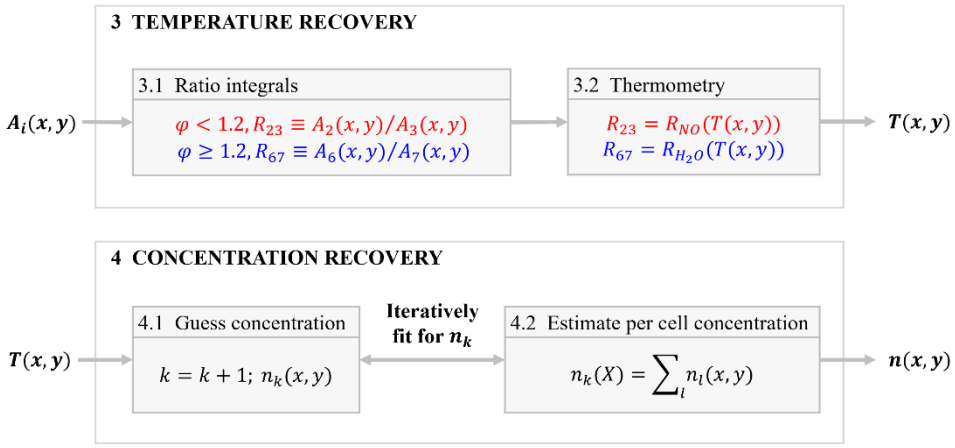


Figure 5.10. Temperature and concentration recovery in SLATE.

to assume that slight offsets yield similar results because the path length difference is smaller than the laser beam width.

Temperature and Concentration Recovery

Two-line thermometry is performed a second time in step 3 of SLATE shown in **Figure 5.10**. The spatially-resolved integrated absorbances $\bar{x}_i = A_i(x,y)$ are ratioed to infer temperature per grid point $T(x,y)$. Peaks 2 and 3 are used in place of peaks 1 and 4. In Step 4 of **Figure 5.10**, beam temperature $T(x,y)$ and an initial concentration guess $n_k = n_{LTE}$ are used to iteratively fit per-cell concentrations.

Experiment Reconstruction

Absorption cross-section per cell, $\sigma(x,y)$, is calculated in step 5.1 of **Figure 5.11** using spatially-resolved temperature $T(x,y)$ from step 3 and spatially-resolved concentration $n(x,y)$ from step 4. Theoretical beam-resolved cross-sectional areas are produced and compared with experimental results from step 1 to ensure validity. Viewed collectively, these individual profiles reveal the two-dimensional profile of nitric oxide temperature and concentration.

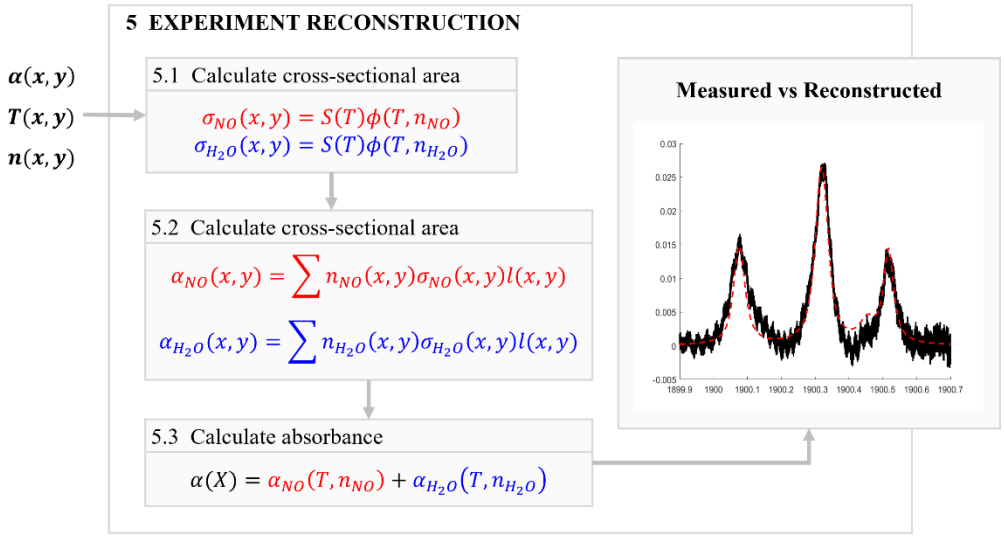


Figure 5.11. Experiment reconstruction in SLATE.

Results

Laser absorption was measured through an NH_3–O_2-enriched air flame at vertical offsets $z = 1, 2, 3$ [cm] and equivalence ratios $\varphi = 0.7, 0.8, 0.9, 1.0, 1.1, 1.2, 1.3$. Due to excess water vapor production at high equivalence ratios, only the first five values of φ are considered.

Figure 5.12 shows how temperature and nitric oxide concentration vary in different equivalence ratios. SLATE-reconstructed temperatures are close to the simulated adiabatic maximum (SAM) temperatures calculated via Cantera. Nitric oxide concentration diminishes as equivalence ratio increases.

Figure 5.13 shows how well the recovered absorbance spectra (in red) fit experimentally measured spectra (in black). The maximum percent error and the wavenumber of its occurrence are indicated for each spectrum and equivalence ratio. Experiment noise heavily influences the percent error and is discussed in the following section.

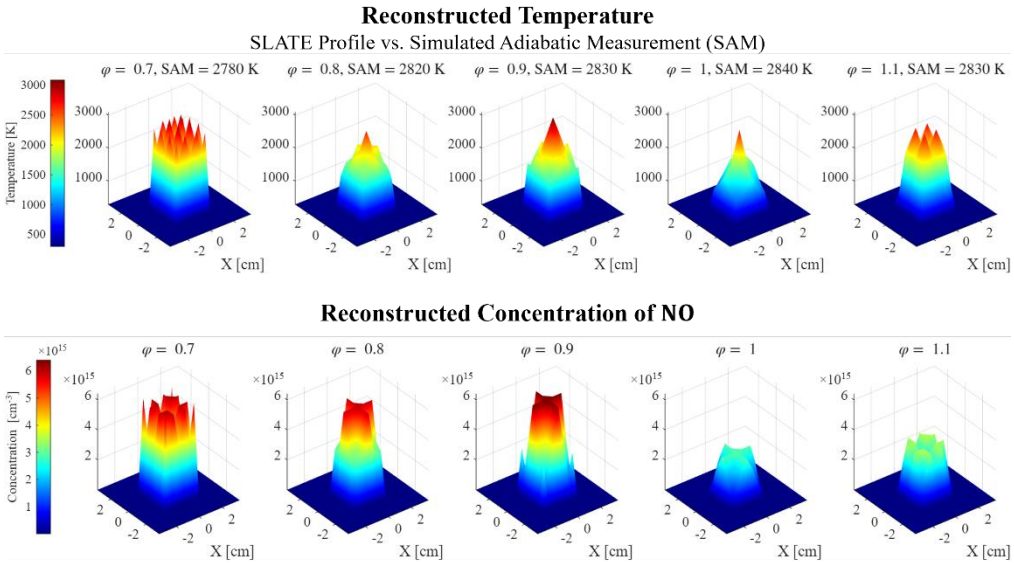


Figure 5.12. SLATE reconstruction of Hencken burner temperature and concentration.

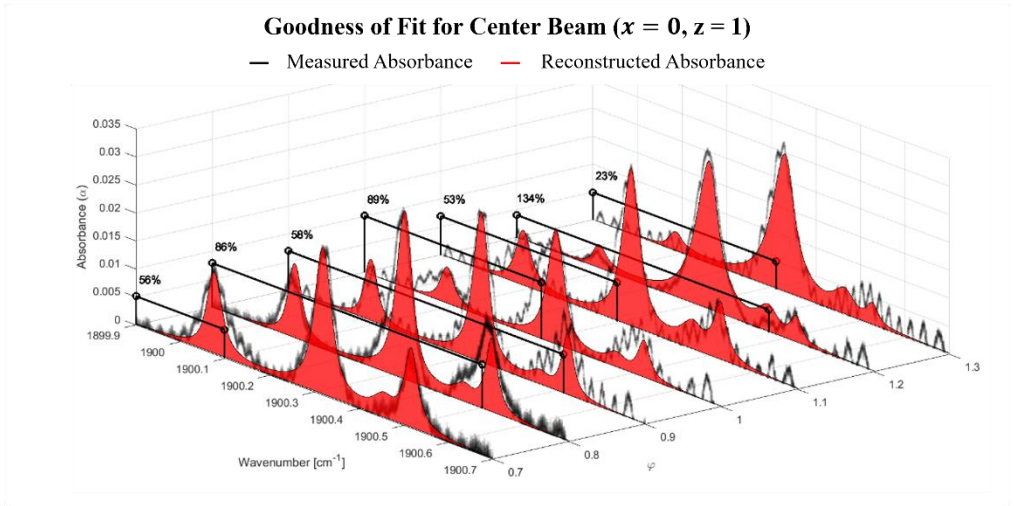


Figure 5.13. SLATE reconstruction of NO concentration [molecules/cm³].

Discussion of Measured Error

Several experimental and analytical precautions were taken to minimize and reduce noise in this experiment. Laser signal quality was improved by averaging over multiple scans. Appropriate oscilloscope bandwidths were chosen to help reduce oscilloscope internal noise. A $50\ [\Omega]$ resistor connection was utilized between the BNC cables and the oscilloscope to improve signal quality. The airflow around the experiment was made stagnant to minimize external fluctuations in the flame. Laser settings and laser alignment were carefully implemented to reduce signal distortion. Fit convergence, performed for spatial reconstruction and concentration recovery, was optimized with phantom data to find reasonable iteration termination conditions that converge without overfitting. Optimal geometry grid resolutions were found through trial-and-error using phantom data.

While the Hencken burner produces a laminar flow, there are still small changes in flame profile over time. These time-based variations are averaged over 400 scans with the $1900\ [\mathrm{cm}^{-1}]$ laser signal data, and can be considered negligible environmental fluctuations. To validate SLATE performance on phantom data, phantom tests were performed for perfect, noiseless data. The recovered spectra had a maximum percent error of 0.05% to the idealized value and an average error of 0.02%.

The datapoint with maximum percent error is highlighted in **Figure 5.13**. These values represent the largest error due to noise in the signal. Goodness of fit is not dependent solely on individual points but rather based on the qualitative fit of spectral peak areas. Individual point errors are provided for quantitative scale measurements of the absorbance.

Discussion of Failures

This experiment was not without error nor pause. At first, a simple open-air methane-oxygen flame was used and the 1900 [cm^{-1}] nitric oxide laser was measuring it. However, instead of the three peaks expected (nor even the convoluted peaks in **Fig. 5.5**), only one peak was visible directly in the middle of the signal. Some work was done in an effort to identify the peak as shown in **Fig. 5.14**.

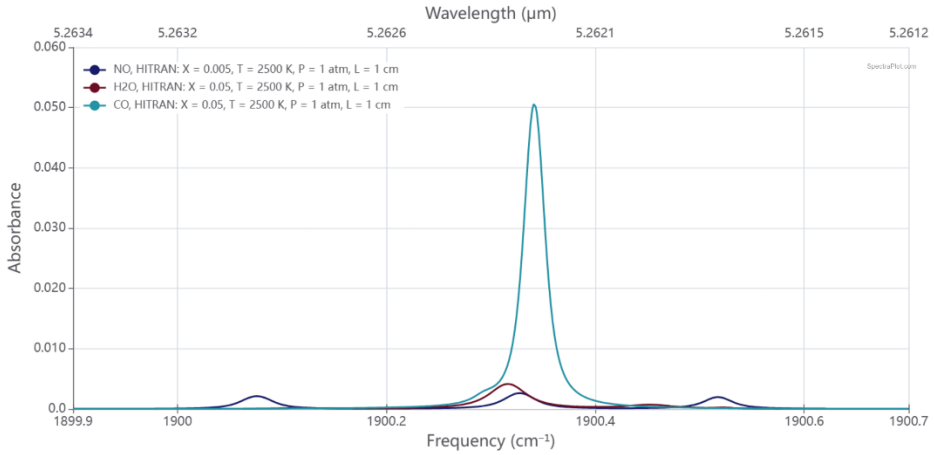


Figure 5.14. SpectraPlot analysis of NO, H_2O, and CO. The largest peak is CO.

Supposing a carbon monoxide peak had snuck its way into the signal, a carbon monoxide laser (2327 [nm]) was attached to the system to identify and remove the compound. Attaching the laser yielded no results however as no CO was measured by the second laser. Unable to identify the peak (and unable to then do any analysis on it), the fuel was changed from methane to ammonia. This had the benefit of forcing the compounds produced to be independent of carbon.

The second error encountered with the now ammonia-oxygen flame involved the presence of water in the signal. First, it was presumed that the 1900 [cm^{-1}] laser measured only NO as in the experiment in the HXT (Chapter Three). However, at elevated temperatures, the spectrum measured by the laser is heavily influenced by water vapor (**Fig. 5.5**). As with the carbon monoxide, the first assumption was to include a laser capable of measuring water vapor (1392 [nm]) in order to subtract the result out of the signal. This did not work as 1392 [nm] measures water vapor at room temperature as well so the resulting signal was oversaturated with a temperature measurement of 300 [K] and no further progress was made.

Recovering an initial estimate of the temperature of the flame was deemed necessary to deconvolve the signal. As such, the 1853 [cm^{-1}] laser (measuring solely NO) was utilized. Seen in **Fig. 5.5**, the 1853 [cm^{-1}] laser provides a second peak for two-line thermometry (peak 4 in the figure), allowing for the initial temperature estimate that begins the whole of the SLATE analysis.

CHAPTER SIX

CONCLUSIONS AND FUTURE WORK

Conclusions

On Chapter Two

To study material degradation and ablation, TDLAS and MS are combined. The fusion characterizes outgassing effects from commercial carbon materials undergoing thermal dissociation. Data were collected unobtrusively using LAS while pyrolyzing a sample of carbon phenolic composite in a dilatometer furnace. Exhaust was directed to an optical cell whereupon the absolute concentration of methane gas was measured at various stages of the pyrolysis process via TDLAS. As the gases were cycled through to a fume hood, a sample of the gas was redirected to an MS probe wherein the relative intensities of the various gases were measured and recorded. The resulting combination of TDLAS and MS recovered the absolute concentrations of every gas measured. The current outcomes from this experiment have returned promising results; the demonstrated technique may be useful for a variety of applications ranging from material sciences and analysis to aerodynamic tunnel testing and characterization. Future work may involve increasing the pathlength of the laser within the Herriott cell to provide higher resolution of concentration.

With the system in place and functioning properly, real-time exhaust data may be analyzed and parsed. All work done in this experiment was done manually, but the procedure lends itself well to automation. Exploring avenues from car exhaust to jet

engines, heat shield outgassing to fumes in chicken coops give this TDLAS/MS analysis system much room to expand.

On Chapter Three

TDLAS, alongside an RVT model of NO, has been utilized to characterize the rotational and vibrational temperature evolution, as well as the concentration evolution of flow behind a normal shock in an expansion tunnel. From the measurable wavelengths of the IR laser, only NO was measured with negligible interference from other molecular species. These measurements were temporally resolved to provide experiment progression information for rotational and vibrational temperature as well as NO concentration during the approximately 1 [ms] run time for the facility. Further, topics from Chapter Four may be applied to simultaneously recover the velocity of the flow with the rotational and vibrational temperatures. With the splitting of the spectrum into rotational (translational) and vibrational bands, the RVT model can be applied to any system where thermal nonequilibrium will be present.

On Chapter Four

Using the second harmonic of the wavelength modulated signal of carbon monoxide around 2.3 [μm] allows for the reasonable recovery of the velocity of the tunnel running with cold flow. The measured velocity of the CO in the tunnel begins over Mach 6 and steadily decreases as an increased concentration of CO recirculates in the test section. Further analysis of the tunnel may be performed with lasers of other wavelengths. Mid-IR ranges around 5.26 [μm] or near-visible around 0.8 [μm] would further corroborate the

tunnel's speed. Furthermore, future work may incorporate temperature analyses of the normalized $2f/1f$ WMS signals.

Temperature analysis of the system will require a database of harmonic signals. As the shape of the normalized WMS signal is temperature dependent, however, a minimized error comparison between the experimentally recovered shape and the simulated phantom shape will yield the temperature within whatever margin of error is chosen.

On Chapter Five

This work has demonstrated the reconstruction of two-dimensional temperature and nitric oxide concentration fields in Hencken burner flames using sparse laser absorption measurements and algebraic reconstruction tomography. Various equivalence ratios for NH_3–O_2-enriched air combustion are measured; processed absorbance spectra are recovered and analyzed. Two-dimensional temperature and concentration profiles are determined via SLATE.

The results confirm that sparse tomographic methods can yield reliable spatially resolved diagnostics without the need for extensive data coverage, making them both practical and cost-effective for certain applications. Beyond validating the approach for Hencken flames, this study establishes a robust framework that can be extended to more complex combustion systems, where full-field optical access is often limited. Future work will include validating the SLATE technique against turbulent datasets and high-enthalpy environments. Further expansion to include and evaluate different molecules, flame spatial profiles, and combustion parameters will also be considered. SLATE may be

further purposed into highly turbulent flows provided an increase in geometric resolution is in place.

Benediction

Benedicat tibi Dominus et custodiat te.

Ostendat Dominus faciem suam tibi et misereatur tui.

Conuertat Dominus uultum suum ad te et det tibi pacem.

Quicquid opus perficiatur, Deus omnipotens id benedicat.

Samuelis Feltis, seruus Altissimi, hoc opus fecit.

LIST OF REFERENCES

[1] Sweetland, K., Combs, C. S., Schmisseur, J. D., Rhodes, R., Zhang, F.-Y., Moeller, T. M., and Plemmons, D. H., "Development of MIR TLAS System with Applications to Reacting Hot Gas Flows," presented at the 2018 AIAA Aerospace Sciences Meeting, 2018. https://doi.org/10.2514/6.2018-1023

[2] Nair, A. P., Lee, D. D., Pineda, D. I., Kriesel, J., Hargus, W. A., Bennewitz, J. W., Danczyk, S. A., and Spearrin, R. M., "MHz Laser Absorption Spectroscopy via Diplexed RF Modulation for Pressure, Temperature, and Species in Rotating Detonation Rocket Flows," *Applied Physics B*, Vol. 126, No. 8, 2020, p. 138. https://doi.org/10.1007/s00340-020-07483-8

[3] Sanders, S. T., Wang, J., Jeffries, J. B., and Hanson, R. K., "Diode-Laser Absorption Sensor for Line-of-Sight Gas Temperature Distributions," *Applied Optics*, Vol. 40, No. 24, 2001, p. 4404. https://doi.org/10.1364/AO.40.004404

[4] Hansemann, C., Bonarens, M., König, D., Hülsbruch, D., Ströhle, J., Epple, B., and Wagner, S., "Reconstruction of Spatially Resolved Gas Phase Parameters from Single Line-of-Sight TDLAS Measurements of Oxy-Fuel Biomass Combustion in a Semi-Industrial Combustion Chamber," *Applications in Energy and Combustion Science*, 2026, p. 100498. https://doi.org/10.1016/j.jaecs.2026.100498

[5] Feltis, S. E., Zhang, Z., Dean, T. S., Bowersox, R. D. W., Siddiqui, F., and Gragston, M., "Measurements of No Rotational and Vibrational Temperatures behind a Normal Shock in Hypervelocity Flow via Absorption Spectroscopy,"

Experiments in Fluids, Vol. 65, No. 7, 2024, p. 112. https://doi.org/10.1007/s00348-024-03841-w

[6] Liu, Y., Lin, J., Huang, G., Guo, Y., and Duan, C., "Simple Empirical Analytical Approximation to the Voigt Profile," *Journal of the Optical Society of America B*, Vol. 18, No. 5, 2001, p. 666. https://doi.org/10.1364/JOSAB.18.000666

[7] Gordon, I. E., Rothman, L. S., Hargreaves, R. J., Hashemi, R., Karlovets, E. V., Skinner, F. M., Conway, E. K., Hill, C., Kochanov, R. V., Tan, Y., Wcisło, P., Finenko, A. A., Nelson, K., Bernath, P. F., Birk, M., Boudon, V., Campargue, A., Chance, K. V., Coustenis, A., Drouin, B. J., Flaud, J. –M., Gamache, R. R., Hodges, J. T., Jacquemart, D., Mlawer, E. J., Nikitin, A. V., Perevalov, V. I., Rotger, M., Tennyson, J., Toon, G. C., Tran, H., Tyuterev, V. G., Adkins, E. M., Baker, A., Barbe, A., Canè, E., Császár, A. G., Dudaryonok, A., Egorov, O., Fleisher, A. J., Fleurbaey, H., Foltynowicz, A., Furtenbacher, T., Harrison, J. J., Hartmann, J. –M., Horneman, V. –M., Huang, X., Karman, T., Karns, J., Kassi, S., Kleiner, I., Kofman, V., Kwabia–Tchana, F., Lavrentieva, N. N., Lee, T. J., Long, D. A., Lukashevskaya, A. A., Lyulin, O. M., Makhnev, V. Yu., Matt, W., Massie, S. T., Melosso, M., Mikhailenko, S. N., Mondelain, D., Müller, H. S. P., Naumenko, O. V., Perrin, A., Polyansky, O. L., Raddaoui, E., Raston, P. L., Reed, Z. D., Rey, M., Richard, C., Tóbiás, R., Sadiek, I., Schwenke, D. W., Starikova, E., Sung, K., Tamassia, F., Tashkun, S. A., Vander Auwera, J., Vasilenko, I. A., Vigasin, A. A., Villanueva, G. L., Vispoel, B., Wagner, G., Yachmenev, A., and Yurchenko, S. N., "The HITRAN2020 Molecular Spectroscopic Database,"

Journal of Quantitative Spectroscopy and Radiative Transfer, Vol. 277, 2022, p. 107949. https://doi.org/10.1016/j.jqsrt.2021.107949

[8] Hanson, R. K., Spearrin, R. M., and Goldenstein, C. S., "Spectroscopy and Optical Diagnostics for Gases," Springer International Publishing, Cham, 2016. https://doi.org/10.1007/978-3-319-23252-2

[9] Reisel, J. R., Carter, C., and Laurendeau, N., "EINSTEIN COEFFICIENTS FOR ROTATIONAL LINES OF THE (0, 0)BAND OF THE NO A2E+-X2I-[SYSTEM."

[10] Reisel, J. R., Carter, C. D., and Laurendeau, N. M., "Einstein Coefficients for Rotational Lines of the (0, 0) Band of the NO A2Σ+-X2π System," *Journal of Quantitative Spectroscopy and Radiative Transfer*, Vol. 47, No. 1, 1992, pp. 43–54. https://doi.org/10.1016/0022-4073(92)90078-I

[11] Sun, K., Chao, X., Sur, R., Goldenstein, C. S., Jeffries, J. B., and Hanson, R. K., "Analysis of Calibration-Free Wavelength-Scanned Wavelength Modulation Spectroscopy for Practical Gas Sensing Using Tunable Diode Lasers," *Measurement Science and Technology*, Vol. 24, No. 12, 2013, p. 125203. https://doi.org/10.1088/0957-0233/24/12/125203

[12] Sun, K., Chao, X., Sur, R., Jeffries, J. B., and Hanson, R. K., "Wavelength Modulation Diode Laser Absorption Spectroscopy for High-Pressure Gas Sensing," *Applied Physics B*, Vol. 110, No. 4, 2013, pp. 497–508. https://doi.org/10.1007/s00340-012-5286-0

[13] Hansen, P. C., Jørgensen, J. S., Lionheart, W. R. B., Andersen, M. S., Batenburg, K. J., Dong, Y., Quinto, E. T., and Sijbers, J., Eds., "Computed Tomography: Algorithms, Insight, and Just Enough Theory," Society for Industrial and Applied Mathematics, Philadelphia, 2021.

[14] Cai, W., and Kaminski, C. F., "Tomographic Absorption Spectroscopy for the Study of Gas Dynamics and Reactive Flows," *Progress in Energy and Combustion Science*, Vol. 59, 2017, pp. 1–31. https://doi.org/10.1016/j.pecs.2016.11.002

[15] Guha, A., "Tomographic Imaging of Combustion Zones Using Tunable Diode Laser Absorption Spectroscopy (TDLAS)," Doctor of Philosophy. Louisiana State University and Agricultural and Mechanical College, 2014. https://doi.org/10.31390/gradschool_dissertations.3393

[16] Hansen, P. C., and Jørgensen, J. S., "AIR Tools II: Algebraic Iterative Reconstruction Methods, Improved Implementation," *Numerical Algorithms*, Vol. 79, No. 1, 2018, pp. 107–137. https://doi.org/10.1007/s11075-017-0430-x

[17] Chen, S., Qiu, L., and Cheng, H.-M., "Carbon-Based Fibers for Advanced Electrochemical Energy Storage Devices," *Chemical Reviews*, Vol. 120, No. 5, 2020, pp. 2811–2878. https://doi.org/10.1021/acs.chemrev.9b00466

[18] Gohardani, O., Elola, M. C., and Elizetxea, C., "Potential and Prospective Implementation of Carbon Nanotubes on next Generation Aircraft and Space Vehicles: A Review of Current and Expected Applications in Aerospace Sciences," *Progress in Aerospace Sciences*, Vol. 70, 2014, pp. 42–68. https://doi.org/10.1016/j.paerosci.2014.05.002

[19] Ramasubramanian, B., Sundarrajan, S., Rao, R. P., Reddy, M., Chellappan, V., and Ramakrishna, S., "Novel Low-Carbon Energy Solutions for Powering Emerging Wearables, Smart Textiles, and Medical Devices.," *Energy & Environmental Science*, Vol. 15, No. 12, 2022, pp. 4928–4981. https://doi.org/DOI%2509https://doi.org/10.1039/D2EE02695C

[20] Bessire, B. K., and Minton, T. K., "Decomposition of Phenolic Impregnated Carbon Ablator (PICA) as a Function of Temperature and Heating Rate," *ACS Applied Materials & Interfaces*, Vol. 9, No. 25, 2017, pp. 21422–21437. https://doi.org/10.1021/acsami.7b03919

[21] Kayacan, İ., and Doğan, Ö. M., "Pyrolysis of Low and High Density Polyethylene. Part I: Non-Isothermal Pyrolysis Kinetics," *Energy Sources, Part A: Recovery, Utilization, and Environmental Effects*, Vol. 30, No. 5, 2008, pp. 385–391. https://doi.org/10.1080/15567030701457079

[22] Bessire, B. K., "Pyrolysis of Thermal Protection System Materials: Molar Yields of Volatile Products Derived from in Situ Mass Spectrometric Measurements," 2018. Retrieved 5 January 2023. https://scholarworks.montana.edu/xmlui/handle/1/14537

[23] Lachaud, J., Scoggins, J. B., Magin, T. E., Meyer, M. G., and Mansour, N. N., "A Generic Local Thermal Equilibrium Model for Porous Reactive Materials Submitted to High Temperatures," *International Journal of Heat and Mass Transfer*, Vol. 108, 2017, pp. 1406–1417. https://doi.org/10.1016/j.ijheatmasstransfer.2016.11.067

[24] Rabinovitch, J., Marx, V. M., and Blanquart, G., "Pyrolysis Gas Composition for a Phenolic Impregnated Carbon Ablator Heatshield," *11th AIAA/ASME Joint Thermophysics and Heat Transfer Conference*, American Institute of Aeronautics and Astronautics, 2014. https://doi.org/10.2514/6.2014-2246

[25] Torres-Herrador, F., Meurisse, J. B. E., Panerai, F., Blondeau, J., Lachaud, J., Bessire, B. K., Magin, T. E., and Mansour, N. N., "A High Heating Rate Pyrolysis Model for the Phenolic Impregnated Carbon Ablator (PICA) Based on Mass Spectroscopy Experiments," *Journal of Analytical and Applied Pyrolysis*, Vol. 141, 2019, p. 104625. https://doi.org/10.1016/j.jaap.2019.05.014

[26] Wong, H.-W., Peck, J., Assif, J., Panerai, F., Lachaud, J., and Mansour, N. N., "Detailed Analysis of Species Production from the Pyrolysis of the Phenolic Impregnated Carbon Ablator," *Journal of Analytical and Applied Pyrolysis*, Vol. 122, 2016, pp. 258–267. https://doi.org/10.1016/j.jaap.2016.09.016

[27] Williams, P. T., and Williams, E. A., "Interaction of Plastics in Mixed-Plastics Pyrolysis," *Energy & Fuels*, Vol. 13, No. 1, 1999, pp. 188–196. https://doi.org/10.1021/ef980163x

[28] Goldenstein, C. S., Spearrin, R. M., Jeffries, Jay. B., and Hanson, R. K., "Infrared Laser-Absorption Sensing for Combustion Gases," *Progress in Energy and Combustion Science*, Vol. 60, 2017, pp. 132–176. https://doi.org/10.1016/j.pecs.2016.12.002

[29] Urban, P. L., "Quantitative Mass Spectrometry: An Overview," *Philosophical Transactions of the Royal Society A: Mathematical, Physical and Engineering*

Sciences, Vol. 374, No. 2079, 2016, p. 20150382. https://doi.org/10.1098/rsta.2015.0382

[30] Jatana, G. S., Perfetto, A. K., Geckler, S. C., and Partridge, W. P., "Absorption Spectroscopy Based High-Speed Oxygen Concentration Measurements at Elevated Gas Temperatures," *Sensors and Actuators B: Chemical*, Vol. 293, 2019, pp. 173–182. https://doi.org/10.1016/j.snb.2019.04.143

[31] "Gas Analysis System | Mass Spectrometer | Manufacturer," Hiden Analytical. Retrieved 7 February 2023. https://www.hidenanalytical.com/products/gas-analysis/hpr-20-rd/

[32] Park, C., "Assessment of Two-Temperature Kinetic Model for Ionizing Air," *Journal of Thermophysics and Heat Transfer*, Vol. 3, No. 3, 1989, pp. 233–244. https://doi.org/10.2514/3.28771

[33] Wada, Y., Ogawa, S., and Kubota, H., "Thermo-Chemical Models for Hypersonic Flows," *Computers & Fluids*, Vol. 22, No. 2, 1993, pp. 179–187. https://doi.org/10.1016/0045-7930(93)90049-F

[34] Bond, R. B., Tatum, K., Power, G. D., and Tuckey, T., "Capabilities of HPCMP CREATE-AV Kestrel V11 for Hypersonic Flight and Ground Testing with a Two-Temperature Model," *AIAA Scitech 2021 Forum*, American Institute of Aeronautics and Astronautics. https://doi.org/10.2514/6.2021-0236

[35] Passiatore, D., Sciacovelli, L., Cinnella, P., and Pascazio, G., "Thermochemical Non-Equilibrium Effects in Turbulent Hypersonic Boundary Layers," *Journal of Fluid Mechanics*, Vol. 941, 2022, p. A21. https://doi.org/10.1017/jfm.2022.283

[36] Sweetland, K., Combs, C. S., Schmisseur, J. D., Rhodes, R., Zhang, F.-Y., Moeller, T. M., and Plemmons, D. H., "Development of MIR TLAS System with Applications to Reacting Hot Gas Flows," presented at the 2018 AIAA Aerospace Sciences Meeting, 2018. https://doi.org/10.2514/6.2018-1023

[37] Girard, J. J., Finch, P. M., Strand, C. L., Hanson, R. K., Yu, W. M., Austin, J. M., and Hornung, H. G., "Measurements of Reflected Shock Tunnel Freestream Nitric Oxide Temperatures and Partial Pressure," *AIAA Journal*, Vol. 59, No. 12, 2021, pp. 5266–5275. https://doi.org/10.2514/1.J060596

[38] Wehe, S., Baer, D., Hanson, R., Wehe, S., Baer, D., and Hanson, R., "Tunable Diode-Laser Absorption Measurements of Temperature, Velocity, and H2O in Hypervelocity Flows," presented at the 33rd Joint Propulsion Conference and Exhibit, 1997. https://doi.org/10.2514/6.1997-3267

[39] Chang, L. S., Strand, C. L., Jeffries, J. B., Hanson, R. K., Diskin, G. S., Gaffney, R. L., and Capriotti, D. P., "Supersonic Mass-Flux Measurements via Tunable Diode Laser Absorption and Nonuniform Flow Modeling," *AIAA Journal*, Vol. 49, No. 12, 2011, pp. 2783–2791. https://doi.org/10.2514/1.J051118

[40] Schultz, I. A., Goldenstein, C. S., Strand, C. L., Jeffries, J. B., Hanson, R. K., and Goyne, C. P., "Hypersonic Scramjet Testing via TDLAS Measurements of Temperature and Column Density in a Reflected Shock Tunnel," presented at the 52nd Aerospace Sciences Meeting, 2014. https://doi.org/10.2514/6.2014-0389

[41] Parker, R., Wakeman, T., Holden, M., and MacLean, M., "Measuring Nitric Oxide Freestream Concentration Using Quantum Cascade Lasers at CUBRC," *44th AIAA*

Aerospace Sciences Meeting and Exhibit, American Institute of Aeronautics and Astronautics, 2006. https://doi.org/10.2514/6.2006-926

[42] Finch, P. M., Girard, J., Strand, C., Yu, W., Austin, J., Hornung, H., and Hanson, R., "Measurements of Time-Resolved Air Freestream Nitric Oxide Rotational, Vibrational Temperature and Concentration in the T5 Reflected Shock Tunnel," *AIAA Propulsion and Energy 2020 Forum*, American Institute of Aeronautics and Astronautics. https://doi.org/10.2514/6.2020-3714

[43] Weisberger, J. M., DesJardin, P., MacLean, M. G., Parker, R. A., and Carr, Z. R., "Near-Surface CO_2 Tunable Diode Laser Absorption Spectroscopy Concentration Measurements in the LENS-XX Expansion Tunnel Facility," presented at the 54th AIAA Aerospace Sciences Meeting, 2016. https://doi.org/10.2514/6.2016-0246

[44] Dean, T., Blair, T. R., Roberts, M., Limbach, C., and Bowersox, R. D., "On the Initial Characterization of a Large-Scale Hypervelocity Expansion Tunnel," *AIAA SCITECH 2022 Forum*, American Institute of Aeronautics and Astronautics. https://doi.org/10.2514/6.2022-1602

[45] Dean, T., Siddiqui, F., Gragston, M. T., and Bowersox, R. D., "Index of Refraction Fluctuation Spectra in Aerothermochemical Non-Equilibrium Shock Layers," *AIAA SCITECH 2023 Forum*, American Institute of Aeronautics and Astronautics, 2023. https://doi.org/10.2514/6.2023-0270

[46] Zander, F., Molder, S., Morgan, R., Jacobs, P., and Gollan, R., "High Temperature Gas Effects for Converging Conical Shocks," presented at the 18th AIAA/3AF

International Space Planes and Hypersonic Systems and Technologies Conference, 2012. https://doi.org/10.2514/6.2012-5939

[47] Chase, M. J., "NIST-JANAF Thermochemical Tables, Monograph 9," American Chemical Society, Washington DC.

[48] Bryan, C. A., Dean, T., Morreale, B. J., and Bowersox, R. D., "Computational Simulations of Hypersonic Mach Stems at High Enthalpy," presented at the AIAA SCITECH 2023 Forum, 2023. https://doi.org/10.2514/6.2023-0858

[49] Chai, W. S., Bao, Y., Jin, P., Tang, G., and Zhou, L., "A Review on Ammonia, Ammonia-Hydrogen and Ammonia-Methane Fuels," *Renewable and Sustainable Energy Reviews*, Vol. 147, 2021, p. 111254. https://doi.org/10.1016/j.rser.2021.111254

[50] Cai, T., and Zhao, D., "Overview of Autoignition and Flame Propagation Properties for Ammonia Combustion," *AIAA Journal*, Vol. 61, No. 7, 2023, pp. 2754–2778. https://doi.org/10.2514/1.J062764

[51] Feltis, S. E., Zhang, Z., Dean, T. S., Bowersox, R. D. W., Siddiqui, F., and Gragston, M., "Measurements of No Rotational and Vibrational Temperatures behind a Normal Shock in Hypervelocity Flow via Absorption Spectroscopy," *Experiments in Fluids*, Vol. 65, No. 7, 2024, p. 112. https://doi.org/10.1007/s00348-024-03841-w

[52] Gilvey, J. J., Ruesch, M. D., Daniel, K. A., Downing, C. R., Lynch, K. P., Wagner, J. L., and Goldenstein, C. S., "Quantum-Cascade-Laser-Absorption-Spectroscopy Diagnostic for Temperature, Pressure, and NO $X^2\,\Pi_{1/2}$ at 500 kHz in Shock-Heated

Air at Elevated Pressures," *Applied Optics*, Vol. 62, No. 6, 2023, p. A12. https://doi.org/10.1364/AO.464623

[53] Guo, S., Li, J., Wei, Y., Yang, Y., Lu, Z., Xing, X., Ren, W., and Yao, S., "A Multi-Laser Hybrid Absorption Sensor for Simultaneous Measurement of NH3, NO, and Temperature in Denitrification Flue Gas," *Infrared Physics & Technology*, Vol. 136, 2024, p. 105034. https://doi.org/10.1016/j.infrared.2023.105034

[54] Li, Q., Ji, F., Wang, W., Ma, L., and Wang, Y., "A Mid-infrared Laser Absorption Sensor for Calibration-free Measurement of Nitric Oxide in Laminar Premixed Methane/Ammonia Cofired Flames," *Microwave and Optical Technology Letters*, Vol. 66, No. 1, 2024, p. e33815. https://doi.org/10.1002/mop.33815

[55] Almodovar, C. A., Spearrin, R. M., and Hanson, R. K., "Two-Color Laser Absorption near 5 Mm for Temperature and Nitric Oxide Sensing in High-Temperature Gases," *Journal of Quantitative Spectroscopy and Radiative Transfer*, Vol. 203, 2017, pp. 572–581. https://doi.org/10.1016/j.jqsrt.2017.03.003

[56] Gilvey, J. J., and Goldenstein, C. S., "A Quantum-Cascade-Laser-Absorption-Spectroscopy Diagnostic for Measuring Temperature and Nitric Oxide at 1 MHz in Shock-Heated Air," presented at the AIAA AVIATION 2023 Forum, 2023. https://doi.org/10.2514/6.2023-4267

[57] Chang, E., Streicher, J. W., and Krish, A., "High-Temperature Infrared-Based Diagnostic for Nitric Oxide Using Tunable Diode Laser Absorption

Spectroscopy," presented at the AIAA SCITECH 2022 Forum, 2022. https://doi.org/10.2514/6.2022-1781

[58] Girard, J. J., Finch, P. M., Strand, C. L., Hanson, R. K., Yu, W. M., Austin, J. M., and Hornung, H. G., "Measurements of Reflected Shock Tunnel Freestream Nitric Oxide Temperatures and Partial Pressure," *AIAA Journal*, Vol. 59, No. 12, 2021, pp. 5266–5275. https://doi.org/10.2514/1.J060596

[59] Upadhyay, A., Lengden, M., Enemali, G., Stewart, G., Johnstone, W., Wilson, D., Humphries, G., Benoy, T., Black, J., Chighine, A., Fisher, E., Zhang, R., Liu, C., Polydorides, N., Tsekenis, A., Wright, P., Kliment, J., Nilsson, J., Feng, Y., Archilla, V., Rodríguez-Carmona, J., Sánchez-Valdepeñas, J., Beltran, M., Polo, V., Armstrong, I., Mauchline, I., Walsh, D., Johnson, M., Bauldreay, J., and McCann, H., "Tomographic Imaging of Carbon Dioxide in the Exhaust Plume of Large Commercial Aero-Engines," *Applied Optics*, Vol. 61, No. 28, 2022, p. 8540. https://doi.org/10.1364/AO.467828

[60] Sun, P., Zhang, Z., Li, Z., Guo, Q., and Dong, F., "A Study of Two Dimensional Tomography Reconstruction of Temperature and Gas Concentration in a Combustion Field Using TDLAS," *Applied Sciences*, Vol. 7, No. 10, 2017, p. 990. https://doi.org/10.3390/app7100990

[61] Song, J., Hong, Y., Xin, M., Wang, G., and Liu, Z., "Tomography System for Measurement of Gas Properties in Combustion Flow Field," *Chinese Journal of Aeronautics*, Vol. 30, No. 5, 2017, pp. 1697–1707. https://doi.org/10.1016/j.cja.2017.08.004

[62] Jeon, M.-G., Deguchi, Y., Kamimoto, T., Doh, D.-H., and Cho, G.-R., "Performances of New Reconstruction Algorithms for CT-TDLAS (Computer Tomography-Tunable Diode Laser Absorption Spectroscopy)," *Applied Thermal Engineering*, Vol. 115, 2017, pp. 1148–1160. https://doi.org/10.1016/j.applthermaleng.2016.12.060

[63] Song, J., Hong, Y., Wang, G., and Pan, H., "Algebraic Tomographic Reconstruction of Two-Dimensional Gas Temperature Based on Tunable Diode Laser Absorption Spectroscopy," *Applied Physics B*, Vol. 112, No. 4, 2013, pp. 529–537. https://doi.org/10.1007/s00340-013-5435-0

[64] Keller, A. R., Spearrin, R. M., Bendana, F. A., Kaialau, D., Perezselsky, A., and Cortopassi, A., "Shear Coaxial Mixing and Combustion of Methane-Oxygen Examined by Laser Absorption Tomography," presented at the AIAA SCITECH 2024 Forum, 2024. https://doi.org/10.2514/6.2024-2420

[65] Steavenson, B. R., and Pineda, D. I., "Mid-Wave Infrared Laser Absorption Tomography of Nitrogen Oxides for Spatially Resolved Quantitative Thermochemistry in H_2 -N_2 O Flames," *Applied Optics*, Vol. 64, No. 16, 2025, p. D103. https://doi.org/10.1364/AO.554557

[66] Shi, D., Jiao, T., Cheong, K.-P., Chen, W., Liu, Y., Song, Y., Liu, Y., and Ren, W., "Volumetric Imaging of H_2 O Transportation in Laminar Jets Issuing from Polygonal Nozzles by Masked and Regularized Tomographic Absorption Spectroscopy," *Optics Express*, Vol. 32, No. 27, 2024, p. 48421. https://doi.org/10.1364/OE.543477

[67] Goodwin, D. G., Moffat, H. K., Schoegl, I., Speth, R. L., and Weber, B. W., "Cantera: An Object-Oriented Software Toolkit for Chemical Kinetics, Thermodynamics, and Transport Processes," Zenodo, Nov 17 2025. https://doi.org/10.5281/ZENODO.17620923

[68] Gokcecik, B. K., Guthikonda, N., Clark, A., Zhao, P., and Zhang, Z., "Laser-Induced Plasma Analysis of Ammonia-Oxygen and Ammonia-Oxygen-Enriched-Air Flames at Elevated Pressures," *Combustion and Flame*, Vol. 271, 2025, p. 113803. https://doi.org/10.1016/j.combustflame.2024.113803

[69] Shi, D., Xu, Z., Huang, A., Cong, Z., Chen, C., Ai, S., Niu, R., Xia, H., Cheong, K.-P., and Kan, R., "Two-Line Jointly Optimized Tomographic Absorption Spectroscopy for Flame Measurement with Adaptive Hybrid Regularization," *Optics Express*, Vol. 33, No. 13, 2025, p. 27942. https://doi.org/10.1364/OE.566682

VITA

Samuel E. Feltis graduated with a Bachelor of Science from the University of Minnesota, Twin Cities in a major of Aerospace Engineering and a minor in Astrophysics. He joined the Laser Diagnostics Laboratory at the University of Tennessee, Knoxville under the supervision of Dr. Zhili Zhang in Fall of 2020 in order to pursue his Ph.D. in Aerospace Engineering.